Parameter Identification of Mechanistic Milling Force Model for Carbon Fiber-Reinforced Polymer Composite Parts

by

Mehran Farhadmanesh
B.Sc., K. N. Toosi University of Technology, 2010
M.Sc., K. N. Toosi University of Technology, 2013

A Dissertation Submitted in Partial Fulfillment of the
Requirements for the Degree of

DOCTOR OF PHILOSOPHY

in the Department of Mechanical Engineering

Parameter Identification of Mechanistic Milling Force Model for Carbon Fiber-Reinforced Polymer Composite Parts

by

Mehran Farhadmanesh
B.Sc., K. N. Toosi University of Technology, 2010
M.Sc., K. N. Toosi University of Technology, 2013

Supervisory Committee

Dr. Keivan Ahmadi, Supervisor
(Department of Mechanical Engineering, University of Victoria)

Dr. Zuomin Dong, Departmental Member
(Department of Mechanical Engineering, University of Victoria)

Dr. Yang Shi, Departmental Member
(Department of Mechanical Engineering, University of Victoria)

Dr. Rishi Gupta, Outside Member
(Department of Civil Engineering, University of Victoria)

Supervisory Committee

Dr. Keivan Ahmadi, Supervisor
(Department of Mechanical Engineering, University of Victoria)

Dr. Zuomin Dong, Departmental Member
(Department of Mechanical Engineering, University of Victoria)

Dr. Yang Shi, Departmental Member
(Department of Mechanical Engineering, University of Victoria)

Dr. Rishi Gupta, Outside Member
(Department of Civil Engineering, University of Victoria)

ABSTRACT

The application of Carbon Fiber-Reinforced Polymers (CFRP) has been exponentially increasing during the last decade in a wide range of industries such as automotive, aerospace, wind turbines, medical instruments, and sports goods. This popularity of CFRP is because of their excellent mechanical properties such as a higher strength-to-weight ratio and superior fatigue and corrosion resistance. Although CFRP are made near net shape, they need to be machined for assembly at the finishing stage. Because machining is at the final stage of the manufacturing process, the occurrence of failure types including fiber pull-out, fiber breakage, matrix smearing, and especially delamination will cause rejection of the high-value-added composite part. This work is motivated by the need to better understand the fundamental machining processes, especially milling operation for CFRP composite materials.

Since delamination is correlated with the level of cutting forces, it is required to develop cutting force models for controlling and optimization of the machining pro-

cess to avoid damage. Among various approaches to studying the milling operation, mechanistic cutting force models are commonly used to compute milling forces under different machining parameters such as axial and radial depth of cut and feedrate. In isotropic (e.g. metallic) materials, parameters of the mechanistic model are treated as constants that are identified using well-established experimental procedures. Mechanics of chip formation in CFRP varies depending on the fiber cutting angle, which continuously changes as the tool rotates in milling operation. To address this variation, a mechanistic model with parameters that depend on fiber cutting angle is proposed, and a new experimental method is presented to identify the parameters of the proposed model. The mechanistic force model parameters, also known as specific force coefficients (SFC), are assumed to be periodic functions of the fiber cutting angle, where the Fourier coefficients of the periodic function are identified from the milling forces measured during a set of milling operations at various feedrate and fiber orientations. The experimental validation of the presented force modeling approach confirms its accuracy to predict cutting forces in milling CFRP.

In addition to the complexity of CFRP milling model, unexpected changes in cutting conditions and tool wear during the process also add to the uncertainty of the conventional offline calibration approaches, causing the need for online identification methods to adaptively recalibrate the model parameters. In this work, two recursive identification methods based on recursive least squares (RLS) and Kalman filter (KF) algorithms are presented. In the RLS method, the model parameters are identified by the recursive regression of the forces measured at discrete time steps. Runout parameters are measured accurately and modeled properly in the RLS algorithm in order to improve the performance of RLS and avoid biased errors. The initial immersion angle of the tool is also estimated as the first stage of the identification process because the RLS algorithm requires this value before it starts recursively updating the unknown SFC of the force model in the second stage.

In the KF approach, a state-space model and observer with constant stochastic dynamics are constructed. In addition to SFC, the runout forces could be also identified as harmonic functions in the state variables vector without prior knowledge of their values, which is one advantage of KF over RLS. The initial immersion angle is considered as an additional state variable in an extended Kalman filter (EKF) by linearization of the observation matrix in a one-stage identification process. Numerical simulations and experimental studies on milling UD-CFRP and MD-CFRP validate the performance of the presented methods. As a result, the identified model accu-

rately predicts the machining forces, and therefore, can be used for process monitoring and optimization in the machining of metals and composite materials.

Contents

List of Tables

List of Figures

ACKNOWLEDGEMENTS

I would like to acknowledge my wonderful family and friends who have been always there for me during the difficult times of this long journey. I believe I would have not been able to graduate without the endless love and support of my parents, Hasan and Sorur, who are the best teachers in my life. I am forever grateful to Hamed, Shirin, Alexandra, Sadegh Hasanpour, and Yaser Mohammadi for all their help and positive encouragement.

This research was financially supported by the NSERC Canadian Network for Research and Innovation in Machining Technology Network (CANRIMT 2).

I would also like to sincerely express my gratitude to my supervisory committee members: Dr. Keivan Ahmadi as the supervisor, Dr. Zuomin Dong, Dr. Yang Shi, and Dr. Rishi Gupta for their invaluable feedback during the course of my PhD degree. Appreciation is extended to my colleagues in Dynamics and Digital Manufacturing lab (DDM) at the University of Victoria, Industrial Technology Research Institute (ITRI) in Taiwan for donation of equipment, material, and services.

DEDICATION

This dissertation is dedicated to my family,
who stood by my side all the time.

Chapter 1

Introduction

1.1 Research Background and Motivation

Carbon fiber reinforced polymers (CFRP) are composite materials in which carbon fibers embedded in the polymeric matrix resin. Each carbon fiber filament has a diameter in the range of 5-15 microns. Carbon fibers are essentially used to improve the stiffness and strength of the composite material while the synthetic resin matrices such as polymides, epoxies, vinyl esters, and other thermoplastics maintains fiber alignment and transfers structural load among the fibers. This reinforced structure can be designed to have more strength and fatigue resistance than conventional metallic materials such as steel and aluminum. Compared to other polymeric composites with glass and aramid, carbon fibers are mainly used in applications requiring more stiffness rather than tensile modulus of glass and aramid fibers [1]. CFRP and GFRP are two main types of fiber-reinforced materials. The key difference between them is that CFRP contains carbon as the fiber component, whereas GFRP contains glass as the fiber component. Concerning the properties, CFRP is lightweight and has low density, while GFRP has medium weight and medium density. Moreover, CFRP is highly expensive, which limits the use of this material in many applications. Meanwhile, comparatively, GFRP is less expensive and is used where CFRP cannot be used [1]. Considering the scope and application of this research project, CFRP was chosen to be studied.

1.1.1 Classification of CFRPs

CFRPs could be categorized based on the length and arrangement of fibers. A distinction is made between continuous strand, long and short fibre reinforced materials. In continuous strand reinforced materials, single fibres are arranged to roving with arbitrary directions where one roving usually consists of 5000-15000 fibres. In short CFRPs, the fibre segments are randomly arranged in the matrix while long fibers reduce the risk of lattice defects which can cause fiber failure and crack propagation [2]. In this work, the scope of project is limited to the long-fiber CFRPs. For short fiber CFRP, the composite material can be treated as an isotropic material. fibers embedded in the resin matrix are considered to be cut together in the milling operation.

.

In terms of substance's resistance to elastic deformation, carbon fibers can be classified into standard modulus, intermediate modulus, and high modulus groups. Standard modulus carbon fiber has a huge share of more than 80% of the total market these days and it's mostly used in automotive and aerospace application while the other two classes are usually used in pressure vessels, wind turbines blades, and some aerospace applications. Other dominant physical properties of carbon fibers include light weight, low coefficients of thermal expansion, and great fatigue resistance and electrical conductivity.

The long fiber-reinforced composites are classified based on the orientation of fiber directions. A CFRP laminate is usually manufactured by stacking several layers of plies together in a specific orientation. These flat layers, in which long carbon fibers form the assembled fabric, could be Uni-Directional (UD), Multi-Directional (MD), or Woven plies. Manufacturers design the composite laminates in order to achieve the lightest and strongest structures by matching the orientation of fibers in the direction of applied loading in the CFRP materials.

In UD laminates, placing the fibers in one direction will result in maximum tolerance of forces in that certain direction and therefore the best possible mechanical properties of the CFRP components. However, to increase the tolerance of CFRP components against the applied forces in more than one direction, several laminates of UD plies will be stacked up together to build a MD formation which is reinforced in different preferential directions. For bidirectional fiber orientations prepreg ply (also called woven-ply), the ultimate strength is lower, but occurs in two directions.

As the direction of the fibers becomes more statistically distributed throughout the composite, the ultimate strength decreases, but the properties are more uniform in all loading directions [1].

Proper selection of ply orientation is important in CFRPs in order to get optimum mechanical properties and provide an efficient structural design because strength design requirements depend on the direction of the applied load, the orientation of the plies and correct sequence [3]. Figure 1.1 shows the schematic illustration of the CFRP. The focus of this research is on flat UD-CFRP and MD-CFRP laminates.

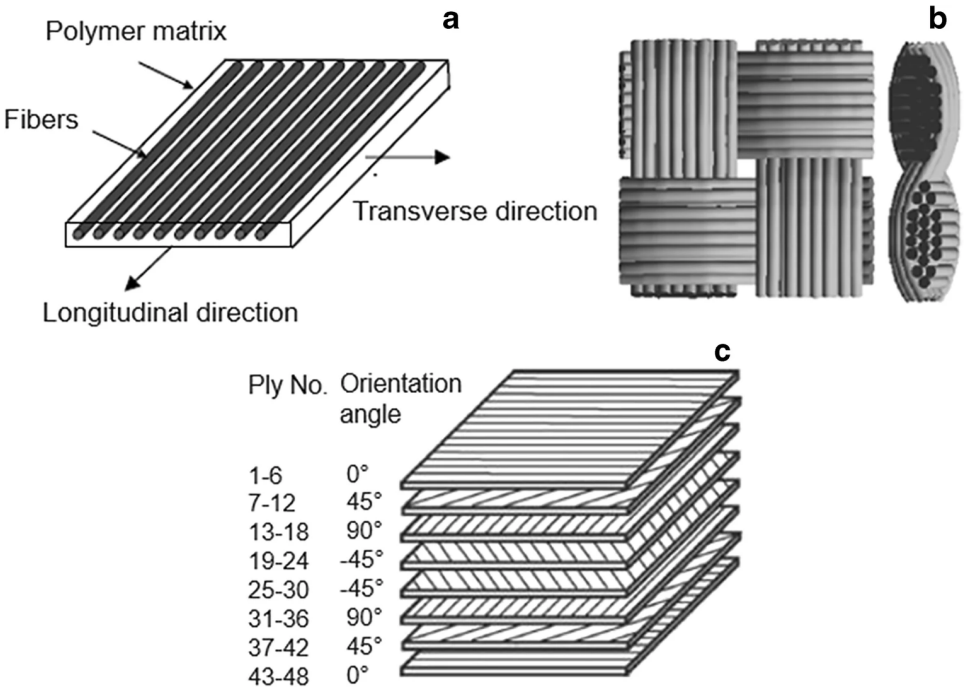

Figure 1.1: (a) Unidirectional (UD) fiber orientation ply; (b) Bidirectional fiber orientations ply (woven-ply); and (c) Multi-directional (MD) laminate with quasi-isotropic laying-up sequence of UD-plies CFRP [3].

1.1.2 Material manufacturing process

Several manufacturing processes exist to impregnate the fibers with the matrix substance and build the component [1]. the selection of the right method depends on component size, matrix material, and geometrical components. The least complicated method is spraying or injecting resin to the laminate placed in one-sided mould under standard atmospheric conditions or vacuum bagging. Another technique is resin transfer moulding, also known as RTM, in which fibers are placed in a dry

stack and compressed together with a binder before injection of resin to the second mould layer. However, the most preferred manufacturing method for producing fiber-reinforced composite parts is prepreg layup (pre-impregnated fabrics). It is usually done by automated tape placement machines. Figure 1.2 schematically shows prepreg layup of a composite part over a contoured tool surface.

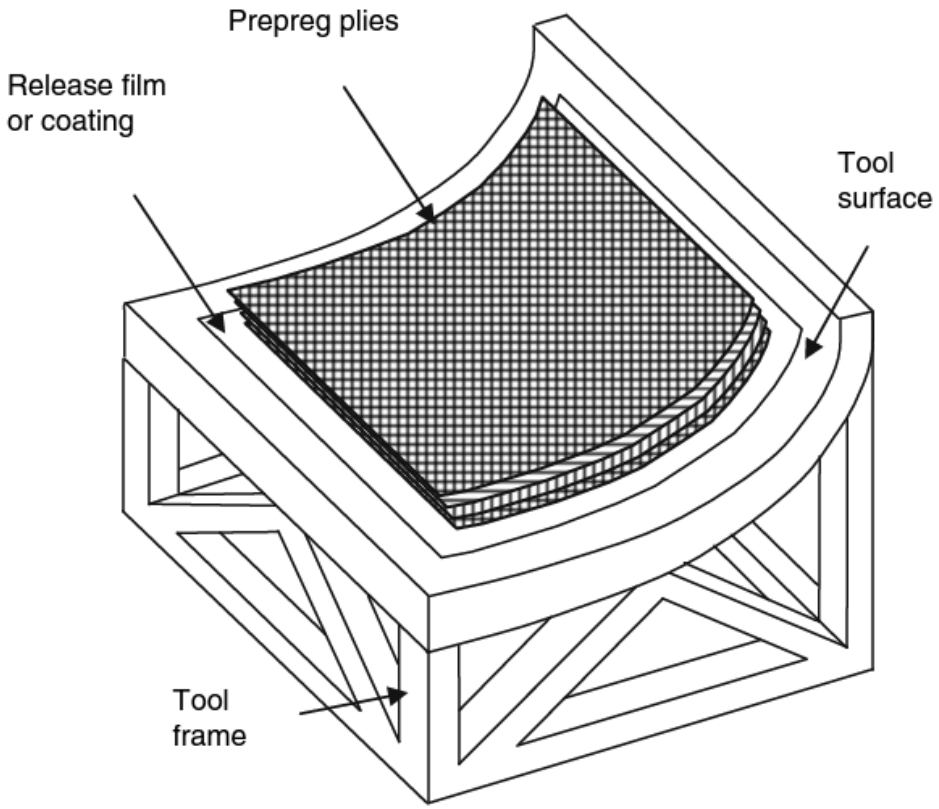

Figure 1.2: Schematic of prepreg layup over a contoured mold [1].

The manufacturing procedure involves removing the prepreg tape, and then cutting the fabrics to the final shape and size, stacking the individual layers (plies) together in the desired orientations, put into a mould and typically heated in an autoclave to form the final shape at temperature around 150°C. The resin reflows and cures under these certain conditions and then covering with appropriate materials for the cure process. The objective of the cure process is to remove volatiles and excess air, to facilitate solidification the laminate, and to apply temperature and pressure to ensure good bonding during cure. For large structures, this process may be adapted to "out of autoclave" by applying pressure with vacuum bagging instead of the tool and using an oven to cure the component. Autoclave processing ensures

good lamination but requires a somewhat expensive piece of hardware [4]. The readers are advised to follow reference [5] for more detailed descriptions of composites manufacturing processes.

1.1.3 CFRP in industrial applications

CFRP are used in many advanced technologies due to their ability to provide materials for several initiatives of energy efficiency and renewable energies. The application of CFRP in a wide range of industries such automotive, aircraft, wind turbines, medical instruments, and sports goods have been exponentially increasing due to their higher strength to weight ratio and a superior fatigue and corrosion [6, 7]. Lightweighting property of CFRP in transportation applications reduce the fuel consumption and leads to energy reduction. Moreover, for instance in wind turbines, using carbon fiber composites enables the designers to extend the turbine blades which results in capturing more wind energy as well as developing the performance of the wind turbine system and putting away the limitation of conventional materials used in this industry. Another example of carbon fiber applications is CFRP-based pressure vessels in alternative fuel vehicle where using CFRP enables these new vehicle to increase the fuel economy for longer distance travels. Many other applications exist for CFRP composite parts which guarantees the spike in anticipated future demands.

1.1.4 Machining operations and challenges

Although CFRPs are mostly produced near net shape, machining is often required to satisfy the dimensional requirements, and to prepare the parts for the assembly. Majority of machining operations e.g. contour milling, drilling, trimming, waterjet machining are still necessary for the finishing stage. In this research, focus will be on the CFRP milling process.

The schematic of a single point cutting tool is shown in Figure 1.3a, where the cutting conditions such as chip thickness (h), cutting speed (V_c), and depth of cut (a) remain constant at all times under orthogonal cutting operation. Because the cutting edge is perpendicular to cutting direction, cutting forces only have components in cutting and feed directions (F_t and F_f, respectively). Figure 1.3b also shows a schematic of multi points cutting tool where the machined surface is perpendicular to the axis of rotation of the cutter. Also, The engagement into the the workpiece is in the axial direction of the cutter. At every angular position of the cutting edge, the

instantaneous chip thickness and fibre cutting angle are determined using the dexel based approach [8].

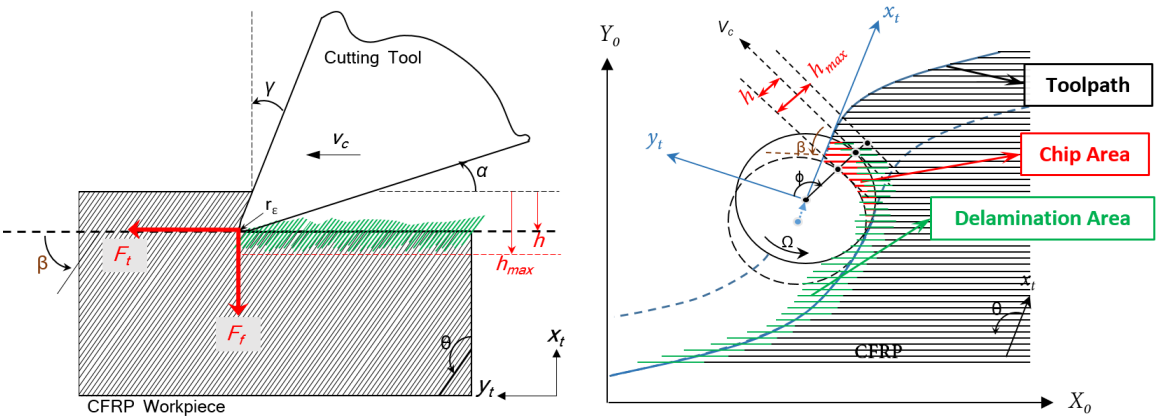

(a) (b)

Figure 1.3: (a)Interaction between tool and CFRP workpiece in single point orthogonal cutting operation; (b)Schematics of main parameters in multi points orthogonal milling operation for CFRP

Machinability is a parameter which always takes much attention in industrial applications in order to increase the efficiency of the production process. Quality of the machined surface is a key factor in machinability of CFRPs. Because of the inhomogeneous structure of CFRP composites, material damages occurs more often in CFRPs than for homogeneous metallic parts during the machining process. Aerospace and aviation industry, which benefits the most from composites technology, has the highest strict requirements on machining quality. Low quality finishing surface is not tolerated on the structural components [1].

Delamination is one of the most challenging issues in CFRP milling process due to the complex interaction between the end mill and the laminates. It is caused by the low interlaminate strength of the composite structure and high transverse forces resulting from cutting action. Kalla D. et al. [9] proposed a model to predict the cutting forces which is a good indicator for controlling and optimizing cutting parameters to avoid delamination and material deformation. Numerous parameters such as fiber orientation and fiber volume [10], axial depth of cutting, and feed-rate [11], cutting speed [12] were identified to play a significant role in surface finish quality.

A study was also carried out on the influence of resin type on the delamination behavior of CFRPs [13]. They used two different matrices (an 8552 epoxy with improved toughness and an unmodified brittle 3501-6 epoxy) in a flexure test under

similar loading. The results confirmed the improved performance of the modified resin in terms of avoiding crack initiation and delamination growth.

Since delamination is highly correlated with cutting forces, applying improper speeds and feeds, inappropriate tool geometry and tool wear will cause cutting forces exceed from a normal level and it affects the machinability of CFRP composites. According to Figure 1.4, there are three basic types of delamination. Type I shows broken fibers prolonging inward forming the trimmed edge. Type II includes uncut fibres which coming outside the material. Type III describes fibres which are partially attached to the milled edge [14].

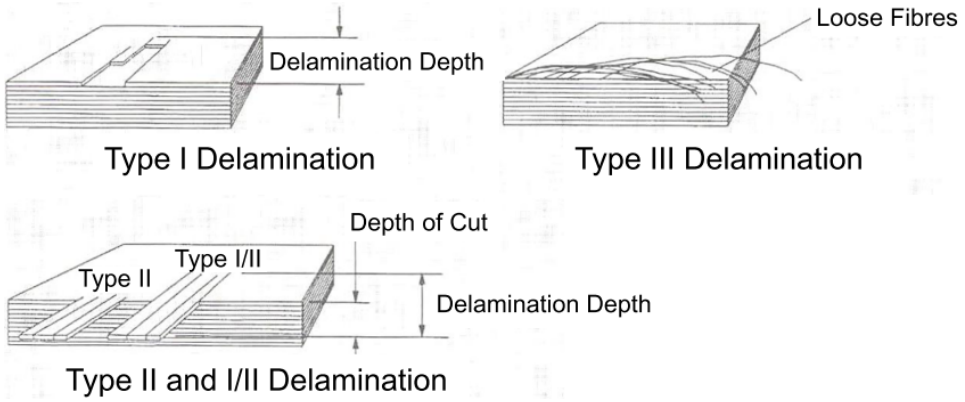

Figure 1.4: Classification of delamination in CFRP laminates [14].

1.1.5 Research motivation

CFRPs are increasingly used in various industries due to their lightweighting and superior mechanical properties (i.e. high strength-to-weight ratio and a superior fatigue and corrosion resistance) [6, 1, 7]. CFRPs are machined to be prepared for assembly [15]. Since machining is at the final stage of the production process, occurrence of failure types such as fiber pull out, fiber break, matrix smearing and especially delamination will cause rejection of the high value-added components. This work is motivated by the need to better understand the fundamental machining processes for CFRPs which are inhomogeneous composite materials. Since delamination is correlated with the level of cutting forces, we also aim to explore potential opportunities for developing the cutting force models in order to control and optimize the process to avoid damages.

This dissertation focuses on study of CFRP machining for generation of process

knowledge and the findings are applied to optimise conventional CFRP milling process. The detailed state of the art concerning these topics is presented in Section 1.2. The literature review section is organized into three subsections: Subsection 1.2.1 reviews the studies related to the cutting mechanics and chip formation mechanism in milling CFRP; Subsection 1.2.2 provides an overview of cutting force modeling in milling of composite materials while Subsection 1.2.3 is a brief overview of the recursive online methods in identification of dynamic systems. The research objectives are presented in Section 1.3, as well as the structure of the thesis in Section 1.4.

1.2 Literature Review

This Section provides an overview regarding characteristic properties of CFRP, chip mechanics in orthogonal cutting of CFRP components, and different modeling approaches in machining processes including cutting force models, specific cutting energy models, and online identification approaches in CFRP milling.

1.2.1 Chip formation mechanism in milling CFRP

The chip formation process in machining unidirectional FRPs is categorized into five different types, as shown in Figure 1.5, depending on fiber orientation and cutting edge rake angle. According to [16], delamination type I chip occurs when a layer of composite is peeled of and breaks off when the bending stress exceeds the bending strength of the fibers. Type II happens when the fibers buckle and fail due to bending stress. Type III cutting chip is similar to shear-type chip formation in metal cutting followed by interlaminar shear along the fiber-matrix interface. Type IV and V occurs when severe fracture in the fibers-matrix and bulky discontinuous chips are formed.

Detailed literature reviews on machining of composite materials can be found in [1, 7] where experimental, analytical, and finite element modelling techniques were used to study the chip formation mechanism in machining CFRPs.

Although CFRPs are often fabricated to near net shapes (e.g. by molding or filament winding), a post machining operation is usually needed to guarantee an acceptable dimensional tolerance, surface quality, and other functional requirements in assembly and finishing stages [17].

Machining of CFRP is more difficult than machining of conventional metals because of anisotropic properties and having two phases of material with totally different

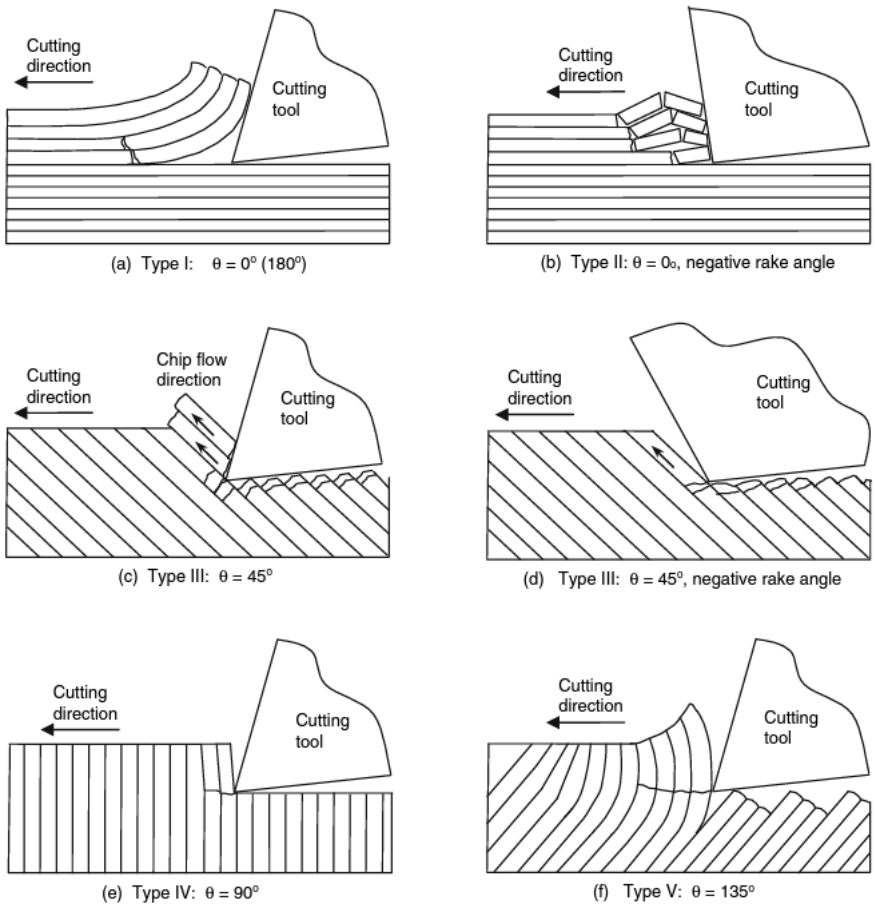

Figure 1.5: Cutting mechanisms in the orthogonal machining of CFRP with a sharp edge [16].

mechanical and thermal properties, which leads to a more complex interaction between matrix and fibers during machining [12]. The heat generated during machining is dissipated through the cutting tool, chip, and workpiece. The heat may be high enough to cause melting or decomposition of the polymer matrix. The cutting temperatures at high cutting speeds may also be high enough to cause thermally activated tool wear. Therefore, the cutting forces will be affected at high temperatures. The machinability of FRPs is improved tremendously when machining at cutting speeds lower than the transitional speed [5]. The scope of this work is limited to the effect of fiber orientation angle in the mechanistic force model, and the temperature is assumed a constant parameter in this project.

In general, the methods used in studying the machining of CFRPs are classified into four categories [18]:

- Experimental study of the macro/microscopic machinability of CFRP composites [19], and optimization of the machining process [20].
- Analytical studies on the estimation of process responses, such as cutting forces [21].
- Numerical modeling and simulation of machining of unidirectional CFRPs with methods ranging from the macro-mechanical to the micro-mechanical approaches.
- Mechanistic force methods are based on the physics of the cutting process and could be represented by mathematical equations and empirical calibration approaches for process parameter predictions [22].

- Experimental investigation:

Orthogonal cutting tests on CFRP was conducted by Koplev [23] to study chip formation mechanisms and the effect of fiber direction on the surface roughness. They found out that surface quality depends on fiber cutting direction. Better surface finishing was observed when fibers orientation is parallel to cutting direction. They also studied the effect of tool geometry on machining to see the effect of tool's clearance angle on machining forces.

Hocheng et al. [24] conducted experimental tests on milling of CFRPs. They could successfully investigate chip formation, surface roughness, and cutting forces. They also categorized chips as powder-like and ribbon-like on the basis of fracture and buckling of fibers, respectively.

Another work was done by Wang et al. [17] to analyze orthogonal cutting experiments on unidirectional laminates. They observed greater thrust forces than cutting forces due to elastic recovery of the fibers. As their next step, they conducted similar tests on multidirectional laminates [16] consisting unidirectional laminates with different fiber directions. They concluded that each layer behaves as an independent laminate, and the superposition principle is suitable to calculate cutting forces.

Milling process is usually used as a corrective operation to produce a high-quality surface finishing [24]. In contrast to orthogonal turning operation, milling is characterized by interrupted cuts and variation of theoretical chip thickness during tool rotation, which makes the study of milling CFRPs more complicated.

- Analytical models:

A theoretical model was presented by Jahromi A. et al. [25] for predicting cutting forces based on the material mechanical properties of FRPs. They developed a new analytical method using energy method to predict the machining forces for orthogonal machining of unidirectional polymer–matrix composites for fiber orientations ranging from 90°to 180°.

- Numerical study:

These studies are mostly based on Finite Element Method [26] and Discrete Element Method [27]. Most of the current numerical methods are focused on orthogonal cutting and not suitable for three-dimensional modeling of more complex processes such as drilling, milling, etc. [6].

Using Artificial Neural Networks (ANN) can lead to prediction of the mechanical behavior of composites. The predictive capabilities of these networks can be improved by determining more appropriate ANN structures. There are still challenges about how to use one type of composite material analysis data for other kinds; how many materials should be used as a training set to give accurate predictions for a new material; In addition, what material properties are the most important to take into account in model [28].

- Mechanistic models:

This work utilizes mechanistic modeling techniques for simulating the cutting of CFRP with a helical end mill. . It is shown that the method developed is capable of predicting the cutting forces in helical end milling of unidirectional and multidirectional composites and over the entire range of fiber orientations from 0° to 180°.

A mechanistic machining model was presented by Kalla et al. in [9] to estimate the cutting and rubbing force coefficients in helical end milling of unidirectional and multidirectional laminates. The methodology was developed for predicting the cutting forces by transforming specific cutting energies from orthogonal cutting to oblique cutting over the entire range of fiber orientations from 0° to 180°. In a comprehensive study on mechanistic force models, Hintze et al. [29] focused on machining CFRP during slot milling experiments and showed that occurrence of delamination is highly related to tool wear and fiber cutting angle. They also proposed a model for propagation of the damages in composite materials.

1.2.2 Mechanistic cutting force modeling in milling CFRPs

Mechanistic models are used to predict the cutting forces directly from specific cutting energy functions and chip geometry. Specific cutting energy (also known as specific cutting force coefficients) is a material property that describes the amount of energy consumed in removing a unit volume of the workpiece material in the process of machining. Specific cutting energy for metals depends on the chip thickness, cutting speed, and tool wear. Specific cutting energy for CFRPs also depends on fiber orientation. The cutting forces are determined as the product of the uncut chip area and the specific cutting force coefficients. Although various mechanistic models have been developed for predicting cutting forces in metals, there is very limited work on mechanistic modeling in machining CFRP [30].

The specific cutting energy for a given tool–workpiece pair is defined as the machining power per unit volume per unit time, and is determined experimentally from the cutting force and material removal rate. For example, the specific cutting energy in orthogonal cutting Figure 1.3a is given by:

$$K_t = p_s = \frac{P_m}{Z_w} = \frac{F_t.V_c}{f.a.V_c} = \frac{F_t}{f.a} \tag{1.1}$$

where f is the feedrate, a is depth of cut, V_c is cutting speed, and F_t is the cutting force. K_t is specific cutting energy or specific cutting force coefficients (SFC). If the specific cutting force coefficients (SFC) are known, the cutting force, F_t, and thrust force, F_f for a given cutting geometry in Figure 1.3a can be calculated in 1.2 in which K_t and K_f are SPC in two principle directions. Edge force coefficients K_te and K_fe also account for the cutting forces that do not contribute to the shearing action [1]:

$$\begin{aligned} F_t &= K_t(h,\theta)h.a + K_{te}.a \\ F_f &= K_f(h,\theta)h.a + K_{fe}.a \end{aligned} \tag{1.2}$$

Schulze V. [31] experimentally obtained the machining forces on short glass fiber reinforced polyesters. Specific cutting force coefficients in feed and normal directions to the tool movement were determined for various parameters of cutting velocity, cutting depth, cutting edge rounding and tool inclination. Using a multivariate regression model allows calculation of machining forces (and direction) for arbitrary milling operations. Figure 1.6 shows the results of their modeling in which there is a disproportional increase in specific forces when tool edge radius is greater than chip

thickness during machining. This variation should be considered especially in milling operations with varying cutting thicknesses from zero to feed per tooth [31].

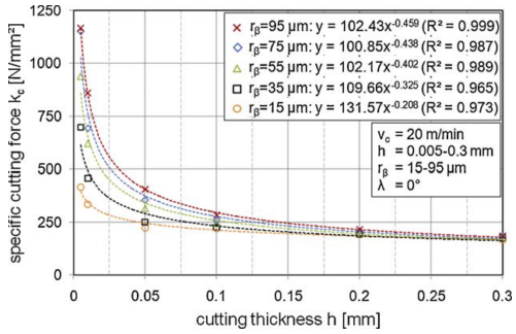

(a)

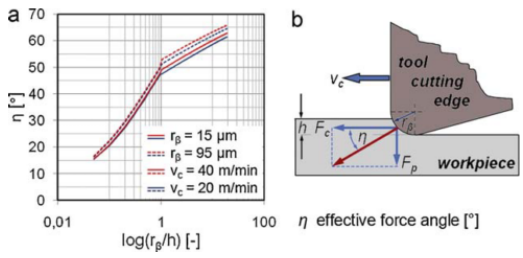

(b)

Figure 1.6: (a) Specific cutting forces vs. cutting thickness; (b) Variation of effective force angle as a function of different geometric engagement conditions [31].

Zhao et al. [32] also classified the energy consumption at different machining states. Specific energy model was also investigated and consumed energy was divided into three main types of net specific cutting energy, spindle energy, and machine tool energy consumption. However, this model is not accurate for composite materials; and some parameters such as fiber orientation and cutting angles need to be taken into account to improve the accuracy of the machining model.

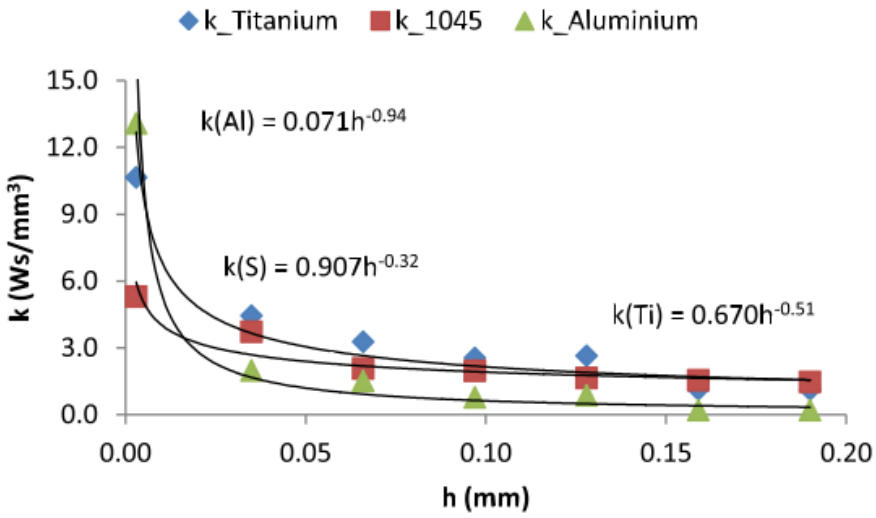

Figure 1.7: Specific energy comparison for aluminum AW6082-T6 alloy, AISI 1045 steel alloy and titanium 6Al-4V alloy [33].

The main idea of the work presented by V. Balogun [33] is modeling the specific

cutting energy coefficient based on the un-deformed chip thickness. A variation of specific energy with chip thickness was tested and reported for three different materials, Figure 1.7. Although their experiments were conducted for materials such as titanium, steel alloy, and aluminum, the methodology can be used for extracting the specific cutting energy constants for composite materials as well.

Yanli He et al. [34] also proposed a mechanistic milling force model in slot milling of unidirectional CFRP with different cutting orientations and conditions. The patterns of cutting force and resulting defects along with the inherent mechanism were investigated. The specific cutting force coefficients were calibrated experimentally. It was shown the at SFC are related to instantaneous chip thickness(t_c), fiber cutting angle(β), and cutting speed(v). According to their observation in Figure 1.8, delamination is strongly related to the fiber cutting angle. Severe uncut fibers exist when fiber cutting angle reaches 90°and beyond till 180°. When fiber cutting angle lies between 0°and 90°, no or little uncut fibres left [34].

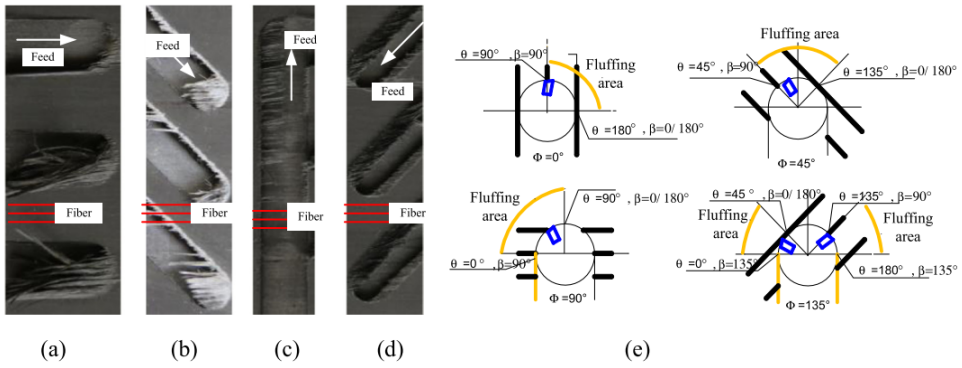

Figure 1.8: Damages during milling process in various fiber orientation angle: a) 0°, b) 45°, c) 90°, d) 135°, e) The damage sketch [34].

Phadnis et al. studied the effects of different machining conditions on the specific cutting energy of CFRP, as shown in Figure 1.9 [35]. They also showed that power consumption increases linearly with the material removal rate (MRR).

Q. AN et al. [36] compared the milling process forces for two CFRP materials with different fiber tensile strengths. They calculated the specific cutting energy, and showed that it reduces when the cutting depth increases. They also showed that improved machinability occurs for increased axial cutting depths. An exception occurs for the fibre orientation of 90°, in which the specific cutting energy maintained stable after the cutting depth exceeded the fibre diameter.

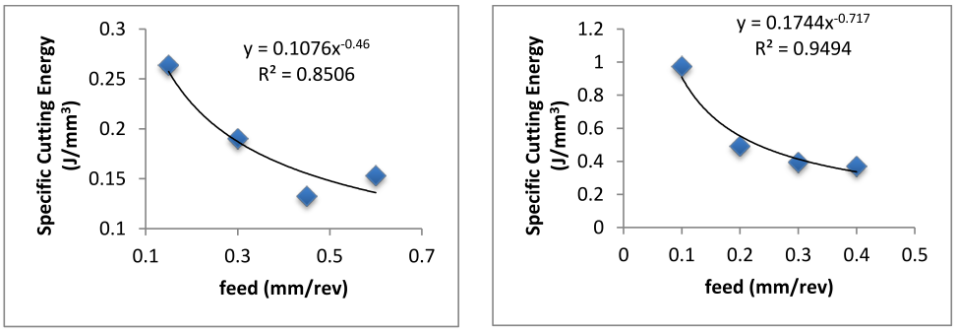

Figure 1.9: Effect of feed on the specific cutting energy for (a) pultruded CFRP composites and (b) CFRP composite pipe [35].

1.2.3 Monitoring of the machining processes

The success of manufacturing process automation hinges primarily on the effectiveness of process monitoring and control systems. Using monitoring systems seems to be an essential part of a high-quality manufacturing process which can helps to have a higher machining speed, better surface quality, lower tool wear, reduction in machining fluid usage [37].

Parameters of the cutting process model for composite materials are changing simultaneously because of variation in composite material types, different cutting tool geometries, and higher possibility of tool wearing during composite machining. An adaptive control system could be used for online prediction and controlling of damages. Therefore, It is necessary to adaptively control the force/energy by manipulating feedrate throughout the toolpath. In conventional approaches, a machinist can adjust the cutting parameters (i.e. federate) to control the level of cutting forces when an increase in the predicted forces is observed, and therefore, to avoid in-process damages.

Monitoring of machining processes helps to identify tool wear, surface roughness, material damages during machining to obtain higher productivity and better product quality, and identify the risk of severe damage to workpiece or machine tool components. The measurement techniques for monitoring are generally categorized into direct and Indirect methods.

Direct measurement is when the actual value of the variable is being directly measured. Direct methods are such as ultrasound system, laser sensors, CCD cameras for image acquisition, and light reflection technologies. A measurement system was developed for the evaluation of tool wear using laser sensors that measure displace-

ment and light intensity [38]. Moreover, the combination of flexible high-resolution CCD cameras can be used simultaneously for the acquisition of the tool images during machining to create an algorithm for data processing based on image acquisition and database [39]. The measurement sensors are divided into five main categories: surface texture sensors, surface integrity sensors, dimensional accuracy sensors, tool condition sensors, and chatter detection [40].

Although direct techniques are more accurate and useful for laboratory usage, they are not suitable for industrial applications. Interference with cutting fluid, machine tool and workpiece movements makes them an unstable system and non-practical for production lines [41].

According to Liang SY [40], monitoring and control of machining composite materials have not yet developed in industry. Particularly, control of delamination in CFRP machining is still a big challenge in which the current methods for conventional metals are not applicable. Using indirect measurement methods such as cutting force and specific cutting energy measurements, vibration analysis, and Acoustic Emission(AE) method could be a practical solution for adaptively controlling the cutting forces during the machining of CFRPs.

An optimal control problem was investigated by Bosetti et al. [42] for machining application using a supervisory controller prototype. They minimized a multi-objective target function to have an optimal productivity, energy consumption rate, tool wear and surface quality. However, the offline optimization method, used in their work, cannot be applied for online applications.

In this work, two online methods will be presented to recursively identify the periodic specific force coefficients in the CFRP milling force model. The presented methods are based on Recursive Least Squares (RLS) and Kalman Filter (KF) algorithms, and can be implemented online to monitor the variation of the force model parameters during the process.

1.2.4 The gap in CFRP milling models

The machinability of composite materials are addressed differently from the machinability of conventional materials. The major difference between metallic and composite components is their structure: isotropic for metals and anisotropic for composite materials. While for metallic materials all the structure will respond similarly in all directions, the composite structure will have localized responses from the same ma-

chining loads, leading to defects in the internal structure of the machined workpiece.

1. Because of the anisotropic nature of CFRPs, understanding of the interaction between composite material and cutting tool is more complicated than metals cutting. Lack of comprehensive models for accurately predicting cutting forces while CFRP milling is a challenging issue; A comprehensive model should be able to consider all of cutting conditions to predict cutting forces and failures such as fiber rupture, resin-fiber de-bonding, surface irregularities, and delamination around machining regions.

2. During a machining process and while the tool has interaction with the workpiece, parameters of the mechanistic force model vary as the tool wear increases. There are also other cutting conditions which might change simultaneously during the process without ability to be monitored. Therefore, it is highly required to be able to update the mechanistic force model parameters using online identification methods. As a result, accurate prediction of the cutting forces will be achievable.

1.3 Research Objectives

The main objectives of this thesis are as following:

1. **To understand the fundamental machining processes for CFRP composites and the chip formation mechanics, Chapter 2**;
   Machining-induced damages such as delamination in machining of CFRP composites is a major concern due to anisotropic nature of these materials. Because such damages may lead to scraping of a high value-added part in the final manufacturing stage, study of the chip fomation mechanism is necessary in order to improve the efficiency and avoid machining-induced damages.

2. **To identify the parameters of the mechanistic cutting force model in milling of Carbon Fibre Reinforced Polymers, Chapter 2**;
   In isotropic (e.g. metallic) materials, the parameters of mechanistic models are treated as constants which are identified using well-established experimental procedures. Mechanics of chip formation in anisotropic CFRP varies depending on the fibre cutting angle. To address this variation, the goal is to identify

the model parameters from the milling forces measured during a set of milling operations at various feedrates and fibre orientations.

3. **Online identification of mechanistic milling force models in isotropic metallic materials, Chapter 3**;
   The constant coefficients of mechanistic models, also known as Specific Force Coefficients (SFC), are identified experimentally by offline regression of the machining forces measured under an extensive set of machining conditions (e.g. feedrate, fibre orientations). The challenge is that the model parameters identified by this offline approach lose accuracy when tool wear increases or cutting conditions change during the process. Therefore, the objective is to adaptively recalibrate the model parameters during the process by using online identification methods.

4. **To develop the mechanistic force models in online identification of specific force coefficients (SFC) during CFRP milling process, Chapter 4**;
   Mechanistic models are widely used for modelling forces in machining operations, but their application in CFRP milling is challenging because of the anisotropic structure of the material. Chip formation mechanics in CFRP strongly depends on fibre cutting angle, which varies by the tool's rotation during the milling process. Considering this periodic variation, the goal is to adopt the mechanistic models of the forces in metallic materials for CFRP milling by replacing its constant coefficients with periodic functions of fibre cutting angle. Therefore, the final objective of this thesis is to accurately and adaptively predict the machining forces in milling CFRP for process monitoring, control, and optimization applications.

1.4 Structure of Thesis

This thesis consists of five chapters. Chapter 1 provides the background and motivations with a detailed introductory literature review. Chapters 2 to 4 present in manuscript format the main contributions of this thesis with relevant background, experiments, and results.

Chapter 2 proposes a mechanistic model in CFRP milling with parameters that depend on fibre cutting angle. Also, a new experimental method is presented to

identify the parameters of the proposed model. The model parameters are assumed to be periodic functions of fibre cutting angle, and the Fourier coefficients of the periodic function are identified from the milling forces.

Chapter 3 demonstrates the performance of Recursive Least Squares (RLS) and Kalman Filter (KF) algorithms in online monitoring of specific force coefficients in milling of isotropic metallic materials (i.e. Aluminum). Numerical simulations and experimental studies are presented to verify the effectiveness of the proposed methods in identifying the SFC in various cutting conditions.

Chapter 4 presents the development of mechanistic force model in metallic materials to CFRP composites milling by replacing its constant coefficients with periodic functions of fibre cutting angle. Performances of the presented methods RLS and KF are validated by numerical simulations and experimental studies. Milling both uni-directional and multi-directional CFRP layups are considered in the presented simulations and experiments.

Chapter 5 of the thesis is dedicated to discussing the ways that the presented modeling methods in previous chapters can be used to enhance the composite material machining process.

Finally, Chapter 6 summarizes the key findings, contributions and suggestions for future work based on the outcomes of three research studies presented in Chapter 2 to 5.

Chapter 2

Modeling and Identification of Cutting Forces in Milling of CFRP

This chapter has been published in the journal of Materials Processing Technology, Volume 280, June 2020, 116595. [1]

This chapter was a collaborative work in DDM research group at University of Victoria. The contribution from each author is as following:

- Raimund Mullin: Software, Validation, Formal analysis, Investigation, Resources, Data Curation, Writing – Original Draft, Visualization.
- Mehran Farhadmanesh: Methodology, Software, Initial analysis, Visualization, Review and Editing.
- Amirali Ahmadian: Validation, Data Curation.
- Keivan Ahmadi: Conceptualization, Formal analysis, Visualization, Writing – Review and Editing, Supervision, Project administration, Funding acquisition.

2.1 Introduction

High strength to density ratio and corrosion resistance of CFRPs have made them a great alternative to replace metallic materials in a wide range of applications. Composite parts are usually made to near net shape using autoclave molding, compression

[1] https://doi.org/10.1016/j.jmatprotec.2020.116595

molding, or fillament winding [5], but they often require machining operations such as drilling and milling in the assembly stage of production [1, 6]. At this last stage, damages (e.g. delamination and fibre pull-out) may happen due to excessive cutting forces. To avoid such damages, cutting force models that relate machining parameters to the resulting cutting forces are essential, because such models enable selecting the cutting parameters that would result in minimum machining damages.

Modelling milling forces in metal cutting is a well-studied topic [43, 44, 45, 46]. Linear mechanistic force modelling is widely used as an efficient method to compute milling forces [43]. In this method, cutting forces are modelled as linear functions of the uncut chip cross section area, which is determined by chip thickness and axial depth of cut. The coefficients of the linear model, known as cutting and edge force coefficients, are calibrated experimentally using the machining forces measured during milling operations.

Budak et al. [45] developed the method known as orthogonal to oblique transformation, which allows computing the cutting and edge force coefficients based on the shear plane angle, friction coefficient, and the material's shear flow stress obtained from the classical orthogonal cutting tests. When these parameters are not available, or when the geometry of the cutting edge includes complex features such as chip breaker or chamfer, Armarego and Whitfield [47] proposed a method to determine the cutting and edge force coefficients based on the average forces that are measured during a set of milling operations with various feedrates. Because the average forces are used in this method, runout, measurement noise, and vibrations do not affect the accuracy of the identified parameters. This identification method, however, requires the measurement of milling forces in a large set of feedrates, and the resulting model parameters are only applicable to the spindle speed and tool/workpiece combinations that were used in the identification tests. Fu et al. [48] used a force model that considers the normal and friction forces on the rake face, neglecting the edge forces, and presented an identification method based on the average forces measured during one milling test. Other researchers such as Gonzalo et al. [49], Grossi et al. [50], and Rivière-Lorphèvre and Filippi [51] used optimization methods to determine the cutting and edge force coefficients from the instantaneous cutting forces, rather than the average forces. Rubeo and Schmitz [52] presented a comparison of the performance of the identification methods that are based on the average forces versus the ones that are based on the instantaneous forces.

Mechanics of chip formation in CFRP machining strongly depends on fibre cut-

ting angle – the angle between the fibre that is being cut and the direction of cutting speed. Sheikh-Ahmad [1] summarized the failure mechanisms that lead to chip formation in various fibre cutting angles to combinations of intralaminar delamination, buckling, shear, and fracture. In milling, fibre cutting angle and consequently the chip formation mechanics changes continuously as the tool rotates. Mechanistic force modelling has been also used to address this variation in modelling CFRP milling forces. Sheikh-Ahmad et al. [53] used multiple regression analysis and committee neural network approximation to develop a mechanistic CFRP milling force model. Su et al. [54] adopted the orthogonal cutting model of Merchant [55] to develop a set of equations that relate the cutting and edge force coefficients in milling of woven-CFRP layers to the instantaneous fibre cutting angle and the mechanical properties of the fibres. Haiyan and Xuda [56] used a linear mechanistic force model with constant coefficients to describe the forces in helical milling of Uni-Directional (UD) CFRP. Although constant coefficients were used in the mechanistic model, they used an empirically determined calibration constant to compensate for the variation of force coefficients in continually varying fibre cutting angles. Karpat et al. [57] mechanistically modelled CFRP milling forces by adopting the linear mechanistic force model that is used in milling of metallic materials. In order to account for the variation of chip formation mechanics in various tool rotation angles, they assumed that the edge and cutting force coefficients are sinusoidal functions of fibre cutting angle. The constant coefficients of the sinusoidal functions were determined using the least-squares curve fitting of the milling forces measured using a rotary dynamometer. Experimental validations in the work of Karpat et al. [57] confirmed that this simple adaptation of the linear mechanistic cutting force model leads to fairly accurate predictions of CFRP milling forces. The identification method that Karpat et al. used utilizes the instantaneous cutting forces, and is therefore biased due to the effect of runout, vibrations, initial immersion angle, and noise.

In this chapter, similarly to the approach of Karpat et al. [57], an adaptation of the linear mechanistic model is used for CFRP milling. The edge and cutting force coefficients are, however, assumed to be periodic functions of fibre cutting angle. The periodic functions are represented by their Fourier series expansions, and a new method is introduced to identify the coefficients of the Fourier series from the average forces measured in a set of UD-CFRP milling operations. Because average – and not instantaneous – forces are used in the presented identification method, the estimated coefficients are not affected by runout, vibrations, noise, and the initial immersion

angle. After identifying the parameters of the linear mechanistic force model from UD-CFRP milling operations, the force model is used to predict milling forces in arbitrary Uni-Directional as well as Multi-Directional CFRP layups.

After describing the geometrical model of CFRP milling in the next section, the linear mechanistic cutting force model is explained in Section 2.3. A new method for the identification of the force model parameters is proposed in Section 2.4. Implementation of the proposed modelling approach is explained using the experimental study presented in Section 2.5. This experimental study is also used to discuss the efficiency of the model in predicting CFRP milling forces in arbitrary cutting conditions.

2.2 Geometrical Modelling

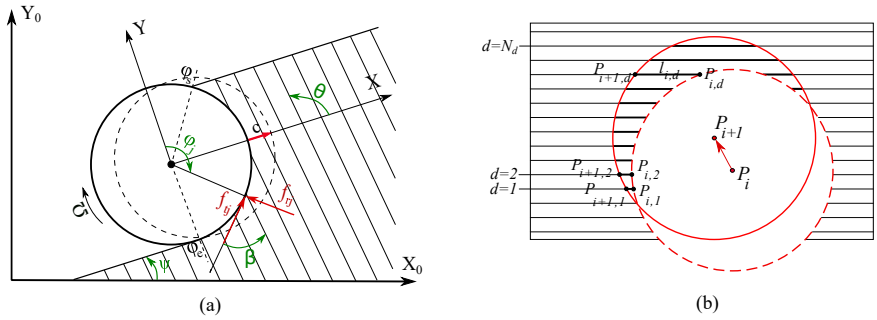

Figure 2.1: (a) Feed, X, and normal, Y, directions; fibre cutting angle, β, fibre orientation of a Uni-Directional layer, θ, and angular immersion angle ϕ; tangential, F_t and radial F_r force components. (b) Geometrical model of fibre cutting during milling

Figure 2.1 shows the geometrical model of 2D milling of Fibre Reinforced Polymers. The global coordinate system in part (a) of the figure, denoted X_0Y_0, is a stationary coordinate system that is used to describe the resulting milling forces. This coordinate system, for example, could be aligned with the X and Y axis of the machine tool. The XY coordinate system is attached to the centre of the tool and its X and Y axis are aligned with the feed and normal to feed directions, respectively. Feed direction is assumed to be at ψ angle with respect to X_0. The tool is assumed to have N cutting edges indexed as $j = 1..N$. The uniform pitch angle between consecutive flutes is $\phi_p = 2\pi/N$. The instantaneous angular immersion of the j^{th} cutting flute is measured from Y-axis and is denoted $\phi_j(t)$. Assuming that the first

flute ($j = 1$) starts its motion from Y-axis, instantaneous immersion angle of each flute is expressed in terms of the spindle rotational speed, Ω in rad/sec, and pitch angle, ϕ_p:

$$\phi_j(t) = \text{mod}\,(\Omega t + (j-1)\phi_p, 2\pi) \tag{2.1}$$

where mod () stands for modulo operation. The cutting edges are engaged with the workpiece when their immersion angle is between start(ϕ_s) and exit(ϕ_e) angles. These angles depend on the tool diameter, D, and the radial immersion, b, as shown in Figure 2.1(a). The thickness of the chip that is removed by each tooth depends on feed per revolution per tooth, c, and immersion angle, ϕ_j:

$$h(\phi_j) = c\sin(\phi_j) \tag{2.2}$$

The orientation of each fibre with respect to X_0 is denoted θ. For Uni-Directional (UD) layers, θ is constant for all of the fibres, but in Multi-Directional (MD) layers θ varies from one fibre to another. Fibre cutting angle, β, is the angle between the fibre that is being cut and cutting speed direction, i.e. the tangential direction, t. The tangential and radial directions at each flute are shown with t and r, respectively. In UD layers, the instantaneous fibre cutting angle can be expressed in terms of angular immersion, $\phi_j(t)$, and fibre orientation, θ:

$$\beta(t) = \text{mod}\,(\phi_j(t) - \psi + \theta, \pi) \tag{2.3}$$

In this work, following the convention adopted by Karpat in [57], positive fibre cutting angle is measured counter clockwise from negative cutting speed direction. In some references, this angle is measured clockwise from positive cutting speed direction.

Cutting forces are usually simulated in discrete time domain where the duration of the process is discretized into N_t time steps and the cutting forces are computed at each discrete moment, $t_i, i = 1..N_t$. In UD composites and a simple toolpath, the fibre cutting angle at each simulation time step is obtained from Equation (2.3) as $\beta(t_i)$. In MD composites or when a complex toolpath is used, graphical methods such as the dexel-based method presented in [8] can be used to determine fibre cutting angle at each time step. In dexel-based methods, each fibre is represented by a dexel, as shown in Figure 2.1(b). In this figure, fibres are indexed as $d = 1, 2, ..., N_d$, where N_d is the total number of fibres in the model. At each simulation time step, the

intersection of dexels with the circular envelope of the milling tool are computed and used to obtain the length and angle of the fibres being cut. For example, in Figure 2.1(b), the intersections of the dexels (i.e. fibres) with the tool at t_i are obtained as $P_{i,d}$, and the intersection points in the following time step, t_{i+1} are obtained as $P_{i+1,d}$, where $d = 1, 2, ...$ are the indices of the fibres (dexels) in the graphical model. The length of the fibres being cut at the i^{th} time step, $l_{i,d}$, are computed as:

$$l_{i,d} = |P_{i+1,d} - P_{i,d}| \, ; d = 1, 2, ..., N_d \tag{2.4}$$

Fibre cutting angle at t_i is obtained with respect to the instantaneous cutting speed direction and the orientations of the fibres being cut:

$$\begin{cases} \beta_{i,d} = (\pi/2) + \cos^{-1}(n_1.n_2) & \text{Clockwise rotation} \\ \beta_{i,d} = (\pi/2) - \cos^{-1}(n_1.n_2) & \text{CounterClockwise rotation} \end{cases} ; \tag{2.5}$$

where n_1 and n_2 are normal vectors in the fibre and radial directions, respectively:

$$n_1 = \frac{(P_{i+1,d} - P_{i,d})}{|P_{i+1,d} - P_{i,d}|}; n_2 = \frac{(P_{i,d} - P_i)}{|P_{i,d} - P_i|} \tag{2.6}$$

2.3 Mechanistic Cutting Force ModelS

Because axial forces are usually minimized in CFRP milling (to avoid delamination), only lateral forces are considered in this study, although the extension to consider axial forces is trivial. The cutting forces applied in radial and tangential directions on each flute are expressed as linear functions of the instantaneous uncut chip thickness, $h(\phi_j)$:

$$\begin{aligned} f_{tj} &= K_{tc}(\beta) a h(\phi_j) + K_{te}(\beta) a; \\ f_{rj} &= K_{rc}(\beta) a h(\phi_j) + K_{re}(\beta) a \end{aligned} \tag{2.7}$$

where a is the axial depth of cut, K_{tc} and K_{rc} are cutting force coefficients in tangential and radial directions, and K_{te} and K_{re} are edge force coefficients. Mechanics of chip formation strongly depends on the fibre cutting angle, which changes at various immersion angles, as described in Section 2.2. To account for the variation of chip formation mechanics at various fibre cutting angles, the cutting and edge force coefficients are assumed to be functions of the fibre cutting angle, β. Because fibre cutting angle varies between zero and π, cutting and edge force coefficients are also assumed

to be periodic with the fundamental period of π. As a result of this assumption, cutting and edge force coefficients are expressed as the following Fourier series:

$$K_{pq}(\beta) = \sum_{i=0}^{M} C_i^{pq} \cos(2i\beta) + S_i^{pq} \sin(2i\beta) \quad , p = t, r; \quad q = c, e \tag{2.8}$$

In Section 2.4, an experimental method is proposed to determine the Fourier coefficients of the cutting and edge force coefficients, C_i^{pq} and S_i^{pq}.

The overall forces applied on the tool are obtained by projecting the radial and tangential forces from each flute onto the global X_0 and Y_0 directions, and then summing the forces from all of the flues:

$$\begin{gathered} \left\{ \begin{array}{c} f_{x0} \\ f_{y0} \end{array} \right\} = T_x^{x_0} \sum_{j=1}^{N} g(\phi_j) T_t^x \left\{ \begin{array}{c} f_t j(\phi_j) \\ f_r j(\phi_j) \end{array} \right\} ; \\ T_t^x = \left[\begin{array}{cc} -\cos(\phi_j) & -\sin(\phi_j) \\ \sin(\phi_j) & -\cos(\phi_j) \end{array} \right] ; T_x^{x_0} = \left[\begin{array}{cc} \cos(\psi) & -\sin(\psi) \\ \sin(\psi) & \cos(\psi) \end{array} \right] \end{gathered} \tag{2.9}$$

where $g(\phi_j)$ is a Heaviside function that determines whether if the cutting edge is engaged with the workpiece or not:

$$g(\phi_j) = H(\phi_j - \phi_s) - H(\phi_j - \phi_e) \tag{2.10}$$

2.4 Identification of Force Model Parameters

As shown in Equation (2.9), milling forces vary periodically with the fundamental period being $2\pi/\Omega N$. The constant term in the Fourier expansion of the periodic forces (i.e. their average value) is obtained by integrating Equation (2.9) over one fundamental period:

$$\begin{gathered} \bar{\mathbf{f}} = \left(\tfrac{N\Omega}{2\pi}\right) \sum_{j=1}^{N} \int_{0}^{2\pi/\Omega N} T_x^{x_0} g(\phi_j) T_t^x \left\{ \begin{array}{c} f_t(\phi_j) \\ f_r(\phi_j) \end{array} \right\} dt \\ \bar{\mathbf{f}} = [\ \bar{f}_{x0} \quad \bar{f}_{y0} \ ]^T ; \end{gathered} \tag{2.11}$$

where the superscript T stands for transpose of a matrix, and $\bar{f}_{x0}$ and $\bar{f}_{y0}$ are the average forces in X_0 and Y_0 directions. For UD composites, assuming that the feed direction (ψ) is constant, by substituting $T_x^{x_0}$ and T_t^x from Equation (2.9) and $f_t j(\phi_j)$ and $f_r j(\phi_j)$ from Equation (2.7) in Equation (2.11), the average forces in X_0 and Y_0

directions are obtained as linear functions of the feedrate, c:

$$\bar{\mathbf{f}} = \mathbf{cb}\left(\psi,\theta\right); \\ \mathbf{c} = \begin{bmatrix} c & 1 & 0 & 0 \\ 0 & 0 & c & 1 \end{bmatrix}; \mathbf{b}\left(\theta,\psi\right) = \begin{bmatrix} a_x & b_x & a_y & b_y \end{bmatrix}^T \tag{2.12}$$

where coefficients a_x, a_y, b_x, and b_y are linear functions of the Fourier coefficients of $K_{tc}(\beta)$, $K_{rc}(\beta)$, $K_{te}(\beta)$,and $K_{re}(\beta)$:

$$\begin{aligned} &\mathbf{b}\left(\theta,\psi\right) = \mathbf{a}\left(\theta,\psi\right).\mathbf{K} \\ &\mathbf{K} = \begin{bmatrix} \mathbf{K}_{tc} & \mathbf{K}_{te} & \mathbf{K}_{rc} & \mathbf{K}_{re} \end{bmatrix}^T \\ &\mathbf{K}_{pq} = \begin{bmatrix} C_0^{pq} & C_1^{pq} & S_1^{pq} & C_2^{pq} & S_2^{pq} & \cdots & C_M^{pq} & S_M^{pq} \end{bmatrix}^T; \quad p = t,r; q = c,e \end{aligned} \tag{2.13}$$

Vector $\mathbf{K}$ contains the Fourier coefficients in Equation (2.8), and $\mathbf{a}\left(\theta,\psi\right)$ is a $4 \times (4 \times (2M+1))$ matrix that depends on the fibre orientation angle, θ, and the feed direction, ψ. Components of $\mathbf{a}\left(\theta,\psi\right)$ for $M = 1$ are given in Appendix A.

The process of identifying the cutting force coefficients involves two steps that are explained below.

Step 1- Let us assume that the cutting forces are measured in X_0 and Y_0 directions while milling a UD composite along a straight line at ψ angle with respect to X_0. If such measurements are repeated using a set of feedrates $(c_i, i = 1..n > 2)$ and the the average of the cutting forces in each test are computed numerically as $\bar{\mathbf{f}}_\mathbf{i}$, $i = 1..n$, an over-determined set of equations can be obtained from Equation (2.12) as follows:

$$\bar{\mathbf{F}} = \mathbf{Cb}\left(\psi,\theta\right); \mathbf{C} = \begin{bmatrix} \mathbf{c_1} \\ \vdots \\ \mathbf{c_n} \end{bmatrix}; \bar{\mathbf{F}} = \begin{bmatrix} \bar{\mathbf{f}}_\mathbf{1} \\ \vdots \\ \bar{\mathbf{f}}_\mathbf{n} \end{bmatrix} \tag{2.14}$$

where $\mathbf{c_i}$ are the $\mathbf{c}$ matrix at c_i. The least squares approximation of $\mathbf{b}\left(\psi,\theta\right)$ is obtained using the pseudo-inverse of the matrix of feedrates, $\mathbf{C}$:

$$\mathbf{b}\left(\psi,\theta\right) = \mathbf{C}^{+}\bar{\mathbf{F}} \tag{2.15}$$

where $+$ superscript stands for Moore-Penrose inverse:

$$\mathbf{C}^{+} = \left(\mathbf{C}^T\mathbf{C}\right)^{-1}\mathbf{C}^T \tag{2.16}$$

Step 2- Step 1 is repeated for a set of fibre orientation angles, $\theta_i, i = 1..m > 2M+1$, to obtain $\mathbf{b}(\psi, \theta_i)$ at each orientation. Subsequently, the following over-determined system of equations is constructed by writing Equation (2.13) for each fibre orientation:

$$\begin{aligned} \mathbf{B} &= \mathbf{A}.\mathbf{K} \\ \mathbf{B} &= \begin{bmatrix} \mathbf{b}(\theta_1, \psi) \\ \vdots \\ \mathbf{b}(\theta_m, \psi) \end{bmatrix}; \mathbf{A} = \begin{bmatrix} \mathbf{a}(\theta_1, \psi) \\ \vdots \\ \mathbf{a}(\theta_m, \psi) \end{bmatrix} \end{aligned} \tag{2.17}$$

The Fourier coefficients of $K_{tc}(\beta)$, $K_{rc}(\beta)$, $K_{te}(\beta)$,and $K_{re}(\beta)$ are estimated by the least squares approximation of the solution of Equation (2.17):

$$\mathbf{K} = \mathbf{A}^{+}\mathbf{B} \tag{2.18}$$

The implementation of the proposed identification method is explained using an experimental study presented in the next section. The experiments are also used to study the performance of the identified model in predicting CFRP milling forces.

2.5 Experimental Results

A 2-flute Tungsten Carbide end mill with 9.525 mm (3/8 inch) diameter and 3^o rake angle is used to mill a layup of UD CFRP plies with 0.8mm thickness (of each layer) and alternating 0 and 90 degrees directions. The experimental setup is shown in Figure 2.2. The experiments were conducted on a 3-Axis vertical CNC machine. Cutting forces were measured by a Kistler 9255 table dynamometer, and the measured signals were conditioned and amplified using a 5010B Kistler amplifier. A NI9234 data acquisition card was used to digitize the force signals at 25.6 KHz sampling rate. Cutpro application [58] was used to store and process the measured force signals.

In all of the experiments, axial depth of cut is kept constant at ($a = 0.8mm$ to ensure that only one UD ply is being cut. The spindle speed (Ω) is also kept constant at 5000 rev/min. Half-immersion up-milling ($\phi_s = 0, \phi_e = \pi/2$), down-milling ($\phi_s = \pi/2, \phi_e = \pi$), and full immersion ($\phi_s = 0, \phi_e = \pi$) cuts are performed at six different fibre orientations ($m = 6$), θ =0^o, 30^o, 60^o, 90^o, 120^o, and 150^o. At each fibre orientation, feed and normal cutting forces are measured at five different feedrates ($n = 5$), $c = 0.02, 0.04, 0.06, 0.08$, and 0.1 mm/rev/flute. In each test, the feed direction (ψ) was chosen according to the orientation of the ply being cut

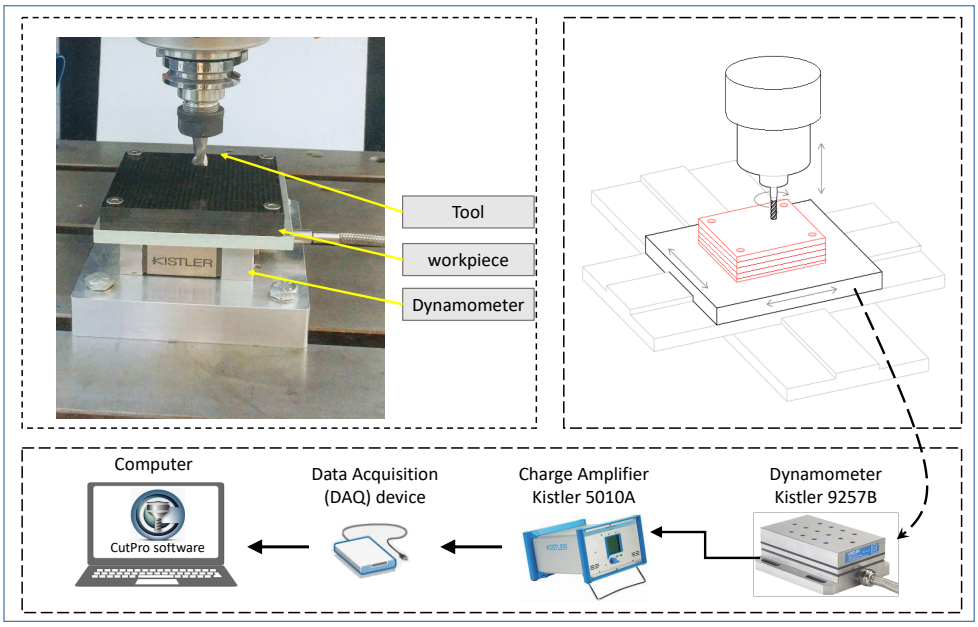

Figure 2.2: Test setup

(0 or 90 degrees) to create the targeted fibre orientation angle θ. Nevertheless, the measured forces in the two in-plane directions of the dynamometer (i.e. X_0 and Y_0) were projected in the respective feed (X) and normal (Y) directions and thus $\psi = 0$ is used in the analysis presented in this section. The generated axial forces depend on the fibre orientation in each test, but they are generally much smaller than the resultant side (lateral) forces. For example, the resultant side forces and the corresponding axial forces in two of the conducted tests are shown in Figure 2.3. Regardless, because axial forces are uncoupled from the forces in tangential and radial direction, they do not affect the identification of tangential and radial force coefficients. Since downmilling resulted in a better surface finish and a fewer fibre pullouts, the measured downmilling forces are used for the identification of force model parameters; the measured upmilling and full-immersion forces are used for verifying the accuracy of the identified model in predicting CFRP milling forces.

Fourier expansions of the cutting force coefficients (Equation (2.8)) are truncated at the first harmonic term ($M = 1$), leading to 12 unknown model parameters that need to be determined ($C_0^{pq}, C_1^{pq}, S_1^{pq}; p = t, r; q = c, e$). The two-step algorithm presented in Section 2.4 is used to identify these 12 parameters from the feed and normal forces measured during the thirty (5 feedrates$\times$ 6 fibre orientations) downmilling tests. In what follows, the results of each step of identification are presented.

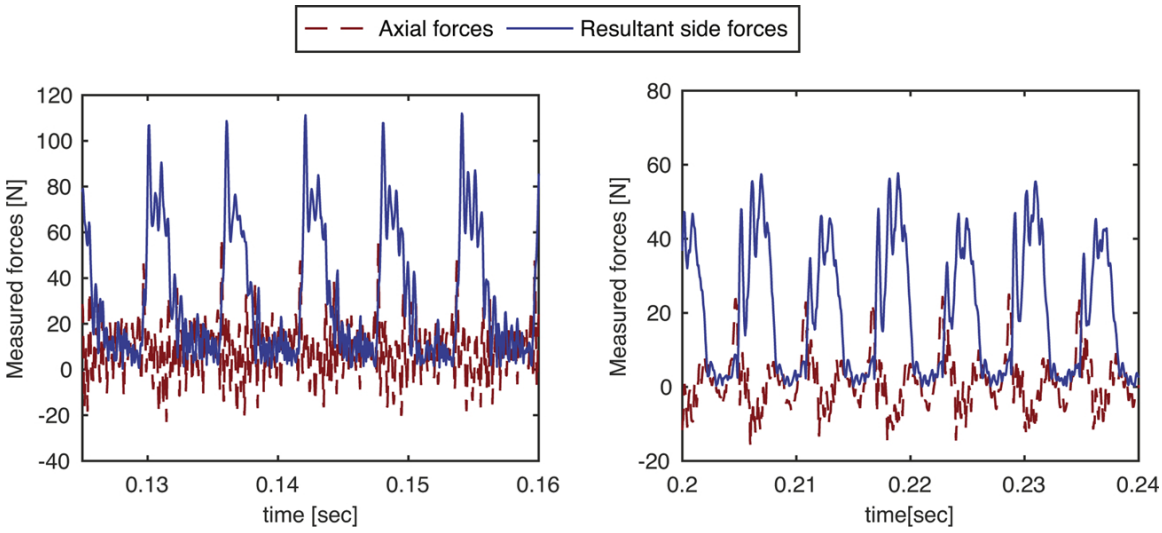

Figure 2.3: Resultant side forces and axial forces measured at 0.06 mm/tooth feedrate, 2000 rev/min spindle speed, half-immersion downmilling with 0.8mm axial depth of cut and left $\theta = 30°$(left) and $\theta = 150°$(right) fibre orientations.

Step 1- Figure 2.4 shows the average of the measured forces in X and Y directions ($\bar{f}_x = \bar{f}_{x0}$ and $\bar{f}_y = \bar{f}_{y0}$, because $\psi = 0$) at the $n = 5$ tested feedrates in each of the $m = 6$ fibre orientations. This figure also shows the least squares approximation (Equation (2.15)) of the linear relationship between the average forces and feedrate as described in Equation (2.12).

If CFRP is treated as an isotropic material in each of the tested $m = 6$ fibre orientations, the resulting slope (a_x and a_y) and intercepts (b_x and b_y) of the approximated lines can be used to obtain the equivalent isotropic cutting (K^e_{tc} and K^e_{rc}) and edge (K^e_{te} and K^e_{re}) force coefficients. The relationships for half-immersion, downmilling, are as follows [43]:

$$\begin{aligned} K^e_{tc} &= \tfrac{4\pi(2a_x+\pi a_y)}{a(\pi^2+4)};\ K^e_{rc} = \tfrac{-4\pi(-2a_y+\pi a_x)}{a(\pi^2+4)} \\ K^e_{te} &= \tfrac{\pi}{2a}\left(b_y + b_x\right);\ K^e_{re} = -\tfrac{\pi}{2a}\left(b_x - b_y\right) \end{aligned} \tag{2.19}$$

Figure 2.5 shows the equivalent cutting and edge force coefficients that are obtained for each of the tested fibre orientations. As expected, both the tangential and radial force coefficients strongly depend on the fibre orientation. Edge force coefficients in some of the fibre orientations are negative, which is physically infeasible. This error is partly associated with the fact that a linear relationship is assumed between chip thickness and the resulting forces (Equation (2.7)). While this assumption

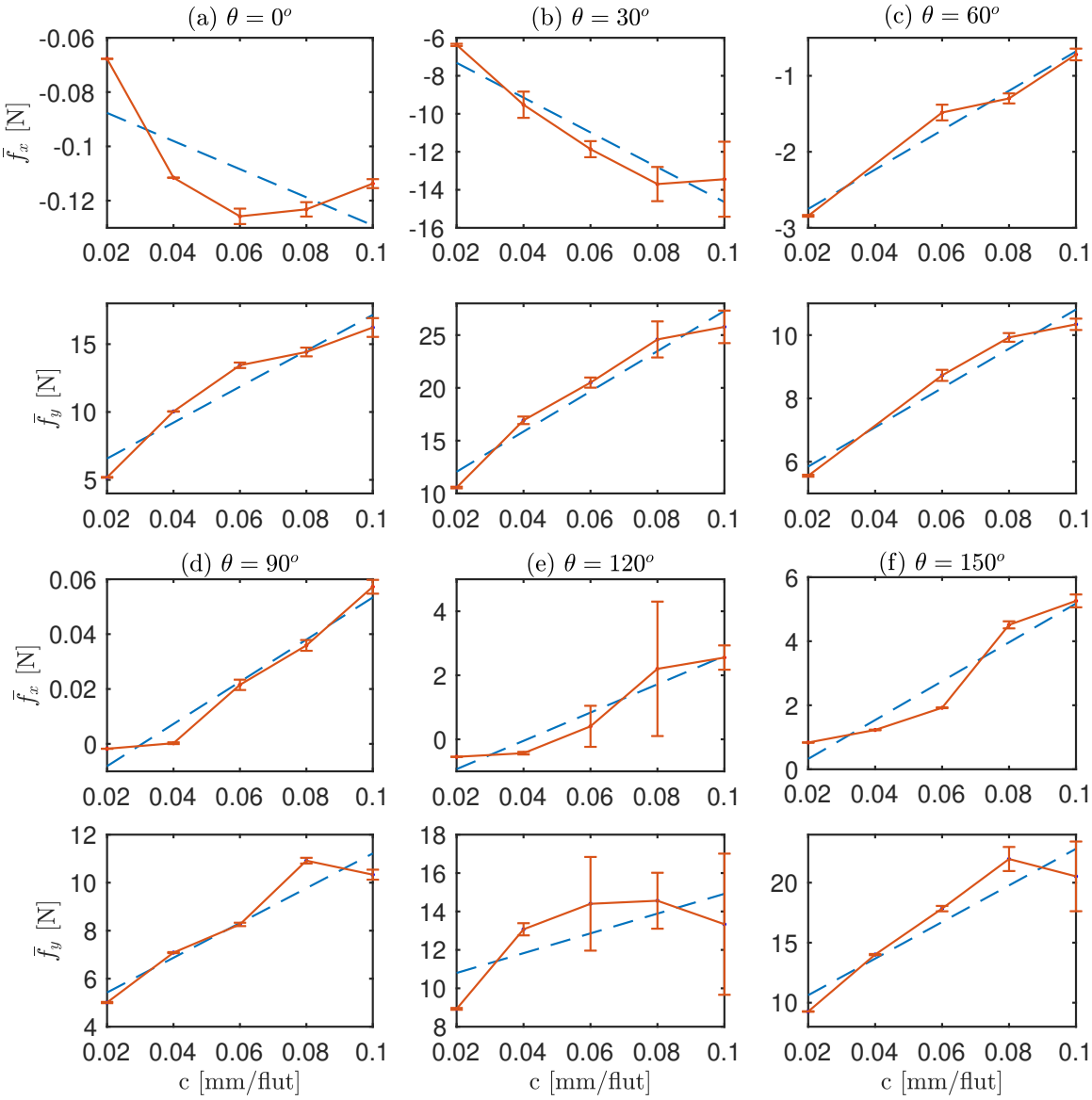

Figure 2.4: Average measured cutting forces in half-immersion, Downmilling, tests in various fibre orientations, θ. Average of the force in feed direction is $\bar{f}_x$ and in normal direction is $\bar{f}_y$. Axial depth of cut $a = 0.8$ mm, and spindle speed $\Omega = 5000$ rev/min

may be reasonable in a certain range of fibre cutting angles, machining forces exhibit strong nonlinearities with respect to the chip thickness in other fibre orientations [1].

For example, as shown in Figure 2.4(a), the average feed forces ($\bar{f}_x$) are negligible when fibres are parallel to the feed direction ($\theta = 0$), and they vary nonlinearly with respect to feedrate. The negative edge force coefficients may also be attributed to the

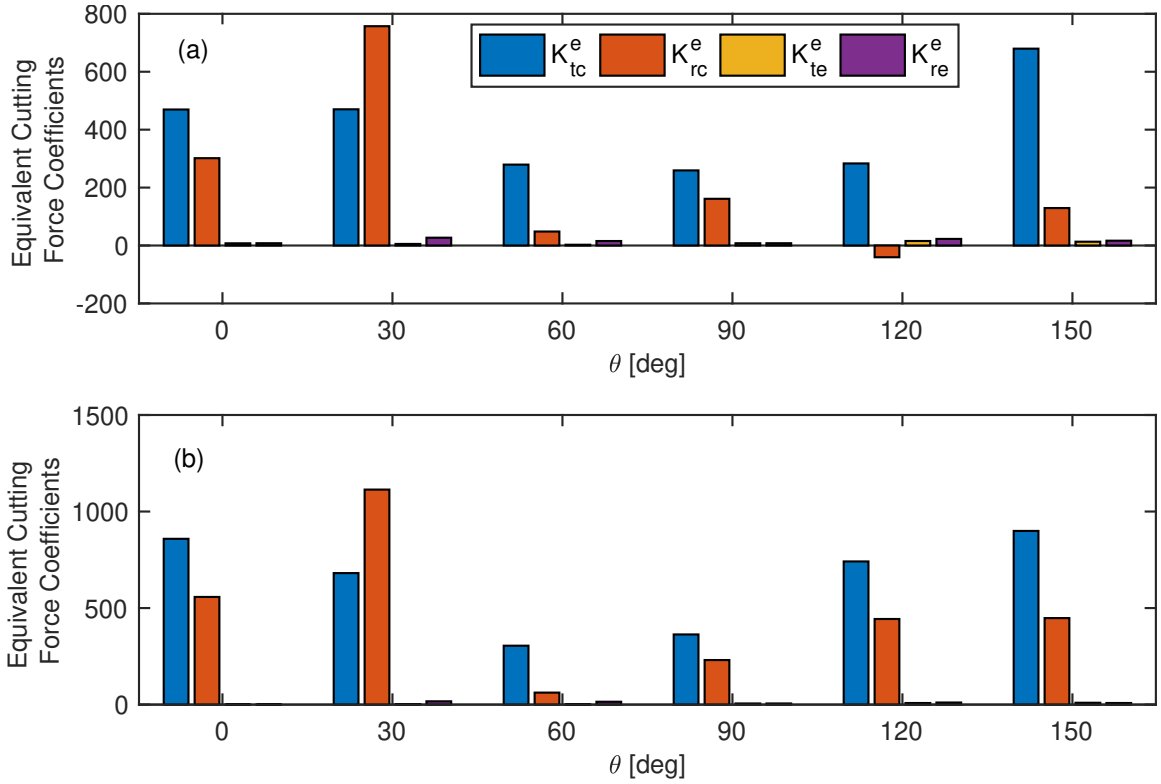

Figure 2.5: Equivalent Cutting Force Coefficients in half-immersion Downmilling tests. (a) using standard least squares, Equation (2.15), and (b) using weighted least squares, Equation (2.20)

errors in the computation of the average forces. Average forces during one cut may vary considerably due to disturbances caused by material inhomogeneity or pulled out and uncut fibres. In order to study the variation of the average forces during each test, the total length of the measured forces during one test is divided into twenty equal segments and the average of the forces in each segment is computed numerically. The error bar on each of the points shown in Figure 2.4 represents the variance of the twenty force averages. As shown in this figure, in some of the tests, the average of the forces change substantially during the experiment due to excessive fibre pullouts or inconsistencies in the material. In order to reduce the effect of the tests with high average force variation, Weighted Least Squares Approximation [59] is used instead of the standard least squares in Equation (2.15):

$$\mathbf{b}\left(\psi,\theta\right) = \mathbf{C}_w^{+}\bar{\mathbf{F}}_w \tag{2.20}$$

where $\mathbf{C}_w$ and $\bar{\mathbf{F}}_w$ are weighted regression matrix and average force vector, respec-

tively:

$$\mathbf{C}_w = \mathbf{WC},\ \bar{\mathbf{F}}_w = \mathbf{W}\bar{\mathbf{F}} \tag{2.21}$$

The weighting matrix,$\mathbf{W}$, is defined as the diagonal matrix containing the inverse squared variance of the average measured forces at each tested feedrate:

$$\mathbf{W} = diag\left(1/\sigma_{x1}^2, 1/\sigma_{y1}^2, \cdots, 1/\sigma_{xn}^2, 1/\sigma_{yn}^2\right) \tag{2.22}$$

where σ_{x_i} and σ_{yi}, $i = 1..n$, are respectively the variance of the average forces measured in X and Y directions at the feedrate c_i.

Figure 2.5(b) shows the equivalent cutting and edge force coefficients when weighted least squares is used to approximate the slope and intercepts of the line in Equation (2.15). Compared to Figure 2.5(a), when weighted least squares approximation is used, the trend of variation of cutting and edge force coefficients remain similar but the magnitudes of edge force coefficients are all positive. Nonetheless, considering the substantial variation of the equivalent force coefficients by fibre orientation (θ), no single set of constant coefficients is suitable for computing the milling forces in arbitrary fibre orientations and cutting conditions

Step 2- In the second step of identification, the estimated values of $\mathbf{b}(\psi, \theta)$ at $\theta = 0^o$,30^o,60^o,90^o,120^o, and 150^o are used in Equation (2.18) to approximate the Fourier coefficients of $K_{tc}(\beta)$, $K_{rc}(\beta)$, $K_{te}(\beta)$,and $K_{re}(\beta)$. The resulting Fourier coefficients, shown in Table 2.1, are used in Equation (2.8) to describe the variation of the cutting force coefficients when the fibre cutting angle (β) varies between 0 and π; the resulting functions are shown in Figure 2.6. Unlike the constant equivalent cutting and edge force coefficients shown in Figure 2.5, because the identified sinusoidal functions are independent of the fibre orientation (β), they can be used to compute forces in arbitrary fibre orientation and cutting conditions.

Table 2.1: Fourier coefficients of $K_{tc}(\beta)$, $K_{rc}(\beta)$, $K_{te}(\beta)$,and $K_{re}(\beta)$

Force Coefficients	Fourier Coefficients		
	C_0	C_1	S_1
$K_{tc}(\beta)[MPa]$	641.5	-296.5	-235.1
$K_{te}(\beta)[N/mm]$	4.7	-9.6	6.4
$K_{rc}(\beta)[MPa]$	475.9	-131.1	-275.2
$K_{re}(\beta)[N/mm]$	9.6	8.7	7.5

In order to verify the accuracy of the identified force model in predicting forces in

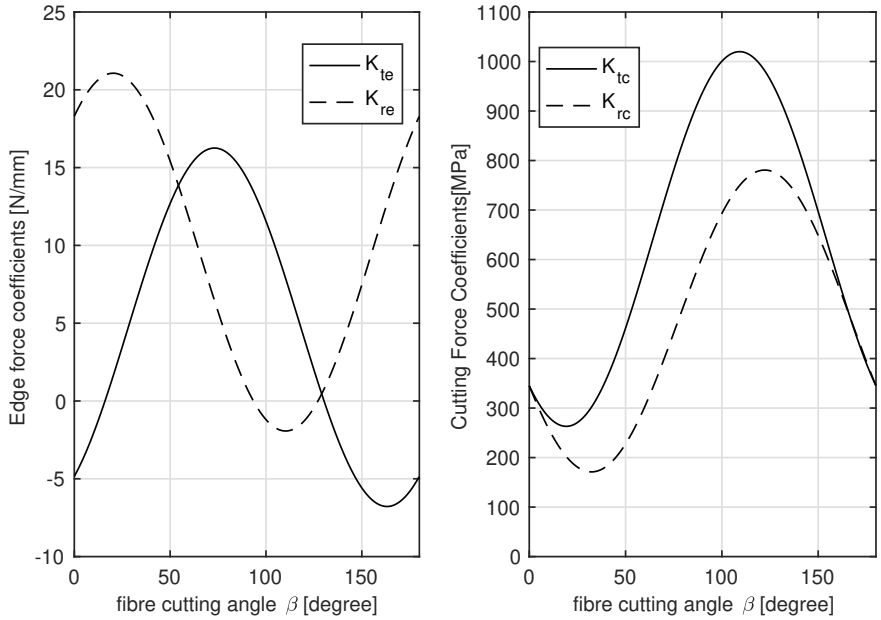

Figure 2.6: Identified functions describing cutting (K_{tc},K_{rc}) and edge force (K_{te},K_{re}) coefficients

arbitrary milling operations, the periodic cutting force coefficients shown in Figure 2.6 are used in the mechanistic force model described in Section 3.5 to simulate the cutting forces in half-immersion downmilling, upmilling, and full-immersion cuts at $c = 0.06$ mm/rev/tooth, $\Omega = 5000$ rev/min, and $a = 0.8mm$. The resulting simulated and measured milling forces when fibre orientations are $\theta = 30, 90$, and 150 degrees are shown in Figure 2.7.

Because the downmilling forces shown in Figure 2.7(a-c) are among the forces used for the identification the force model, the comparison of the measured and simulated forces in parts (a) to (c) of this figure only verifies the accuracy of the two-step least squares curve fitting process presented in Section 2.4. The upmilling and full-immersion forces shown in parts (d) to (i) of Figure 2.7 were not used in identification and therefore the comparison of the measured and simulated forces in those cases are used to verify the accuracy of the identified force model to predict forces in arbitrary milling operations.

As shown in Figure 2.7, the simulated forces agree well with the measured ones, although force underestimation is also visible in some cases– for example, in the tests shown in parts (a) and (f).

Figure 2.8 shows the variation of the fibre cutting angle and chip thickness during a half tool revolution cycle ($0^o < \phi < 180^o$) in the half-immersion downmilling test with

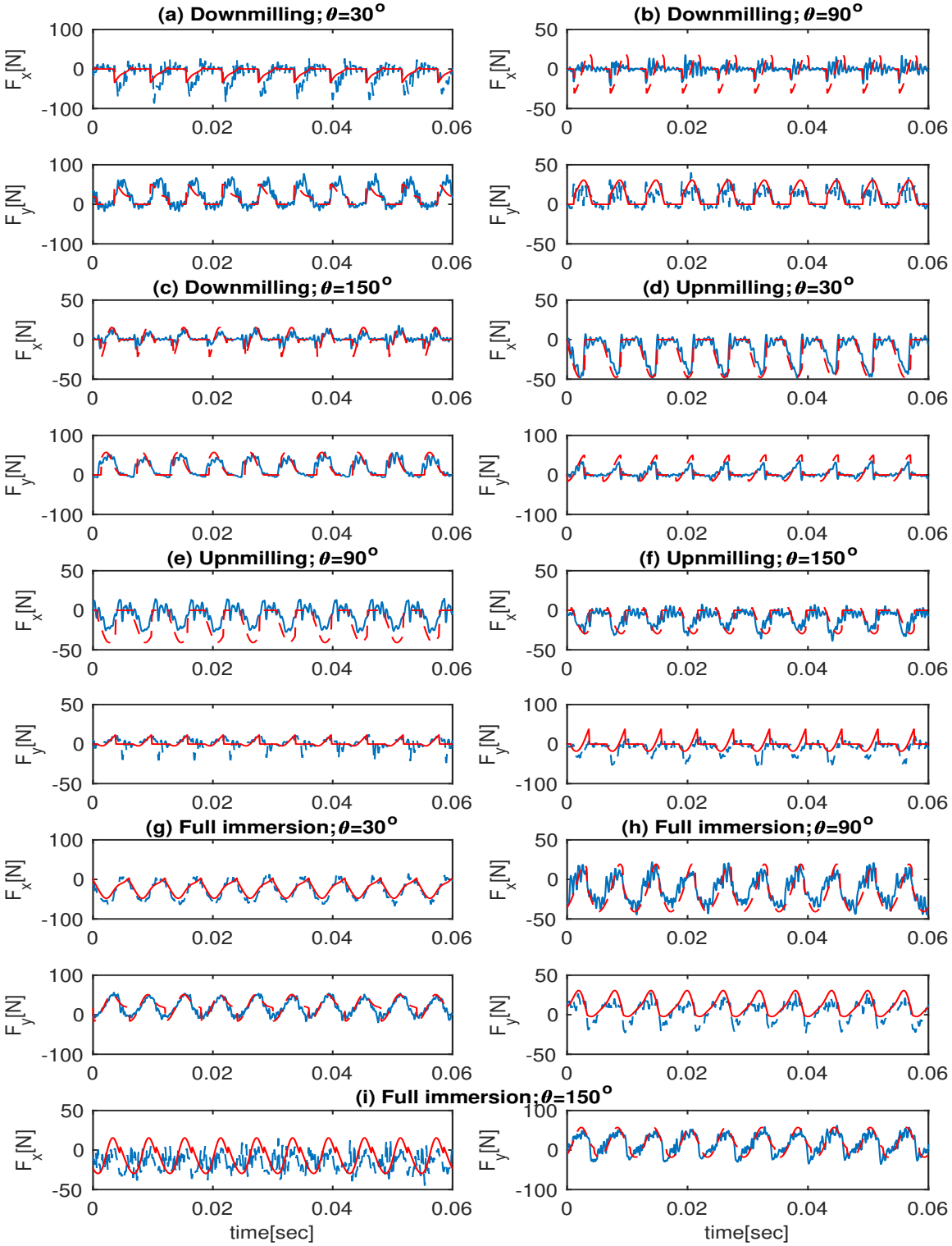

Figure 2.7: Simulated and measured forces in UD CFRP milling tests. Simulated forces are shown in red solid line, and the measured forces in blue dashed line

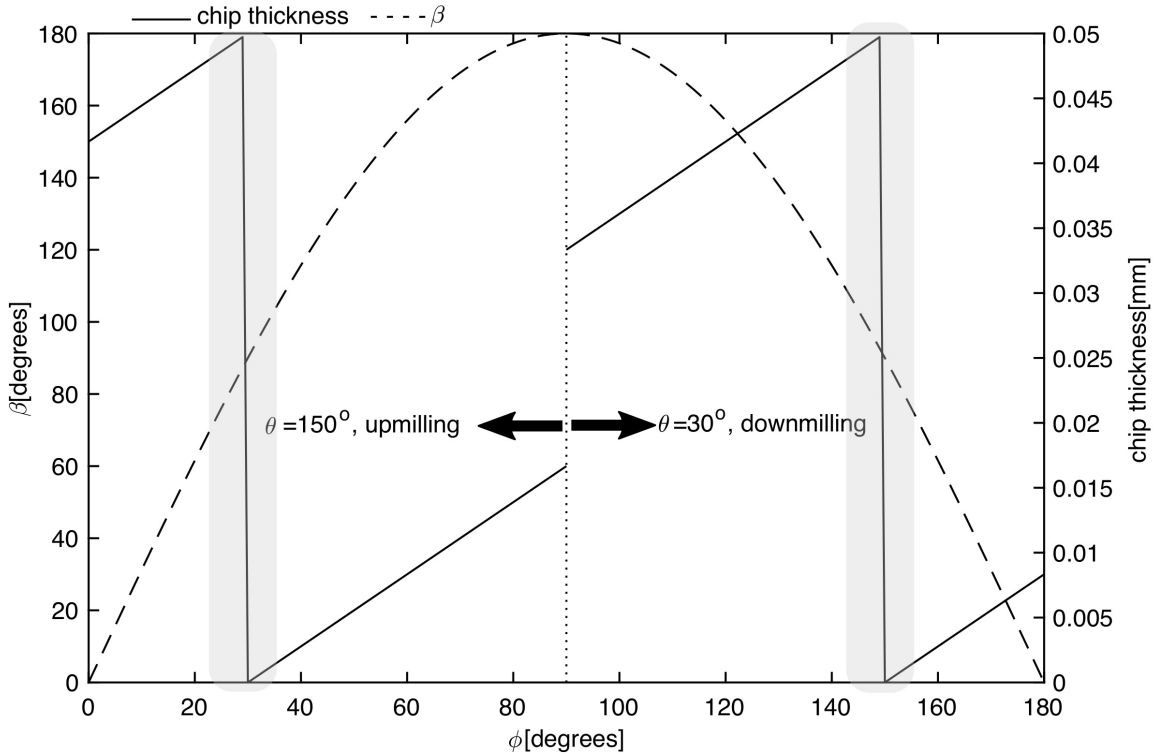

Figure 2.8: Variation of the fibre cutting angle, β, and chip thickness during the half-immersion downmilling test at $\theta = 30^o$ (right) and half-immersion upmilling test at $\theta = 150^o$ (left).

$\theta = 30^o$ (shown in Figure 2.7(a)) and half-immersion upmilling test with $\theta = 150^o$ (shown in Figure 2.7(f)). As shown in this figure, in both of the tests, fibre cutting angle reaches $\beta = 180^o$(i.e. $\beta = 0^o$) at the highlighted rotation angles. Similar changes in fibre cutting angle and consequently underestimation of forces is observed in the downmilling test with $\theta = 60^o$ and upmilling test with $\theta = 120^o$. Force underestimation in these cases might be explained due to the fundamentally different chip formation mechanics in the vicinity of zero degrees fibre cutting angle. As discussed in detail by Sheikh-Ahmad in [1], chip formation in zero degrees is initiated by buckling (if rake angle is negative) or Mode I fracture at the interface between fibres and matrix (if rake angle is positive), followed by bending and eventually fracture of fibres. In fibre cutting angles away from zero degrees, chip formation is initiated by compression-induced fibre shearing (when $\theta > 90^o$) or by delamination caused by severe fibre bending (when $\theta > 90^o$). After initiation, chip continues to form by intralaminar shearing between fibre and matrix. Intralaminar shearing between fibre

and matrix is similar in shape to chip formation along the shear plane in ductile metals and thus the adaptation of the mechanistic cutting force model in Equation (2.7 leads to proper prediction of forces. Fibre fracture in zero degrees cutting is fundamentally different in mechanics and therefore the applied mechanistic force model may not be able to capture the variation of forces.

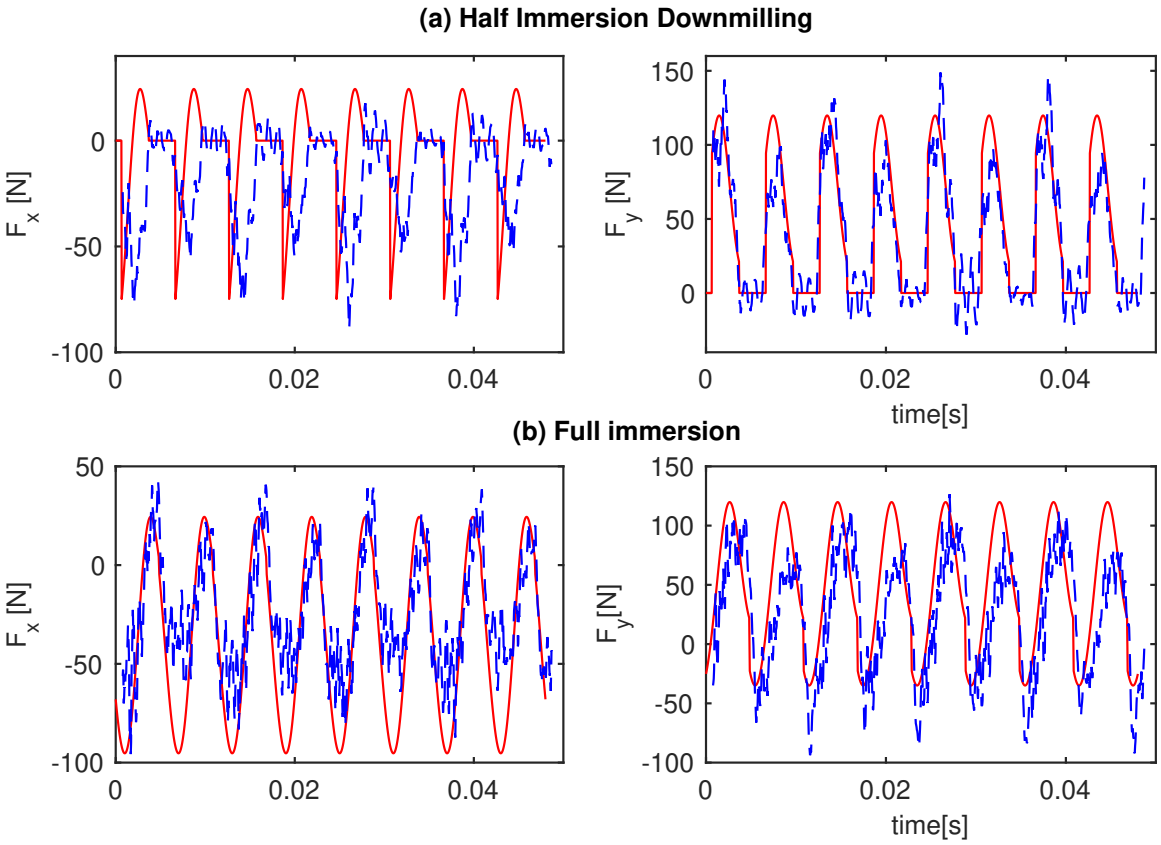

Figure 2.9: Simulated (red solid line) and measured(blue dashed line) forces in MD CFRP milling tests. Layup of plies $150/60/150^o$ and the thickness of each layer is 0.8mm. Spindle speed, $\Omega = 5000$ rev/min and feedrate is $c = 0.06$mm/rev/tooth for a two-fluted endmill.

The identified force model is also used to simulate milling forces when multiple plies with various fibre orientations are cut simultaneously. Figure 2.9 shows the measured and simulated forces when a layup of three 0.8 mm-thick plies with $\theta = 150/60/150^o$ fibre orientations are cut. Part (a) of the figure shows the forces in a half-Immersion downmilling experiment and part (b) shows the forces in a full-immersion test. Because the Kistler 9255 dynamometer (used in UD-CFRP tests) was no longer available at the time of performing MD-CFRP tests, a Kistler 9256C1

dynamometer was used to measure the forces. Milling forces in both tests were simulated by computing the contribution of each layer to the overall feed (F_x) and normal (F_y) forces. Except for the feed forces in downmilling, all of the simulated forces are in good agreement with the measured ones. Additional feed forces before the tool exits from the cut in downmilling (i.e. $\phi = 180^o$) are observed in Figure 2.9 (a). Similar to Figure 2.7(a) and (f), these additional forces could be associated with the mechanics of chip formation at fibres fibre cutting angle near zero degrees.

2.6 Conclusions

A mechanistic CFRP milling force model that considers the variation of the chip formation mechanics in various fibre cutting angles was presented. The cutting force coefficients are assumed to be periodic functions of fibre cutting angle. A new method was presented to identify the periodic cutting force coefficients based on the average milling forces measured during milling UD composite layers. The accuracy of the presented model and the identification approach were verified by comparing the simulated milling forces against the measured ones. Simulations also included milling of Multi-Direction CFRP layups. The verification tests showed that the presented modelling approach can predict the forces fairly accurately, but discrepancies between measured and predicted forces are observed when zero fibre cutting angles are encountered.

The presented method provides a practical approach for calibrating mechanistic cutting force models in various combinations of tools and composite materials; however, unavoidable characteristics of CFRP milling processes such as excessive tool wear, fibre pull-out, and fibre peeling will influence the accuracy of the presented model. Studying the linkage between the variation of the cutting force coefficients and the physics of chip formation at different fibre cutting angles may provide a better understanding of the mechanics of process.

Chapter 3

Online Identification of Mechanistic Milling Force Models in Milling Metallic Materials

This chapter has been published in the journal of Mechanical Systems and Signal Processing, Volume 149, 15 February 2021, 107318 [1]

3.1 Introduction

Computing milling forces based on process parameters is a critical requirement in designing optimal machining operations. Analytical, numerical, empirical, and mechanistic models are usually used to compute the forces generated in various machining operations [60, 61]. Such models are also integrated into computer simulations of the machining process, known as virtual machining systems, where the process is simulated and optimized in a computer environment before implementing it on a physical machine tool [62]. Except in machining operations with a basic cutting edge geometry, the parameters of cutting force models must be calibrated based on the forces measured during the process. The calibration process usually involves measuring the forces under various machining conditions (e.g. feedrates and spindle speeds), and then identify the model parameters using offline methods. Machining forces can be measured directly using commercial piezoelectric dynamometers or force sensors integrated in the structure of the machine tools [63]. They can also be estimated

[1] https://doi.org/10.1016/j.ymssp.2020.107318

indirectly from vibration [64, 65], or motor current measurements [66]. In addition to being costly and time-consuming, offline calibration does not provide any information about the evolution of the model parameters during machining. Force model parameters are strongly linked to the mechanics of chip formation, which evolves during the process due to various reasons such as tool wear or buildup edge formation. Because of this linkage, online identification of the force model parameters can be advantageous for process monitoring, where changes in force model parameters can be correlated to changes in process mechanics.

Analytical machining force models employ fundamental theories of chip formation mechanics to establish equations that relate the cutting forces to the machining parameters (e.g. feedrate) and the workpiece material's mechanical properties (e.g. shear strength, friction). The early work of Merchant [67], followed by the work of Lee and Shaffer [68] and Palmer and Oxley [69], and the mathematical foundations of slip-line models presented by Hill [70] are considered the basis for most of the analytical models that were developed later. Numerical methods such as Finite Element Analysis are also used to model machining forces, especially when complex material models, temperature dependent parameters, or micro-mechanics of the process are considered in modelling. Extensive reviews of the analytical and numerical force models are available in [71, 72]. In empirical modelling, the effects of machining parameters such as feedrate, depth of cut, and cutting speed are associated with the experimentally measured average forces by means of empirical equations [73, 74, 75]. Unlike analytical or numerical models, empirical modelling can be applied in machining processes with a complex tool geometry, workpiece material, and tool and workpiece engagement conditions. However, empirical equations serve as predictive models only and do not necessary represent the true mechanics of the process. Mechanistic models combine the physics-based nature of analytical and numerical models with the adaptability of empirical models by calibrating the parameters of physics-based models based on empirically measured cutting forces [76, 77, 78, 79]. As a result, the force model can be applied for complex cutting conditions, and at the same time, the parameters of the model are related to the mechanics of the process.

In linear mechanistic models, machining forces are formulated as linear functions of uncut chip thickness [79, 76, 77]. The constant coefficients of the linear model, usually referred to as Specific Force Coefficients (SFC), depend on the characteristics of the shearing action on the shear plane, friction on the rake face of the cutting edge, and the ploughing action under its flank face. Owing to their accuracy in predicting

the forces in a wide range of machining parameters, tool geometries, and workpiece materials, linear mechanistic force models are widely used to simulate forces in milling operations as well. Budak and Armarego [45] presented analytical equations that relate the SFC in general machining operations to the shear angle, friction coefficient, and shear flow stress of the material, which are determined empirically from standard orthogonal cutting tests [80]. This approach is also used to determine the SFC in milling operations, but when the orthogonal test parameters are not available or when the cutting edge has a complex geometry (e.g. chamfer, chip breaker), SFC are identified directly from the forces measured during the milling operation. Two different approaches can be used to identify (calibrate) the SFC [81] in milling. In the first approach [80], SFC are determined by performing a linear regression of the average forces measured at a set of different feedrates. This method requires measuring the milling forces (e.g. using force dynamometers) under various feed per tooth values, but because the average (and not instantaneous) forces are used, tool runout and vibrations do not affect the identified coefficients. In the second approach [49, 82], optimization methods are used to identify the SFC from instantaneous forces measured during the milling process. The coefficients in this approach can be identified from the forces measured under one feedrate only, but they are affected by tool runout and vibrations. In both of the approaches, SFC are identified offline, and they are applicable only for the specific tool geometry and range of cutting speeds, feedrates, and depth of cuts that were used in calibration tests.

Online monitoring of machining forces is an effective method for tool condition monitoring [83], however, in addition to tool wear and breakage, machining forces are also affected by changes in cutter-workpiece engagement and machining parameters. Therefore, tool condition monitoring using the force signal requires a complex use of Virtual Machining Systems [84] or signal processing methods [83] to remove the effect of cutter-workpiece engagement and machining parameters. Specific Force Coefficients, on the other hand, are mainly affected by the mechanics of chip formation only. As a result, SFC provide more sensitive measures for tool condition monitoring. For instance, Lin and Yang [85], and later, Choudhury and Rath [86] used the relationship between flank wear and the average SFC to estimate the extent of tool wear in milling processes. In their work, SFC were estimated by offline processing of the average cutting forces. More recently, Nuori et al. [87] implemented a similar approach in constant intervals along the toolpath to monitor the variation of the SCF during the milling operation. This online scheme to monitor SFC led to the

successful monitoring of tool wear during the process. These studies verify that SCF are strongly affected by tool wear. As a result, in addition to their application in mechanistic force models, SFC can be used for tool condition monitoring as well.

Milling forces can be monitored directly during the milling process (e.g. using force dynamometers), but indirect observation methods need to be developed to monitor SFC online. In this work, three model-based methods [88] for monitoring SFC are proposed. In the first method, SFC are treated as the constant parameters of a deterministic linear force model, and Recursive Least Squares (RLS) algorithm is used to estimate them from measured forces. In the second method, SFC are modelled as constant stochastic processes, and a Kalman Filter (KF) state-observer is designed to estimate them from measured forces. This method involves a two-stage identification procedure, but the dynamics of SFC variation is described by a linear state space-model which can be observed by standard Kalman Filters. The third proposed method is similar to the second method (based on KF observers), but the identification is performed in a single step. This advantage is gained at the expense of using nonlinear state-space models, and SFC are observed using an Extended Kalman Filter (EKF). The implementation of the proposed methods is explained by providing experimental and numerical case studies. The presented experiments verify that the proposed methods can be used to estimate the SFC online and subsequently use them for tool condition monitoring. Another application of the proposed SFC observation methods is in-situ calibration of Virtual Machining Systems, which is essential for using those systems as the digital twin of the process [84].

The linear mechanistic milling force model is explained in the next section, followed by presenting three online methods to identify the parameters of the model in Section 3.3. A set of numerical case studies are presented in Section 3.4 to study the consistency and convergence of the presented identification methods. In Section 3.5, the implementation of the proposed methods is demonstrated by presenting an experimental study.

3.2 Mechanistic Force Model

Geometry of tool and workpiece engagement in 2-D end-milling operations, Figure 3.1(b). The diameter of the cylindrical tool is denoted D and the radial depth of cut b. The tool moves in X direction at the constant feedrate of c mm/tooth while the spindle rotates clockwise at Ω rad/sec. The N flutes of the endmill are indexed

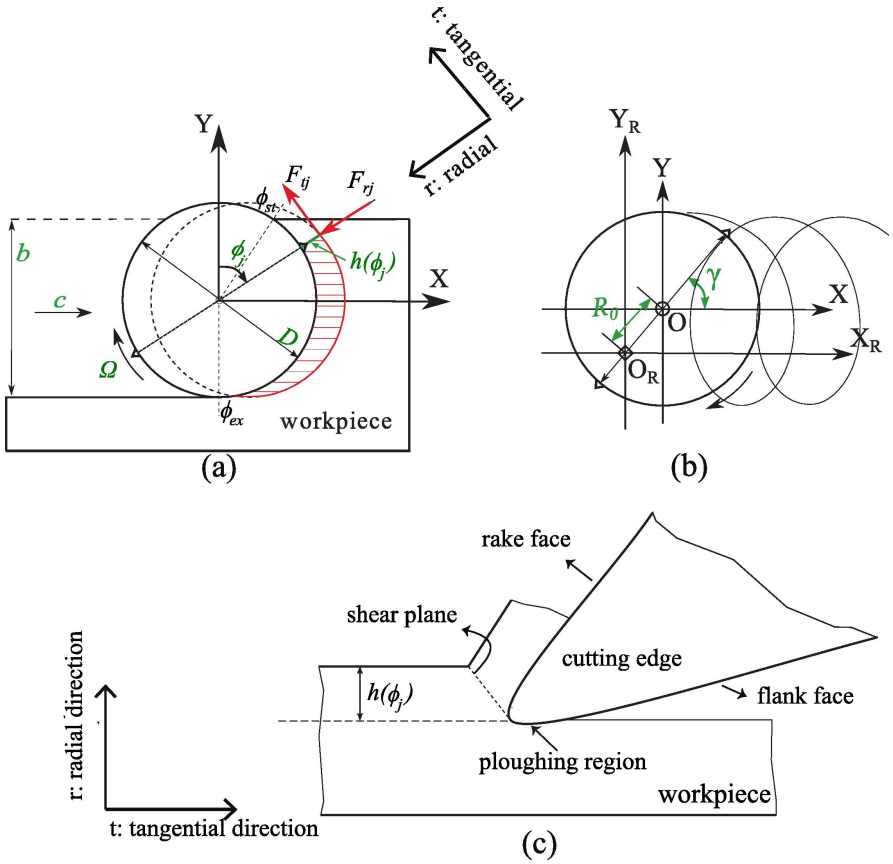

Figure 3.1: (a) Geometry of milling process; (b) Tool radial runout parameters and trochoidal trajectory; (c) Interaction of the cutting tool and workpiece material on the rake and flank faces of the cutting edge

$j = 1..N$, and the instantaneous immersion angle of the j^{th} tool measured from the normal to feed axis, Y, is denoted ϕ_j, as shown in Figure 3.1(a). The instantaneous immersion angle of each tooth is determined by the spindle rotation speed and the angular immersion of the first tooth at $t = 0$, which is denoted ϕ_0:

$$\phi_j = \Omega t - \frac{2\pi(j-1)}{N} + \phi_0; \quad j = 1, ..., N \tag{3.1}$$

The initial immersion angle, ϕ_0, is usually unknown and its estimation based on the measured forces will be discussed in Section 4.4. The overall machining forces applied on each tooth is decomposed into the radial component, F_{rj}, and tangential component, F_{tj}, as shown in Figure 3.1(a). In linear mechanistic models of machining forces, each of these components are assumed to be linear functions of the instantaneous chip

thickness [80]:

$$\begin{aligned} F_{tj} &= K_{tc}.h(\phi_j).a + K_{te}.a \\ F_{rj} &= K_{rc}.h(\phi_j).a + K_{re}.a \end{aligned} \tag{3.2}$$

where a is the axial depth of cut and $h(\phi_j)$ is uncut chip thickness. The highlighted area in Figure 3.1(a) shows the variation of chip thickness when the eccentricity of the tool rotation centre (O_R) and its geometric centre (O), i.e. radial runout, is negligible and feed speed is much lower than cutting speed. Th chip thickness in this situation is determined based on feed per tooth and instantaneous immersion angle, as follows:

$$h\left(\phi_j\right) = c \sin \phi_j \tag{3.3}$$

In practice, as shown in Figure 3.1(b), tool runout and the actual trochoidal trajectory of the cutting tooth alter the chip thickness, and neglecting their effect can cause bias error in modelling. To avoid this error, the following chip thickness model, presented in [89, 90], which considers the trochoidal trajectory and radial runout is used:

$$h\left(\phi_j\right) = q_1 . \sin \phi_j + q_2 . \sin \phi_j \cos \phi_j + q_3 . \cos^2 \phi_j + q_4 \tag{3.4}$$

where $q_i, i = 1..4$ are constants depending on feedrate per tooth, c [mm/tooth], and radial (R_0) and angular (γ) offset of tool rotation centre, O_R, from its geometric centre, O, as shown in Figure 3.1(b):

$$\begin{aligned} q_1 &= c(1 + (-1)^j \tfrac{4R_0}{\pi D} \sin \gamma); \qquad q_2 = \tfrac{-2}{\pi D} c^2 \\ q_3 &= \tfrac{1}{D} c^2; \qquad q_4 = -2(-1)^j R_0 \cos \gamma \end{aligned} \tag{3.5}$$

The constant coefficients of the linear mechanistic model in Equation (3.2), K_{tc}, K_{rc},K_{te}, and K_{re}, will be referred to as the Specific Force Coefficients (SFC). The cutting force coefficients, (K_{tc} and K_{rc}), are associated with the shearing action on the shear plane and friction forces on the rake face of the cutting edge. The edge force coefficient, K_{te} and K_{re}, are related to the ploughing action under the flank (clearance) face of the cutting edge [80]. The estimation of these coefficients from the forces measured during milling operations is the principal subject of this chapter.

The overall machining forces in feed direction, F_X, and normal direction, F_Y, are obtained by projecting the radial and tangential forces in the feed and normal directions and then summing the contributions from each of the flutes that are engaged in

the cut, as follows:

$$\{F(t)\} = \begin{Bmatrix} F_X \\ F_Y \end{Bmatrix} = \sum_{j=1}^{N} g(\phi_j) \left[T_t^X\right] \begin{Bmatrix} F_{tj} \\ F_{rj} \end{Bmatrix}$$
$$\left[T_t^X\right] = \begin{bmatrix} -\cos(\phi_j) & -\sin(\phi_j) \\ \sin(\phi_j) & -\cos(\phi_j) \end{bmatrix} \tag{3.6}$$

where $\left[T_t^X\right]$ is the rotation matrix that maps the forces from tangential and radial directions to the feed and normal directions. The engagement of each flute with the cut is determined by the Heaviside function, $g(\phi_j)$, which is nonzero only if the corresponding immersion angle is between the start and exit angles, ϕ_{st} and ϕ_{ex}, shown in Figure 3.1:

$$g(\phi_j) = H(\phi_j - \phi_{st}) - H(\phi_j - \phi_{ex}); \quad j = 1..N \tag{3.7}$$

where $H(\phi_j)$ is unit step function. The start and exit angles are determined by the radial depth of cut b, tool diameter, D, and the milling mode:

$$\begin{cases} \phi_{st} = 0 \quad \text{and} \quad \phi_{ex} = \cos^{-1}\left(1 - \frac{2b}{D}\right) & \text{upmilling} \\ \phi_{st} = \pi - \cos^{-1}\left(1 - \frac{2b}{D}\right) \quad \text{and} \quad \phi_{ex} = \pi & \text{downmilling} \end{cases} \tag{3.8}$$

3.3 Identification of Specific Force Coefficients (SFC)

In this section, the average force method [80], which is commonly used to identify SFC, is discussed first. Then, three new methods to identify SFC are introduced. These methods include Recursive Least Squares (RLS), Kalman Filter (KF), and Extended Kalman Filter (EKF) methods.

3.3.1 Average-force method

The milling forces resulting from Equation (3.6) are periodic at tooth passing period, $2\pi/N\Omega$. Average values of the periodic forces (i.e. the first term in their Fourier

expansion) are obtained by integrating Equation (3.6) over one principal period:

$$\{F_0\} = \begin{Bmatrix} F_{X0} \\ F_{Y0} \end{Bmatrix} = \frac{N\Omega}{2\pi} \sum_{j=1}^{N} \int_0^{2\pi/N\Omega} g(\phi_j) \left[T_t^X\right] \begin{Bmatrix} F_{tj} \\ F_{rj} \end{Bmatrix} dt \tag{3.9}$$

Tool runout does not contribute to the average values of the forces and therefore it can be neglected in Equation (3.9). Additionally, assuming that the feed speed is much slower than cutting speed, the trochoidal tool trajectory can be approximated by a circular motion at each tooth passing period. As a result, the simplified model in Equation (3.3) can be used to describe chip thickness variation. Substituting this chip model in Equation (3.2), and subsequently substituting the resulting tangential and radial forces in Equation (3.9) leads to the following equation of the average feed and normal forces, F_{X0} and F_{Y0}, respectively:

$$\begin{aligned}
&F_{X0} = a_{x1}c + a_{x0};\\
&F_{Y0} = a_{y1}c + a_{y0};\\
&a_{x1} = \left\{\tfrac{Na}{8\pi}\left[K_{tc}\cos 2\phi - K_{rc}\left(2\phi - \sin 2\phi\right)\right]\right\}_{\phi_{st}}^{\phi_{ex}};\\
&a_{x0} = \left\{\tfrac{Na}{2\pi}\left[-K_{te}\sin\phi + K_{re}\cos\phi\right]\right\}_{\phi_{st}}^{\phi_{ex}};\\
&a_{y1} = \left\{\tfrac{Na}{8\pi}\left[K_{tc}\left(2\phi - \sin 2\phi\right) + K_{rc}\cos 2\phi\right]\right\}_{\phi_{st}}^{\phi_{ex}};\\
&a_{y0} = \left\{-\tfrac{Na}{2\pi}\left[K_{te}\cos\phi + K_{re}\sin\phi\right]\right\}_{\phi_{st}}^{\phi_{ex}};
\end{aligned} \tag{3.10}$$

According to Equation (3.10), the average feed and normal forces are linear functions of feedrate, c, and the slopes (a_{x1} and a_{y1}) and intercepts (a_{x0} and a_{y0}) of the linear functions are directly related to SFC. Suppose the average forces, $\left\{\tilde{F}_0(c_i)\right\} = [\tilde{F}_{X0}(c_i), \tilde{F}_{Y0}(c_i)]^T$, are measured at $c_i, i = 1..N_c$ different feedrates. Note that $\tilde{.}$ is used to denote measured quantities in this paper. According to Equation (3.10), the average forces are linear functions of feedrate, therefore the average of the measured forces can be described using the following matrix equation:

$$\left\{\tilde{F}_0(c_i)\right\} = \left[b\left(c_i\right)\right]\left\{a\right\}; i = 1..N_c \tag{3.11}$$

where

$$\left[b\left(c_i\right)\right] = \begin{bmatrix} c_i & 1 & 0 & 0 \\ 0 & 0 & c_i & 1 \end{bmatrix} \quad \text{and} \quad \left\{a\right\} = \begin{bmatrix} a_{x1} & a_{x0} & a_{y1} & a_{y0} \end{bmatrix}^T \tag{3.12}$$

The constant coefficients, a_{x1} and a_{y1} are the slopes of the linear equations and a_{x0} and a_{y0} are the corresponding intercepts. These constants are estimated by the following Least Squares Estimation (LSE):

$$\begin{aligned} \{\hat{a}\} &= [B]^{\dagger}\left[\begin{array}{cccc} \left[\tilde{F}_0(c_1)\right]^T & \left[\tilde{F}_0(c_2)\right]^T & \cdots & \left[\tilde{F}_0(c_{N_c})\right]^T \end{array} \right]^T; \\ [B] &= \left[\begin{array}{ccc} [b(c_1)]^T & \cdots & [b(c_{N_c})]^T \end{array} \right]^T; \\ [B]^{\dagger} &= \left([B]^T [B] \right)^{-1} [B]^T \end{aligned} \tag{3.13}$$

where the T superscript stands for the transpose of a matrix and $\{\hat{a}\}$ is the least squares estimation of $\{a\}$. The four SFC are obtained by solving the four linear equations relating them to the components of $\{\hat{a}\}$, as shown in Equation (3.13).

3.3.2 Recursive least squares (RLS) method

In this method, instantaneous feed and normal forces are used in Recursive Least Squares (RLS) algorithm to estimate the SFC. Because instantaneous forces are used– and not their time-averages– neglecting the effect of tool run out and its trochoidal trajectory will cause a considerable bias error in estimation. To avoid this error, the complete chip thickness model described in Equation (3.4) is substituted in the equation of overall feed and normal forces in Equation (3.6), and the resulting equation is rearranged to the following form to express the instantaneous forces as linear functions of SFC:

$$\{F(t)\} = [A(t, \varphi_0)] \{K\} \tag{3.14}$$

where $\{K\} = \left[\begin{array}{cccc} K_{tc} & K_{rc} & K_{te} & K_{re} \end{array} \right]^T$, and $[A(t, \varphi_0)]$ is a 2×4 matrix depending on time and the initial immersion angle of the first flute, ϕ_0:

$$[A(\phi_0, t)] = \left[\begin{array}{cccc} A_{11} & A_{12} & A_{13} & A_{14} \\ A_{21} & A_{22} & A_{23} & A_{24} \end{array} \right]; \tag{3.15}$$

where the elements of matrix $[A(t, \varphi_0)]$ are represented as follows:

$$
\begin{aligned}
A_{11} = A_{22} &= -a \sum_{j=1}^{N} g\left(\phi_j\right) \left(q_1 \sin\phi_j \cos\phi_j + q_2 \sin\phi_j \cos^2\phi_j + q_3 \cos^3\phi_j + q_4 \cos\phi_j\right) \\
A_{12} = -A_{21} &= -a \sum_{j=1}^{N} g\left(\phi_j\right) \left(q_1 \sin^2\phi_j + q_2 \sin^2\phi_j \cos\phi_j + q_3 \cos^2\phi_j \sin\phi_j + q_4 \sin\phi_j\right) \\
A_{13} = A_{24} &= -a \sum_{j=1}^{N} g\left(\phi_j\right) \cos\phi_j \\
A_{14} = -A_{23} &= -a \sum_{j=1}^{N} g\left(\phi_j\right) \sin\phi_j
\end{aligned}
\tag{3.16}
$$

Because cutting forces are usually measured at discrete time instants, Equation (3.14) is more useful when expressed in discrete-time domain with constant sampling time of Δt:

$$\{F_k\} = [A_k(\varphi_0)]\{K\} \tag{3.17}$$

where $\{F_k\} = \{F(k\Delta t)\}$ and $[A_k(\varphi_0)] = [A(k\Delta t, \varphi_0)]$. In the presented RLS algorithm, a two-step solution is used to estimate the vector of SFC, $\{K\}$, from measured forces, $\left\{\tilde{F}_k\right\}$.

The goal in *Step 1* is to determine the unknown initial immersion angle, ϕ_0. For this, Equation (3.17) is repeated at all of the time steps within the first few tool revolutions to construct an over-determined system of linear equations.

$$\left\{\tilde{F}\right\} = [A(\phi_0)]\{K\}; \qquad \left\{\tilde{F}\right\} = \begin{Bmatrix} \left\{\tilde{F}_1\right\} \\ \vdots \\ \left\{\tilde{F}_N\right\} \end{Bmatrix}; \qquad [A(\phi_0)] = \begin{bmatrix} [A_1(\phi_0)] \\ \vdots \\ [A_N(\phi_0)] \end{bmatrix} \tag{3.18}$$

In this work, the time steps within the first six tool revolutions were used to construct such system of equations. Subsequently, the least squares estimation of $\{K\}$ is obtained from the constructed system of equations, however, the approximated coefficients and the corresponding residue (LSE error) depends on ϕ_0:

$$\epsilon(\phi_0) = \left\| [A(\phi_0)] [A_1(\phi_0)]^{\dagger} \left\{\tilde{F}\right\} - \left\{\tilde{F}\right\} \right\| \tag{3.19}$$

where $\epsilon(\phi_0)$ is the LSE error (i.e. residue) when the initial immersion is assumed ϕ_0. Any value of $0 \leq \phi_0 < 2\pi$ that leads to the smallest LSE error is chosen as the optimum ϕ_0, which is then used in the second step of the RLS estimation algorithm.

In practice, this step has to be repeated automatically every time the spindle rotation (re)starts. The computation time to complete this step depends on the number of samples used (i.e. N in Equation (3.18)) and the number of ϕ_0 values at which the LSE error is obtained. In this work, the error was obtained for 1800 different values of equally spaced between 0 and π (i.e. 0.1°increments). The computation time varies based on the processing speed of the computer and the algorithms used to determine the LSE, but it is typically below one second, which is not considerable when the algorithm is used to monitor long operations.

In *step 2*, the RLS algorithm is used to recursively update the estimation of SFC based on the forces measured at each time step. A Multi-Output RLS algorithm with forgetting factor is applied to determine the unknown $\{K\}$ from the linear equations in Equation (3.17). The estimation of SFC at each time step is updated based on its estimation in the preceding time step as follows:

$$\left\{\hat{K}_k\right\} = \left\{\hat{K}_{(k-1)}\right\} + [P_k]\,[A_k]^T[\lambda]\{e_k\} \tag{3.20}$$

where $\left\{\hat{K}_k\right\}$ stands for the estimation of SFC at the k^{th} time step, $[P_k]$ is the covariance matrix of estimation error, $[\lambda]$ is forgetting factor, and e_k is objective error function which is minimized at every updating step:

$$\{e_k\} = \left\{\tilde{F}_k\right\} - [A_k]\left\{\hat{K}_{k-1}\right\} \tag{3.21}$$

Note that the $\tilde{.}$ symbol is used to distinguish the measured forces, $\left\{\tilde{F}_k\right\}$, from their counterpart in the force model, $\{F_k\}$. At each time step, the covariance matrix of estimation error, $[P_k]$, is also updated recursively using the following equation:

$$[P_k] = [P_{k-1}] + [P_{k-1}]\,[A_k]^T\left[[\lambda]^{-1} + [A_k]\,[P_{k-1}]\,[A_k]^T\right]^{-1}[A_k]\,[P_{k-1}] \tag{3.22}$$

In this work, forgetting factor and the initial values of the estimation and the corresponding error covariance are set to $\left\{\hat{K}_0\right\} = \begin{bmatrix} 0 & 0 & 0 & 0 \end{bmatrix}^T$, $[\lambda] = 0.98[I]_{2\times2}$, and $[P_0] = 10^5[I]_{4\times4}$.

Implementation of the described RLS algorithm is demonstrated using the numerical and experimental studies in Sections 3.4(Numerical results) and 3.5(Experimental results).

3.3.3 Kalman filter (KF) method

Considering the high sampling rate that is usually used to measure cutting forces, at each time step, SFC can be assumed constant stochastic processes. In addition, because the contribution of tool runout to the overall machining forces is harmonic at the tool-passing frequency, the variation of milling forces due to runout effect can be modelled as harmonic processes at the tool-passing frequency with stochastic amplitudes. The dynamics of the variation of SFC and runout forces can therefore be described using the following discrete-time domain state space model:

$$\begin{aligned} \{q_{k+1}\} &= [\Psi_k]\{q_k\} + \{w_k\} \\ \{F_k\} &= [H_k]\{q_k\} + \{v_k\} \end{aligned} \tag{3.23}$$

where $\{q_k\}$ is the vector of state variables, $[\Psi_k]$ is state transition matrix, and $[H_k]$ is observation (or output distribution) matrix. Process noise, $\{w_k\}$, and measurement noise, $\{v_k\}$, are assumed to be uncorrelated white noise with Gaussian distribution and known covariance matrices, $[Q]$ and $[R]$, respectively. The state vector includes SFC and runout forces:

$$\{q_k\} = \begin{bmatrix} K_{tc}, & K_{rc}, & K_{te}, & K_{re}, & F_{Xr}, & \dot{F}_{Xr}, & F_{Yr}, & \dot{F}_{Yr} \end{bmatrix}^T \tag{3.24}$$

The state transition matrix defines the progression of the constant SFC, harmonic runout forces, F_{Xr} and F_{Yr}, and their time-derivatives, $\dot{F}_{Xr}$ and $\dot{F}_{Yr}$, in each time step as follows:

$$[\Psi_k] = \begin{bmatrix} [I]_{4\times4} & [0]_{4\times2} & [0]_{4\times2} \\ [0]_{2\times4} & \begin{bmatrix} \cos\Omega\Delta t & \sin\Omega\Delta t \\ -\sin\Omega\Delta t & \cos\Omega\Delta t \end{bmatrix} & [0]_{2\times2} \\ [0]_{2\times4} & [0]_{2\times2} & \begin{bmatrix} \cos\Omega\Delta t & \sin\Omega\Delta t \\ -\sin\Omega\Delta t & \cos\Omega\Delta t \end{bmatrix} \end{bmatrix}_{8\times8} \tag{3.25}$$

Output vector comprises the forces in the feed and normal direction and thus the output matrix, $[H_k]$, is defined by combining runout forces with the forces in Equation (3.6), leading to the following equation:

$$[H]_{2\times8} = \begin{bmatrix} [A_k] & \begin{matrix} 1 & 0 & 0 & 0 \\ 0 & 0 & 1 & 0 \end{matrix} \end{bmatrix} \tag{3.26}$$

Note that because runout forces are considered as additional state variables, prior knowledge of runout parameters (R_0 and λ) is no longer necessary and their values in computing the observation matrix in Equation (3.26) are set to zero.

The KF algorithm is used as a state observer to estimate the states, $\{q_k\}$, based on the observations, i.e. measured forces, $\{F_k\}$. Details of Kalman filter design can be found in various references; for example, see [91]. A brief description of the method is also provided here. The algorithm consists of initialization, prediction, and correction steps.

Step(0) - Initialization

To initialize the algorithm, the expected value of the state vector at k=0 and the associated error covariance matrix are defined:

$$\begin{aligned} \{\hat{q}_0\}^+ &= E(\{q_0\}) \\ [P_0]^+ &= E\left[\left(\{q_0\} - \{\hat{q}_0\}^+\right)\left(\{q_0\} - \{\hat{q}_0\}^+\right)^T\right] \end{aligned} \tag{3.27}$$

where $[P_k]$ is the state estimation covariance matrix, $E\{\}$ stands for the Expected value, and the superscript "+" shows a posteriori estimation. The selected initial estimate of the state vector does not affect the identified SFC, and a relatively large values are selected for $[P_0]$ to increase the convergence rate of the algorithm.

Step(1) - Prediction

The state and covariance matrix at time step k are predicted as a new priori estimation by using the system model.

$$\begin{aligned} \{\hat{q}_{k+1}\}^- &= [\Psi_k]\{\hat{q}_k\}^+ \\ [P_{k+1}]^- &= [\Psi_k][P_k][\Psi_k]^T + [Q] \end{aligned} \tag{3.28}$$

Step(2) - Correction

In this step, the error between the measured forces and the forces predicted based on the priori state estimates is multiplied by the Kalman Gain, $[G_k]$, and the result is added to the priori estimation of the state vector to update it to its posteriori estimation. The priori estimation of the correlation matrix of the states is also updated to its posteriori estimation as follows:

$$\begin{aligned} \{\hat{q}_k\}^+ &= \{\hat{q}_k\}^- + [G_k]\left(\left\{\tilde{F}_k\right\} - [H_k]\{\hat{q}_k\}^-\right) \\ [G_k] &= [P_k]^-[H_k]^T\left([H_k][P_k]^-[H_k]^T + [R]\right)^{-1} \\ [P_k]^+ &= ([I] - [G_k][H_k])[P_k]^- \end{aligned} \tag{3.29}$$

3.3.4 Extended kalman filter (EKF) method

In both RLS and KF methods, the initial immersion angle of the first flute, ϕ_0, was obtained separately using the batch LSE method in Section 3.3.2. If this parameter is treated as another unknown state variable with constant stochastic dynamics, the state space model in Equation (3.23) will no longer be linear, but it can be described using the following nonlinear state space model:

$$\begin{aligned} \{q_{k+1}\} &= [\Psi_k]\{q_k\} + \{w_k\} \\ \{F_k\} &= h(\{q_k\}, k) + \{v_k\} \end{aligned} \tag{3.30}$$

where the state vector includes the initial immersion angle as the additional variable:

$$\{q\} = \begin{bmatrix} K_{tc} & K_{rc} & K_{te} & K_{re} & F_{Xr} & \dot{F}_{Xr} & F_{Yr} & \dot{F}_{Yr} & \phi_0 \end{bmatrix}^T \tag{3.31}$$

The state transition matrix will also be extended to a 9×9 matrix with zeros in all of the additional 9^{th} row and column, and 1 on the 9^{th} diagonal element. Comparing the linear model in Equation (3.23) and the nonlinear model in Equation (3.30), the linear output matrix, $[H_k]$ is converted to the time-varying nonlinear function $h(\{q_k\}, k)$. Extended Kalman Filter (EKF) allows the estimation of state variables in non-linear systems with additive noise [91]. Assuming small sampling time Δt, the nonlinear output function ($h(\{q_k\}, k)$) can be linearized around its value at the priori estimation of the state vector in current time step, $\{\hat{q}_k\}^-$, leading to the following linearized output equation in the state space model:

$$\{F_k\} = h(\{\hat{q}_k\}^-, k) + [J_k]\left(\{q_k\} - \{\hat{q}_k\}^-\right) + \{v_k\}; \quad [J_k] = \left[\frac{\partial h}{\partial q}\right]_{q=\{\hat{q}_k\}^-} \tag{3.32}$$

Components of the Jacobian matrix,$[J_k]$, in Equation (3.32) are obtained by substituting F_X and F_Y from Equation (3.6) in the following equation:

$$[J_k] = \begin{bmatrix} \frac{\partial F_X}{\partial K_{tc}} & \frac{\partial F_X}{\partial K_{rc}} & \frac{\partial F_X}{\partial K_{te}} & \frac{\partial F_X}{\partial K_{re}} & 1 & 0 & 0 & 0 & \frac{\partial F_X}{\partial \phi_0} \\ \frac{\partial F_Y}{\partial K_{tc}} & \frac{\partial F_Y}{\partial K_{rc}} & \frac{\partial F_Y}{\partial K_{te}} & \frac{\partial F_Y}{\partial K_{re}} & 0 & 0 & 1 & 0 & \frac{\partial F_Y}{\partial \phi_0} \end{bmatrix}_{\{\hat{q}_k\}^-} \tag{3.33}$$

The three stages, initialization, prediction, and correction in Kalman filter algorithm are also used to update the estimate of the state variables from the linearized state space model in Eqs.3.30 and 3.32 as well. While the initialization and prediction stages are similar to Equation (3.27) and 3.28, the correction stage in Extended

Kalman Filter changes to the following:

$$\begin{aligned}
\{\hat{q}_k\}^+ &= \{\hat{q}_k\}^- + [G_k]\left(\left\{\tilde{F}_k\right\} - h(\{\hat{q}_k\}^-, k)\right) \\
[G_k] &= [P_k]^-[J_k]^T\Big([J_k]\,[P_k]^-[J_k]^T + [R]\Big)^{-1} \\
[P_k]^+ &= (I - [G_k]\,[J_k])\,[P_k]^-
\end{aligned} \tag{3.34}$$

3.4 Numerical Simulation

A numerical example is presented to study the consistency and convergence of RLS, KF, and EKF methods in identifying SFC. Cutting forces in feed and normal directions, F_X and F_Y, are simulated at $\Delta t = 0.2$ millisecond intervals by substituting the chip thickness model from Equation (3.4) in the mechanistic cutting force model in Equation (3.6).

For numerical simulation, the constant sampling time $\Delta t = 0.2$ milliseconds in the discrete-time domain is determined based on the tool passing frequency and Nyquist sampling theorem. The Nyquist sampling theorem provides a prescription for the nominal sampling interval required to avoid aliasing. It may be stated simply as follows: The sampling frequency should be at least twice the highest frequency contained in the signal. In mathematical terms $f_s \geq 2f_c$ where f_s is the sampling frequency, and f_c is the highest frequency contained in the signal. Considering the spindle speed of 2000 rpm and a two-flute cutting tool, the tool passing frequency $f_c = 66.7Hz$. Therefore, the sampling frequency should be at least $f_s = 133.4Hz$. In the machining applications, the ideal sampling frequency is usually determined 10 times higher than the Nyquist frequency. To stay on the safe side, the sampling frequency is chosen at 5 KHz, which is more than 30 times higher than the Nyquist frequency. This assumption results in the sampling time $\Delta t = 0.2$ milliseconds.

Feedrate $c = 0.2$ mm/tooth, spindle speed of $\Omega = 2000$ rev/min, a two-fluted cutter, and full immersion milling ($\phi_{st} = 0$ and $\phi_{ex} = \pi$) with $a = 1$ mm axial depth of cut is assumed in simulations. The true SFC are assumed to be $K_{tc} = 750$ MPa, $K_{rc} = 150$ MPa, $K_{te} = 20$ N/mm, $K_{re} = 30$ N/mm. Two sets of simulations were performed. In the first set, the tool runout and measurement noise are assumed to be zero; in the second set, the radial and angular offset parameters of runout are assumed R_0=10 μm and γ=0^o, and measurement noise is added to the simulated forces. Signal to noise ratio (SNR) in the second set is 15 dB and 18 dB for the force signals $F_X$and F_Y, respectively. The cutting forces from the two sets of simulations

are shown in Figure 3.2 (a) and (b). The initial immersion angle in both simulations are assumed $\phi_0 = 30^o$.

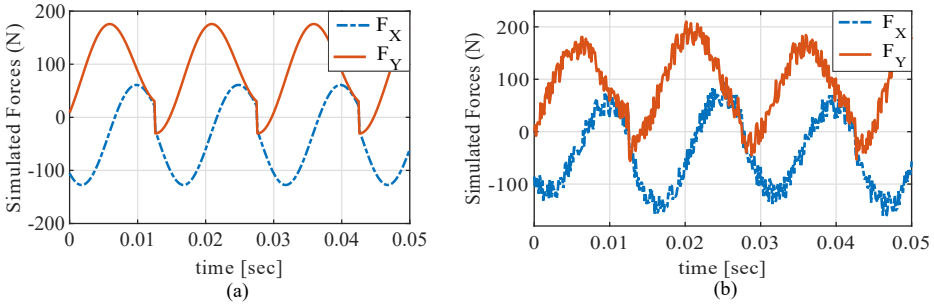

Figure 3.2: Simulated forces in (a)first set: no runout and noise, (b) second set: considering $R_0 = 10\mu$m tool runout at $\gamma = 0$, measurement noise of 15 dB SNR in F_X, and 18 dB in F_Y . Cutting conditions: $K_{tc} = 750$ MPa, $K_{rc} = 150$ MPa, $K_{te} = 20$ N/mm, $K_{re} = 30$ N/mm, $c = 0.2$ mm/tooth, $\Omega = 2000$ rev/min, axial depth of cut $a = 1$ mm, $\Delta t = 0.2$ milliseconds, and Full Immersion engagement.

In order to estimate the initial immersion angle in the first stage of RLS method, a batch LSE is applied on the simulated forces, shown in Figure 3.2. The LSE error when various ϕ_0 values are used in the batch LSE is shown in Figure 3.3. In the first set of simulations, Figure 3.3(a), the LSE error becomes minimum at $\phi_0 = 30^o$, and in the second set, Figure 3.3(b), it becomes minimum at $\phi_0 = 28.9^o$. These values are used as the optimum estimation of ϕ_0 in the proposed RLS and KF methods.

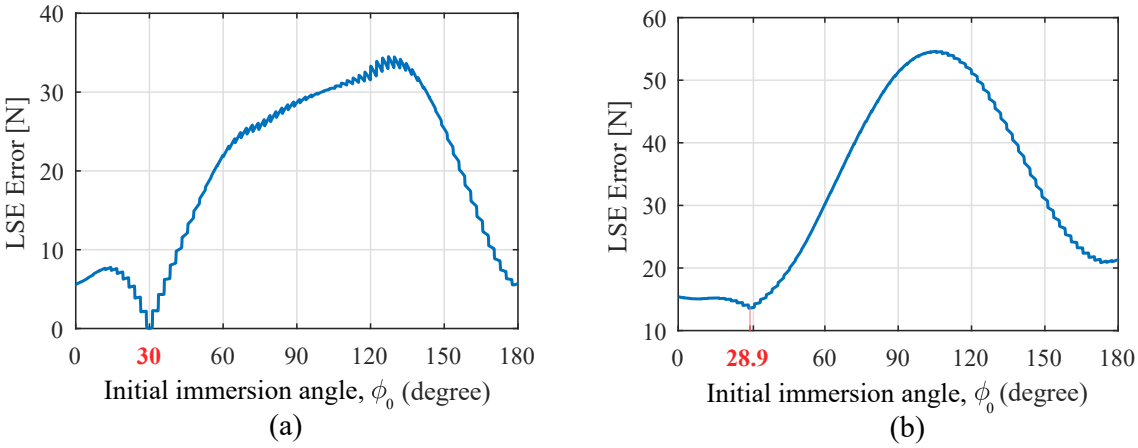

Figure 3.3: Identification of unknown initial immersion angle, ϕ_0, based on the estimation error (residue) of batch Least Square Estimation. (a)first set: no runout and noise, (b)second set: considering the effect of noise and tool runout.

Figure 3.4(a-d) shows the convergence of SFC when the cutting forces resulting

from the first set of simulations (i.e. no runout and noise) are used in the RLS, KF, and EKF algorithms. The initialization parameters applied in each of the three methods, RLS, KF, and EKF, are presented in Table 3.1.

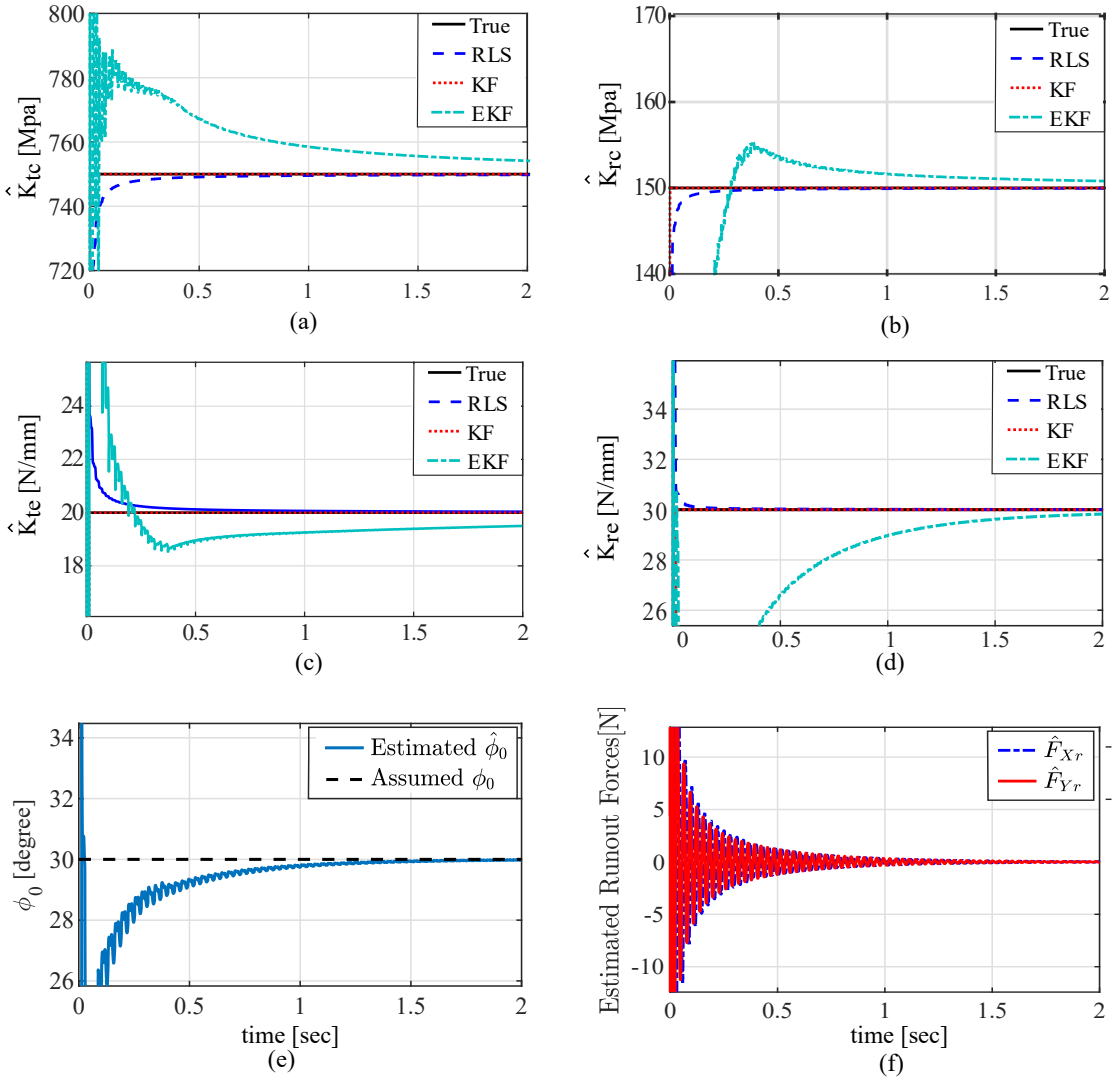

Figure 3.4: Numerical simulation results without considering runout and measurement noise. (a-d) Convergence of SFC estimated by RLS, KF, and EKF; (e) Initial immersion angle estimated by EKF. (f) runout forces estimated by EKF during the milling process. Forces simulated using $K_{tc} = 750$ MPa, $K_{rc} = 150$ MPa, $K_{te} = 20$ N/mm, $K_{re} = 30$ N/mm, $c = 0.2$ mm/tooth, $\Omega = 2000$ rev/min, axial depth of cut $a = 1$ mm, $\Delta t = 0.2$ milliseconds, and Full Immersion engagement.

Figure 3.4 shows the convergence of force model parameters when noise and runout is not included in simulations (first set of simulations). Therefore, RLS and KF algorithms converge asymptotically to the true values used in simulations. The EKF

Table 3.1: The initialization parameters applied for RLS, KF, EKF algorithms. $[R], [Q]$, and $[P_0]$ are diagonal matrices, and $Q_{(i,i)}$ and $P_{0(i,i)}$ denote the i^{th} diagonal elements of $[Q]$ and $[P_0]$ matrices, respectively.

RLS	KF	EKF
$[\lambda] = 0.98[I]_{2\times2}$	$[R] = 2 \times 10^{-2}[I]_{2\times2}$	$[R] = 2 \times 10^{-2}[I]_{2\times2}$
$[P_0] = 10^2[I]_{4\times4}$	$[Q] = 10^{-8}[I]_{8\times8}$	$Q_{(i,i)} = \begin{cases} 10^{-8};\ i = 1, ..., 8 \\ 10^{-10};\ i = 9 \end{cases}$
$\{\hat{K}_0\} = \{0\}_{4\times1}$	$[P_0]^+ = 10^7[I]_{8\times8}$	$P_{0(i,i)} = \begin{cases} 10^7;\ i = 1, ..., 8 \\ 10^3;\ i = 9 \end{cases}$
	$\{q_0\}^+ = \{0\}_{8\times1}$	$\{q_0\}^+ = \{0\}_{9\times1}$

algorithm, due to linearization errors, converges to a biased estimation, but the estimation bias is negligible ($\sim 1\%$). In the KF algorithm, in addition to SFC, the runout forces also converge to the true value (zero runout). In the EKF, the initial immersion angle ϕ_0 is considered as an additional state variable, which converges to its true value, 30^o, as shown in Figure 3.4(e).

Figure 3.5 shows the convergence of the RLS, KF, and EKF algorithms when forces simulated in the second set (with noise and runout) are used. RLS and KF converge to the true values with a negligible bias error. This error is more clear in $\hat{K}_{rc}$ convergence diagram shown in part (b) of the figure. The deterioration of the performance of the RLS and KF algorithms is associated with the error in estimating the initial immersion angle, ϕ_0, in the first step of estimation process discussed in 3.3.2. The estimated ϕ_0 used in RLS and KF is 28.9^o, different from true value 30^o. The KF algorithm also converges to the true values of the runout forces. Similar to Figure 3.4, in Figure 3.5, the EKF converges to a biased value of the SFC, but the offset between the true solution and the converged values is within the typical measurement errors.

3.5 Experimental Results

A set of milling experiments were conducted to study the performance of the average force method, RLS, KF, and EKF methods in identifying SFC in milling. The presented experiments were performed on a 3-axis machining centre with a 2-tooth inserted tool with 25.4mm diameter. The workpiece material was Al6061, and the milling forces in the feed and normal directions were measured using a Kistler 9257B table dynamometer. Force signals were amplified using a Kistler 5814B1 amplifier

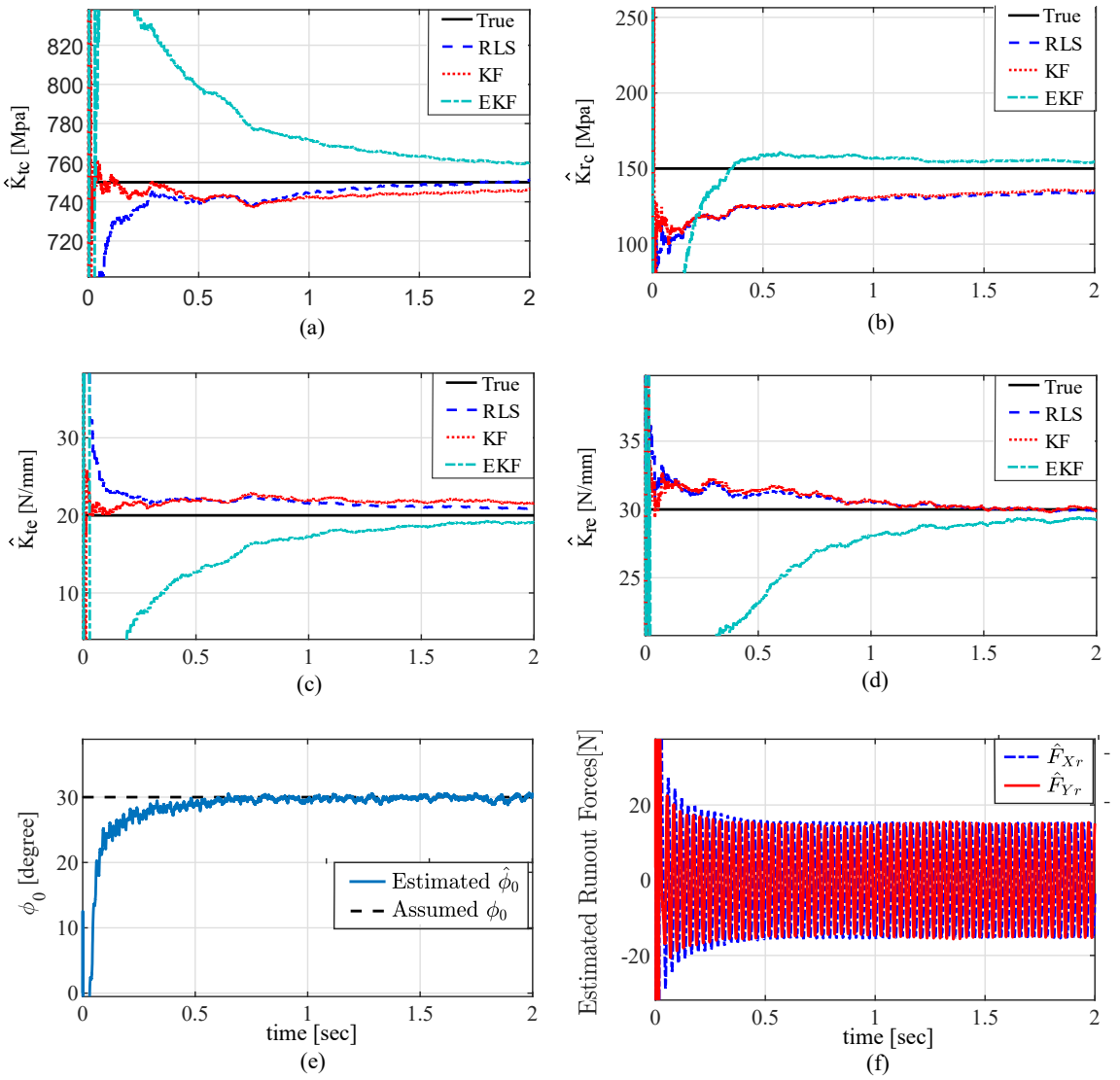

Figure 3.5: Numerical simulation results considering measurement noise and tool runout. (a-d) Convergence of SFC estimated by RLS, KF, and EKF; (e)Initial immersion angle estimated by EKF. (f)runout forces estimated by EKF during the milling process. Forces simulated using $K_{tc} = 750$ MPa, $K_{rc} = 150$ MPa, $K_{te} = 20$ N/mm, $K_{re} = 30$ N/mm, $c = 0.2$ mm/tooth, $\Omega = 2000$ rev/min, axial depth of cut $a = 1$ mm, $\Delta t = 0.2$ milliseconds, and Full Immersion engagement. Runout parameters are assumed $R_0 = 10\mu$m, $\gamma = 0^o$, and signal to noise ratio (SNR) is 15 dB and 18 dB for the force signals F_X and F_Y.

and digitized using a NI 9234 data acquisition card. Spindle speed and axial depth of cut were maintained at 2000 rev/min and 1 mm in all of the experiments. Considering one of the teeth as the reference, the eccentricity of the other tooth is measured to

represent the radial runout R_0. Runout is measured using a dial indicator pressed against the tool shank while it is turned. Total indicated runout (TIR) is a technician's term for the measured runout of any rotating system, including all forms of runout, at the measured point. This value for the tool used in the experiments was read $R_0 = 13\mu m$. The eccentricity angle γ (shown in Figure 3.1(b)) is assumed zero, because its effect is superimposed with the initial immersion angle, ϕ_0 , which is identified as explained in what follows.

3.5.1 Average-force method

Cutting forces were measured at four different feedrates, c =0.05, 0.1, 0.15, and 0.2 mm/tooth. The average of the measured forces at each feedrate are shown in Figure 3.6. These average forces and the corresponding feedrates are substituted in Equation (3.13), and the resulting constant coefficients $(a_{x1}, a_{x0}, a_{y1}, a_{y0})$ are substituted in Equation (3.12) to determine the average SFC. As shown in Figure 3.6, K_{tc} and K_{rc} are estimated 1007.8 and 430.5 MPa, and K_{te} and K_{re} are estimated 28.2 and 21.3 N/mm, respectively. Because average forces are used in this method, runout and initial immersion angle do not affect the identified coefficients.

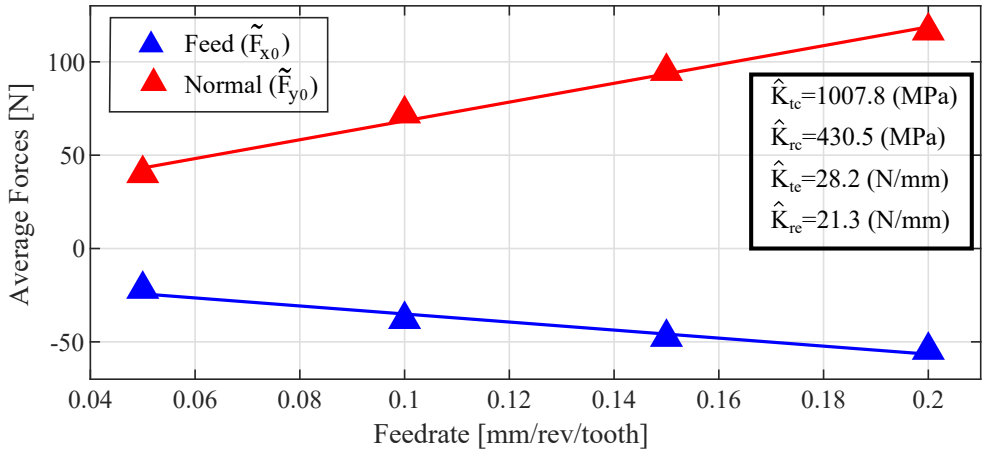

Figure 3.6: Identification of SFC using average measured forces. Cutting conditions are $c = 0.05, 0.1, 0.15, 0.2$ mm/tooth, $\Omega = 2000$ rev/min, axial depth of cut $a = 1$ mm, material Al 6061, inserted cutter with two teeth and 25.4 mm diameter, and full immersion engagement.

3.5.2 RLS method

In the first stage of RLS method, the initial immersion angle is estimated by applying batch LSE on the forces measured during the first six revolutions of the tool.

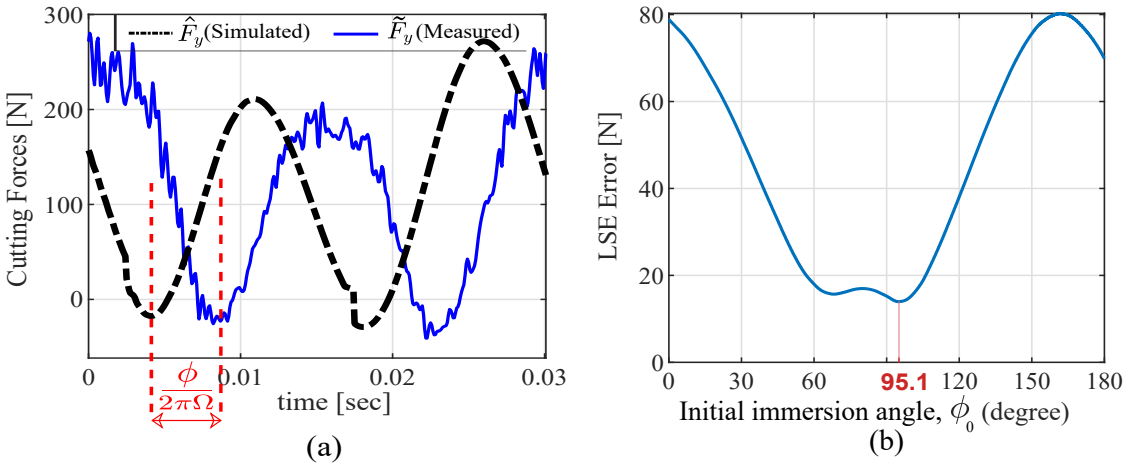

Figure 3.7: (a) Offset angle between simulation and measured forces, and (b) Variation of Least Square Estimation error by initial immersion angle ϕ_0.

Figure 3.7 shows the LSE error when various ϕ_0 values are used in the batch LSE. Part (a) of the figure shows the measured forces and the estimated ones when a certain value of ϕ_0 is used. As shown in part (b), at $\phi_0 = 95.1^o$ the LSE error becomes minimum, and therefore this value is used as the optimum estimation of ϕ_0 in the RLS and KF algorithms.

Figure 3.8(b) shows the milling forces measured during the test with feedrate $c = 0.2$ mm/tooth. For a better visibility, the forces during only a few tool revolutions are shown. These forces are used in the RLS algorithm to estimate SFC at every time step. The evolution of the estimated force model coefficients is shown in part (a) of the figure. The estimated values for $\hat{K}_{tc}$ and $\hat{K}_{rc}$ converge to 1060 and 430 MPa, respectively, and the edge force coefficients converge to $\hat{K}_{te} = 22$ and $\hat{K}_{re} = 20$ N/mm.

The differences between SFC identified using RLS and average method is mainly attributed to the fact that RLS algorithm estimates the coefficients at the operational feedrate (0.2 mm/tooth), but the average method estimates the coefficients for a range of feedrates (0.05-0.2 mm/tooth). A comparison between the measured forces and the ones estimated using RLS are shown in Figure 3.8(b).

As the RLS algorithm converges, the covariance of estimation error approaches

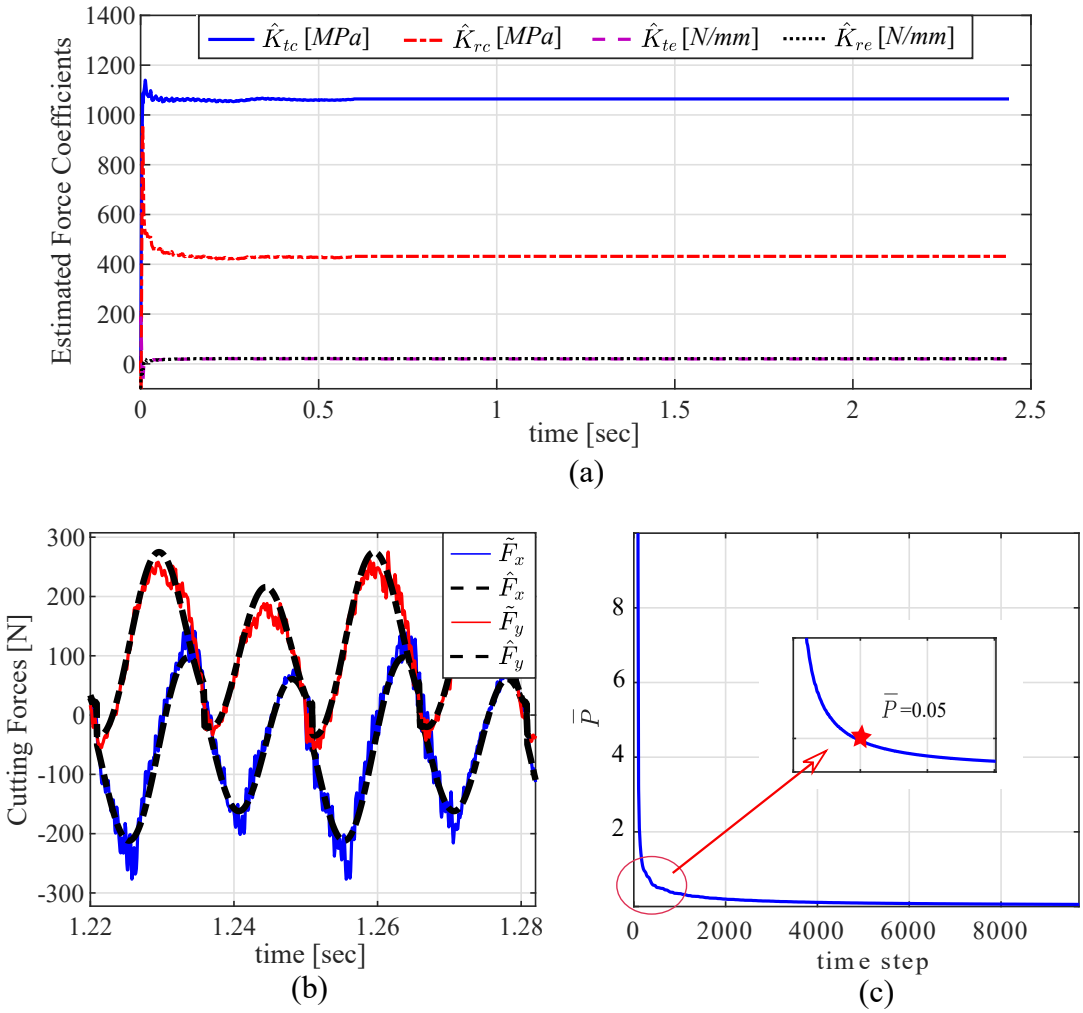

Figure 3.8: (a) RLS identification of SFC from forces measured at $c = 0.2$ mm/tooth; (b) Comparison of estimated and measured cutting forces in X and Y directions; (c) Variation of the average of the diagonal elements of error covariance matrix by time steps.

zero, which causes numerical drift of the estimated solution. In order to avoid this problem, the estimation process is stopped when the mean value of the diagonal elements of covariance matrix, $\bar{P}$ in the following equation, becomes smaller than a preset threshold value:

$$\bar{P} = \frac{1}{4} \sum_{i=1}^{4} P_{(i,i)} \tag{3.35}$$

The algorithm termination threshold significantly affects the estimated coefficients in RLS method. Figure 3.8(c) shows the convergence of $\bar{P}$ by time. In this work,

to avoid numerical drift, $\bar{P} = 0.052$, which is at the knee of the convergence curve, is selected as the termination point of RLS algorithm. If the value of $\bar{P}$ goes below this threshold, algorithm stops estimating the coefficients until $\bar{P}$ returns above this threshold.

3.5.3 KF method

The presented KF methods is implemented in this section to estimate SFC and the runout forces contributing to the measured forces. The initial immersion angle is estimated $\phi_0 = 95.1^o$ from the prior analysis discussed in Section 3.3.2.
Convergence of the KF algorithm is shown in Figure 3.9(a). The initial estimates of the state vector and covariance matrices in the performed KF algorithm are as the same as the values used in Section 3.4, shown in Table 3.1. The SFC converge to $\hat{K}_{tc} = 1013$ MPa, $\hat{K}_{rc} = 422$ MPa, $\hat{K}_{te} = 26$ N/mm, and $\hat{K}_{re} = 22$ N/mm. The forces estimated by the KF algorithm are compared against the measured ones in Figure 3.9(b).

3.5.4 EKF method

Extended Kalman Filter method was implemented to identify SFC, runout forces, and the initial immersion angle from the forces measured at $c = 0.2$ mm/tooth. Figure 3.10 shows the convergence of SFC to $\hat{K}_{tc} = 1020$ MPa, $\hat{K}_{rc} = 442$ MPa, $\hat{K}_{te} = 24$ N/mm, and $\hat{K}_{re} = 22$ N/mm. The estimated forces are also compared against the measured forces in Figure 3.10(b). The main dvantage of EKF over standard KF and RLS is its capability to estimate both initial immersion angle and SFC in one step. Figure 3.10(c) shows that the mean value of the estimated ϕ_0 in the EKF algorithm converges to approximately $\phi_0 = 95^o$.

While the measurement noise covariance, $[R]$, can be measured from the baseline (i.e. air cutting) of the measured forces, determination of the process noise covariance $[Q]$ in KF method is challenging. Figure 3.11 shows the variation of the average SFC identified using KF method when various values for Q are used as the diagonal element of the process noise matrix, $[Q]$. As shown in this figure, the assumed process noise covariance, $[Q]$, greatly affects the accuracy of estimation. Considering that all of the SFC converge to a constant value for Q smaller than 10^{-8}, this value is used as the optimum value in this case study.

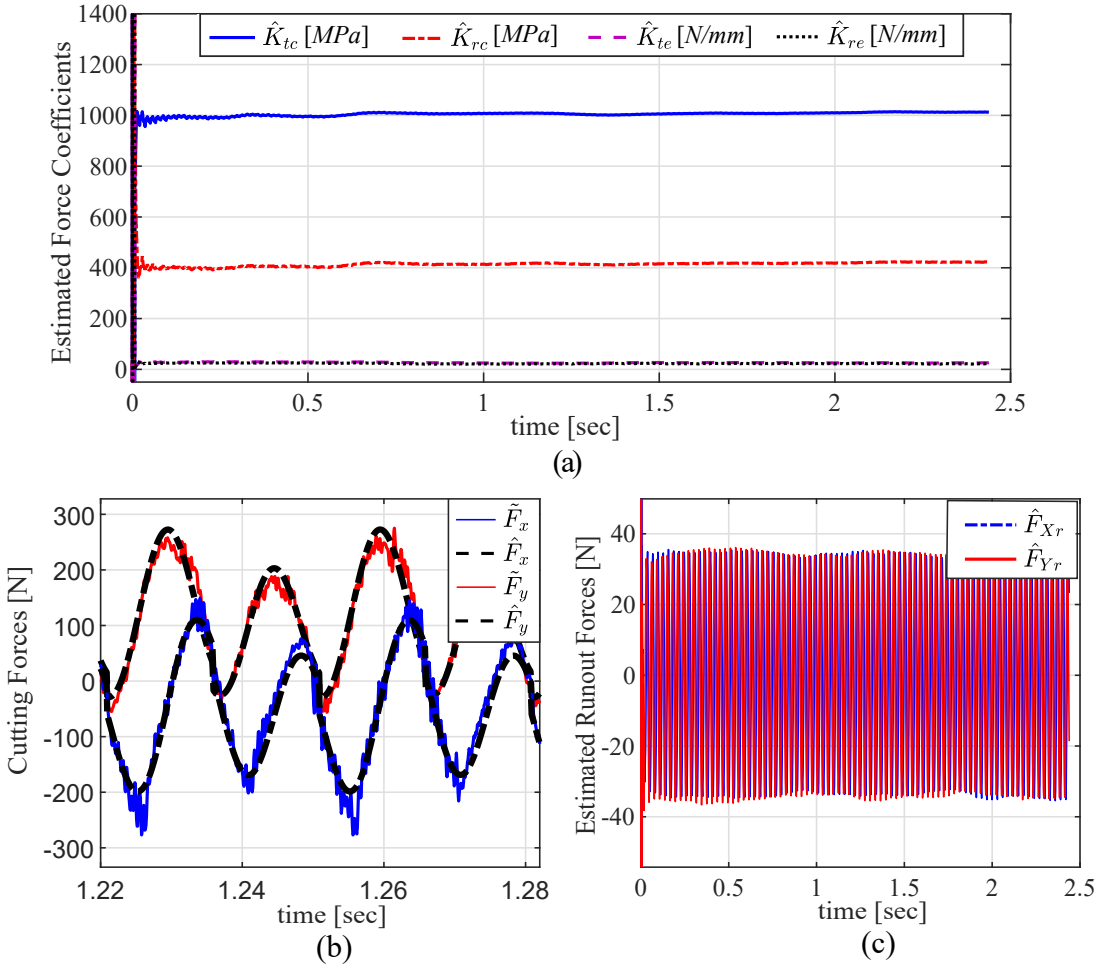

Figure 3.9: (a) Kalman Filter identification of SFC from the forces measured at $c =$ 0.2 mm/tooth; (b) Comparison of measured cutting forces and the forces estimated using Kalman Filter Method; (c) Runout forces estimated by Kalman filter

The presented methods were also used to identify the force model parameters from the forces measured at $c = 0.05, 0.1$, and 0.15 mm/rev. Figure 3.12 shows the convergence of the cutting force coefficients, $\hat{K}_{tc}$ and $\hat{K}_{rc}$, estimated using the KF algorithm. Due to chip thinning effect [92], SFC tend to increase at lower chip thickness where ploughing action is more dominant than shearing. The increasing trend of the cutting force coefficients is shown in Figure 3.12 when the feedrate reduces from 0.2 to 0.05 mm/tooth in KF method.

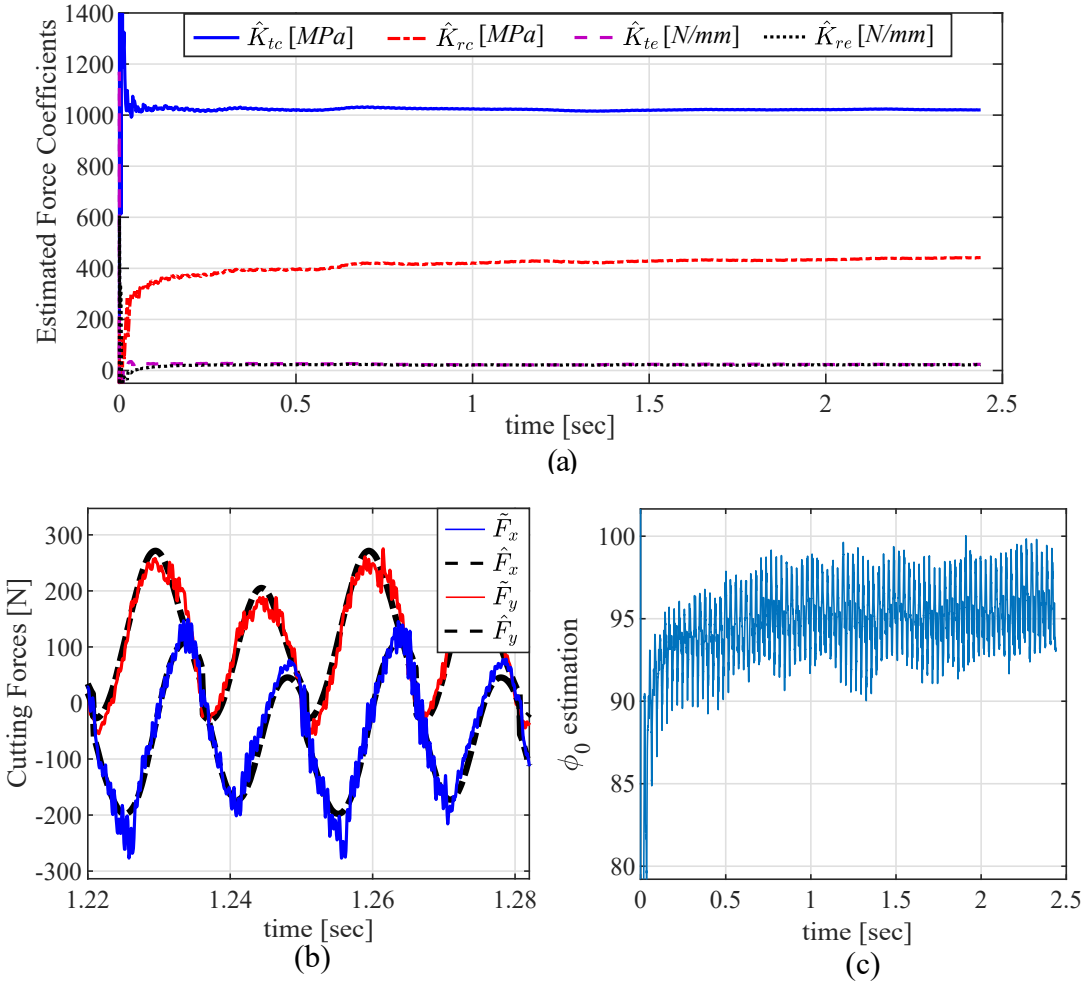

Figure 3.10: (a) EKF identification of SFC from forces measured at $c = 0.2$ mm/tooth; (b) Comparison of the measured forces and the forces estimated using EKF ; (c) Estimation of ϕ_0 using Extended Kalman Filter

3.6 Comparison

In preceding sections, all of the three presented methods were shown to be capable of identifying the SFC in full-immersion operations. To study the performance of the presented methods in partial-immersion operations ($b < D$), RLS and KF methods were used to identify the SFC from the forces measured during half-immersion downmilling ($\phi_{st} = 90$ and $\phi_{ex} = 180$).

Figure 3.13 shows the SFC identified using the RLS method as well as the estimated and measured forces. Similar to the full-immersion case, the initial immersion angle (ϕ_0) was determined in the fist stage, as shown in part (c) of Figure 3.13. The

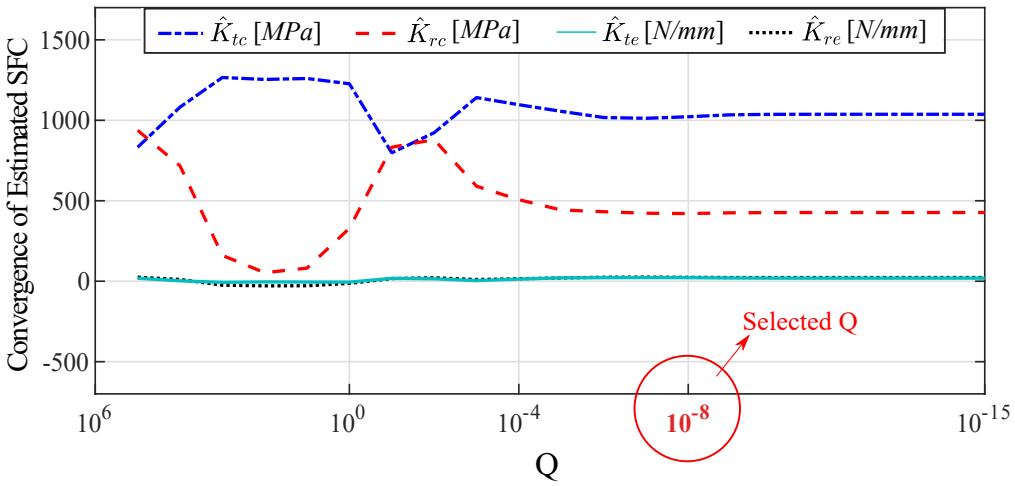

Figure 3.11: Variation of the identified SFC by Q, the diagonal element of process noise covariance matrix $[Q]$.

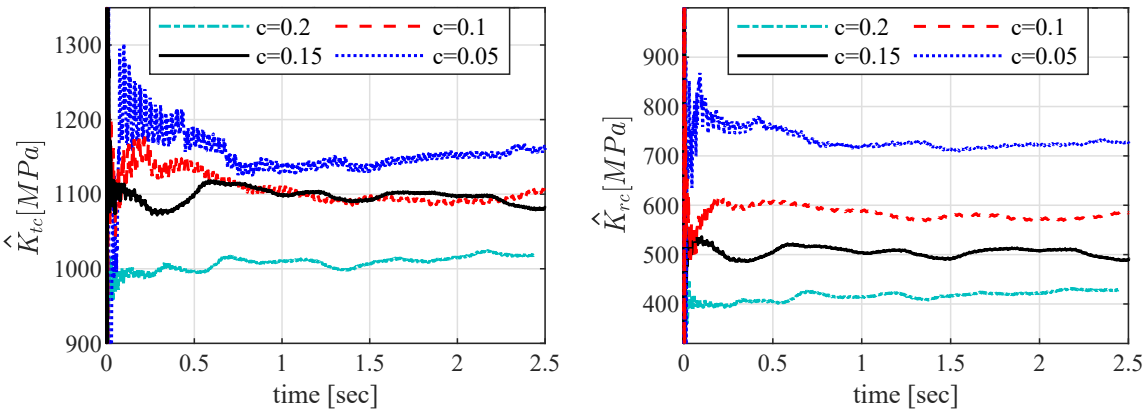

Figure 3.12: Cutting force coefficients estimated using KF algorithm from forces measured at c=0.05, 0.1, 0.15, and 0.2 mm/tooth

SFC are identified and shown in Figure 3.14 using the KF method. Also, the measured and estimated cutting forces, and the estimated runout forces in the half-immersion case are depicted in this figure. The identified SFC from both RLS and KF methods are similar but slightly different than the values obtained in the full-immersion case. The EKF cannot be used in the case of half-immersion with a 2-fluted tool because, as is shown in part (b) of Figure 3.13 and Figure 3.14, the cutting force is not differentiable (due to its sharp changes) and therefore the Jacobian matrix in EKF cannot be defined. In such cases, alternative methods such as Unscented Kalman Filter [93] could be considered.

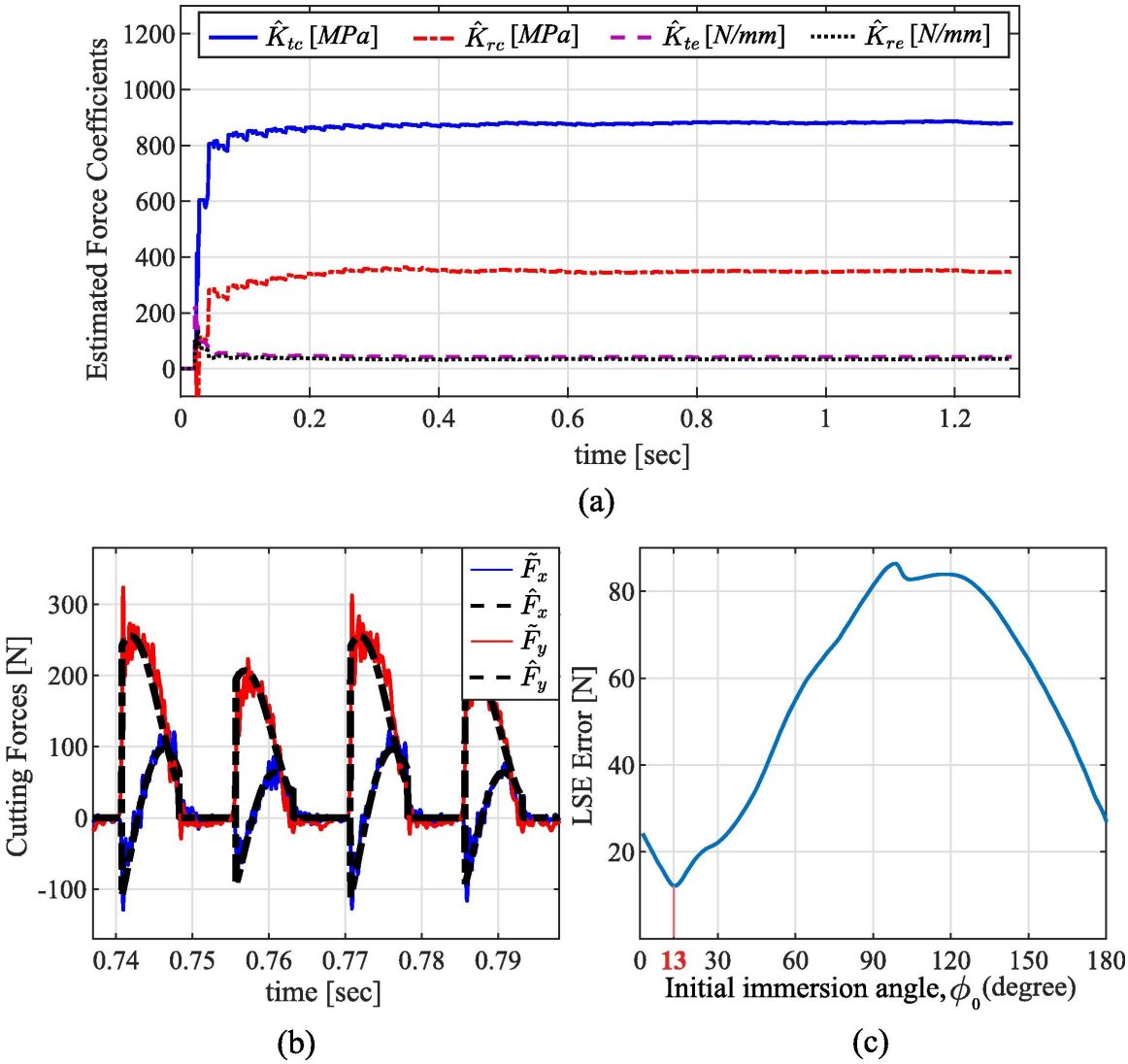

Figure 3.13: Cutting force coefficients estimated using KF algorithm from forces measured at c=0.05, 0.1, 0.15, and 0.2 mm/tooth

A qualitative comparison of the presented methods with respect to various performance criteria is presented in Table 3.2. The advantage of KF and EKF methods over RLS is in their capability to identify the SFC without a prior knowledge of the runout parameters. When an accurate measurement of the runout parameters is available, the application of RLS is more advantageous, because information about the process and measurement noise is not required. The EKF is advantageous over the other presented methods, because it does not require the determination of initial immersion angle in the first stage of identification. However, the EKF can only be applied when there is a continuous engagement between the tool and the workpiece.

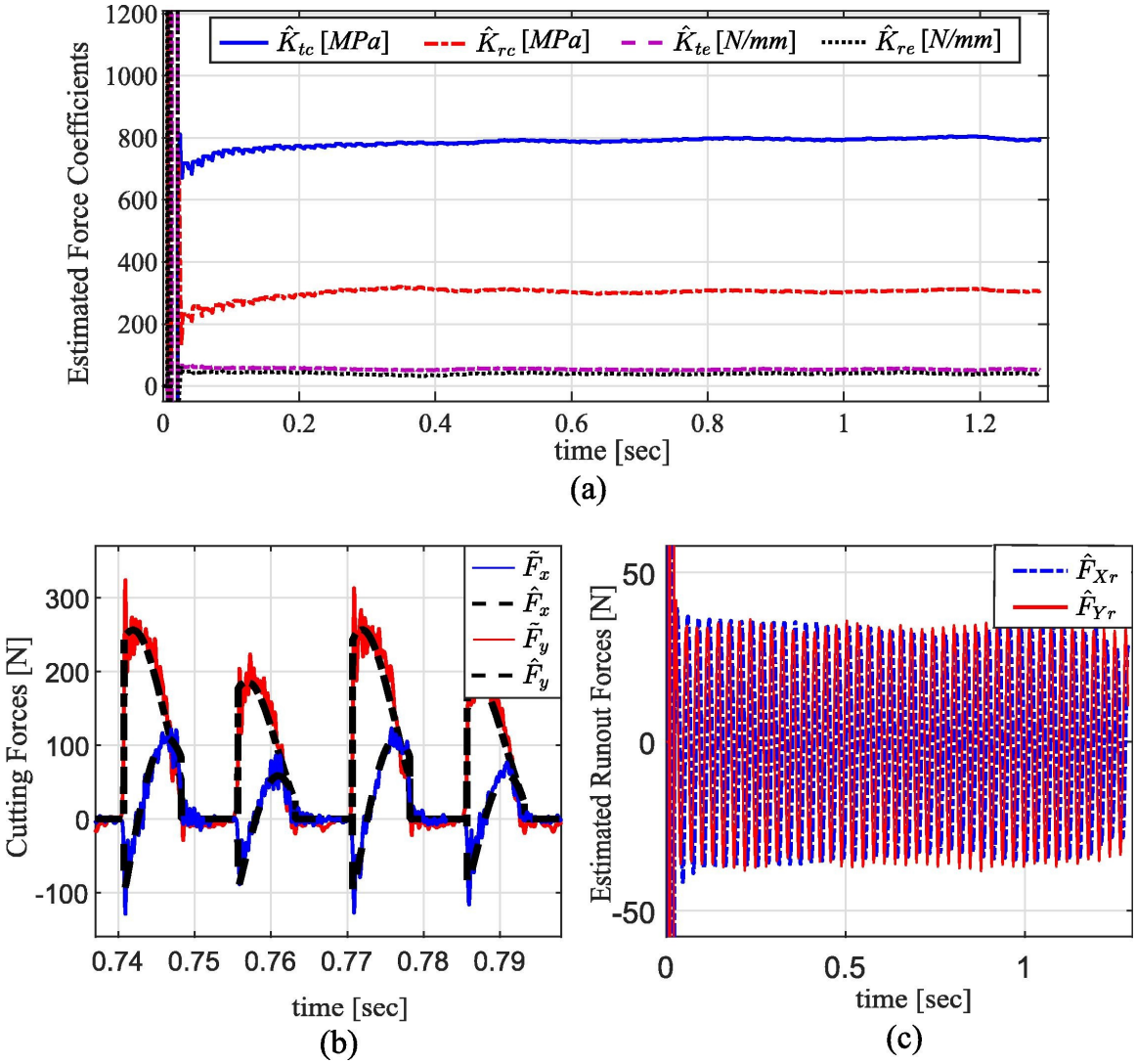

Figure 3.14: Cutting force coefficients estimated using KF algorithm from forces measured at c=0.05, 0.1, 0.15, and 0.2 mm/tooth

A quantitative comparison of the convergence rate of the three methods is not possible, because each method involves a different number of variables. Nonetheless, as shown in Figure 3.4, because EKF linearizes the nonlinear system at each time-step of the algorithm, it converges slower than KF. The RLS algorithm converges the fastest as it involves a fewer number of variables. The RMS error in estimating the measured forces in each of the methods is also reported in Table 3.2. All of the three methods lead to similar estimation errors, while the forces are predicted with a slightly lower accuracy using the traditional average method. This lower accuracy is expectable, because the SFC resulting from the average method are identified for

a range of feedrate values, whereas in the presented methods, they are adaptively calibrated for the specific feedrate that is being used in the operation.

Table 3.2: Comparison of identification methods based on the full-immersion force measurements

Method	runout	online	identification steps	convergence rate	RMS error%
Average	Measured	No	One	N/A	$F_x(5.5), F_y(7.2)$
RLS	Measured	Yes	Two	Fast	$F_x(5.3), F_y(6.9)$
KF	Estimated	Yes	Two	Slow	$F_x(5.1), F_y(6.7)$
EKF	Estimated	Yes	One	Slowest	$F_x(5.1), F_y(6.7)$

3.7 Conclusions

Three online identification methods were presented to monitor the evolution of Specific Force Coefficients (SFC) of linear milling force models. Conventional SFC calibration methods require measuring the milling forces in various cutting conditions, and then processing them using offline curve fitting algorithms. The presented Recursive Least Squares(RLS), Kalman Filter(KF), and Extended Kalman Filter (EKF) methods were shown to be capable of identifying SFC recursively at every discrete time step during the milling process.

While dynamometers are precise in measuring machining forces at low frequencies, their electromechanical dynamics distort the high-frequency content of the forces. It results in critical measurement errors, particularly in high-speed or highly intermittent milling processes [94]. Since the tool passing frequency is much lower than the natural modes of the dynamometer, it does not play a big role in the accuracy of results in this project, and therefore, the dynamics of the dynamometer were neglected in the modeling.

Because the SFC are directly linked to the mechanics of chip formation, real time implementation of the proposed methods can lead to a more effective process monitoring during milling operations. In addition, the presented methods can be used for in-situ calibration of Virtual Machining Systems when they are used as the digital twin of the machining process.

Chapter 4

Recursive Identification of Cutting Force Model Parameters in Milling of CFRPs

4.1 Introduction

CFRPs are widely used in various industries due to their low weight-to-strength ratio, corrosion resistance, and vibration absorption [95]. Because of the non-homogeneous properties of CFRP composites, unwanted damages such as delamination, chipping, and tool wear can be easily formed under excessive cutting forces during the machining operations [29, 34]. As a result, modelling machining forces has received much attention in order to prevent these damages and improve the machinability and quality of surface finish in milling CFRP [18].

Many researchers have been successfully established mechanistic force models to relate cutting forces to the tool geometry and milling parameters based on the metal cutting theories [53, 24]. Due to the anisotropic structure of the composites material, chip formation mechanics in CFRP depends on the fiber cutting angle [96], which varies periodically as the tool rotates during the milling process. This relationship was discussed by Kalla et al. in [96]. Considering this periodic variation, mechanistic force models in metallic materials have been adopted for CFRP milling by replacing the constant coefficients with periodic functions of fiber cutting angle [57, 97].

The periodic coefficients of the linear force model, commonly referred to as specific force coefficients (SFC), represent the cutting energy in the milling process. To

address the importance of SFC, there are some studies focused on the effect of fiber cutting angle on the specific cutting energy in CFRP machining experiments [98], in which they concluded that the specific cutting energy is bigger for the fiber cutting angle below 90°rather than the values above 90°.

Both radial and axial depth of cut was considered as constant values in the mechanistic force model in this work. However, the axial depth of cut is a major factor that might affect the accuracy of the model in predicting cutting forces and surface damages [99]. In reality, ϕ_j is affected by the helix angle on the cutting tool. Increasing the depth of cut or a larger value for the tool's helix angle will result in more variation in the value of ϕ_j for each layer of the composites. In the current study, because of choosing a relatively small depth of cut (a=0.8 mm), we neglect the effect of helix angle as an assumption to simplify the model.

In recent years, extensive investigations have been carried out on determining the specific force coefficients in CFRP milling operation [57, 100], highlighting their dependency on machining conditions (e.g., feedrate, fiber orientation, and fiber cutting angle). In these works, the SFC was identified experimentally by applying linear regression of measured cutting forces over a range of feedrates and different fiber orientations while the other cutting conditions have remained constant. However, this offline calibration method is time-consuming since several cutting tests are required to perform the linear regression analysis [101]. Also, the resulting calibrated coefficients, SFC, are only interpretable to the corresponding cutting parameters, selected tool geometry, and workpiece material.

When cutting conditions change during the process or tool wear increases, the model parameters identified by offline approaches lose accuracy; online identification methods are therefore required to adaptively recalibrate the model parameters during the process [84, 88, 102]. Furthermore, because of the strong linkage between the model parameters and the mechanics of chip formation, online monitoring of the SFC can also provide valuable information for process monitoring [103].

The majority of model identification research work has focused on offline methods [104] without much focus on the online identification approaches during the CFRP milling operation. This work aims to demonstrate the potential for process monitoring and control of machining operation in cutting CFRP.

In this chapter, the linear mechanistic force model in milling CFRP is first explained in the next section, followed by presenting two recursive methods to identify the unknown periodic parameters of the model in Section 3. A set of numerical

case studies are presented in Section 4 to validate the consistent performance of the presented identification methods in converging to actual values. In Sections 5 and 6, experimental cases are conducted to evaluate the performance of proposed online methods in identifying model parameters in milling unidirectional CFRP composites.

4.2 Problem Geometry

The important parameters in the mechanistic milling force model is presented in this section. Figure 4.1a shows the CFRP workpiece position when it is mounted on a CNC table machine and is being cut by a two-fluted cutting tool.

Schematics of tool-workpiece engagement in end-milling operation of CFRP is shown in Figure 4.1b. Vectors X and Y show Feed and Normal directions of the tool movement trajectory; fiber cutting angle is denoted β, and fiber orientation in a Uni-Directional layer is θ. Tangential and radial force components are also shown as f_t and f_r, respectively. The diameter of the cylindrical tool is denoted D which could be also referred to as radial depth of cut in full immersion engagement of tool-workpiece; and finally the axial depth of cut is denoted by parameter a. Both radial and axial depth of cut are considered as constant values in the force model analysis.

The tool moves in X direction at the constant feedrate of c mm/tooth while the spindle rotates clockwise at Ω rad/sec. The N flutes of the endmill are indexed $j = 1..N$, and the instantaneous immersion angle of the j^{th} tool measured from the normal to feed axis, Y, is denoted ϕ_j as shown in Figure 4.1.

4.3 Recursive Estimation of Specific Force Coefficients (SFC)

In order to identify the parameters of the mechanistic cutting force model in milling of CFRPs, as discussed in previous studies for traditional calibration of force model parameters, Kalla et al. [9] and Karpat et al. [57], the cutting forces applied in radial and tangential directions on each flute can be expressed as linear functions of the instantaneous uncut chip thickness $h(\phi_j)$ by considering the instantaneous fiber

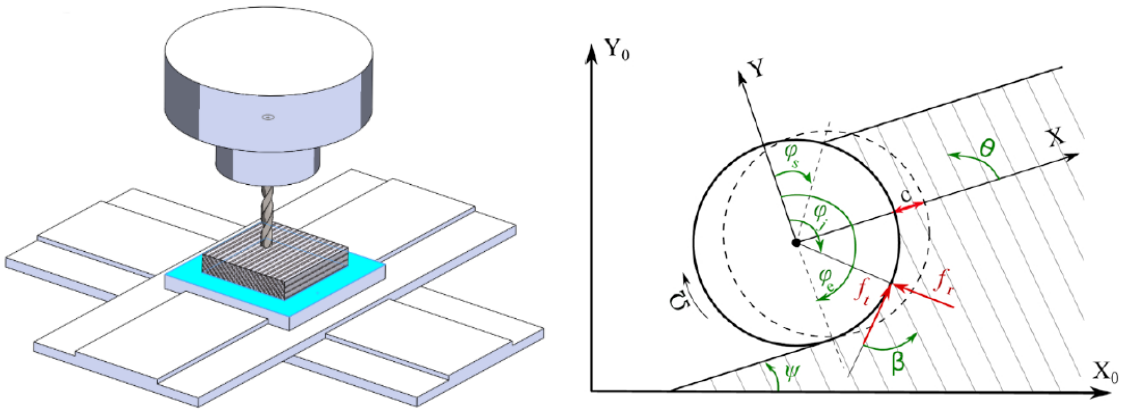

(a) (b)

Figure 4.1: (a)Interaction between tool and CFRP workpiece; (b)Schematics of main parameters in milling CFRP

orientation angle θ and tool rotation angle ϕ_j as following:

$$\begin{aligned} f_t &= K_{tc}(\beta).h(\phi_j).a + K_{te}(\beta).a \\ f_r &= K_{rc}(\beta).h(\phi_j).a + K_{re}(\beta).a \end{aligned} \tag{4.1}$$

To account for the variation of chip formation mechanics at various fibre cutting angles, the cutting and edge force coefficients are assumed to be functions of the fibre cutting angle. Since the variation of fibre cutting angle is periodic at half of the tool revolution period, the cutting and edge force coefficients are expressed as the Fourier series coefficients.Based on the proposed model, the following functions are used to describe the physical behavior of the specific cutting energy which consists of four distinct terms as

$$\begin{aligned} \hat{K}_{tc} &= \hat{K}_{tc0} + \hat{K}_{tc1}.\sin(2\beta) + \hat{K}_{tc2}.\cos(2\beta) \\ \hat{K}_{rc} &= \hat{K}_{rc0} + \hat{K}_{rc1}.\sin(2\beta) + \hat{K}_{rc2}.\cos(2\beta) \\ \hat{K}_{te} &= \hat{K}_{te0} + \hat{K}_{te1}.\sin(2\beta) + \hat{K}_{te2}.\cos(2\beta) \\ \hat{K}_{re} &= \hat{K}_{re0} + \hat{K}_{re1}.\sin(2\beta) + \hat{K}_{re2}.\cos(2\beta) \end{aligned} \tag{4.2}$$

Subsequently, by substituting Equation (4.2) in mechanistic force model, Equation (4.1), the final expression of cutting forces in milling of CFRP laminates can be extracted. With the simulated and experimentally measured forces, the specific force coefficients in Equation (4.2) can be determined by multi-variables Recursive Least

Squares (RLS) and Kalman filter methods. Subroutine programs have been developed to realize the recursive analysis in Matlab.

The accuracy of predictions for SFCs is analyzed which provides a measure of how well the estimation results are close to the experimental data. The formulation and equations in aforementioned methods have been already discussed thoroughly in the previous work by M. Farhadmanesh et al. [105] for isotropic metallic materials. However, in this chapter we are going to develop the mechanistic force model for milling of CFRPs.

The instantaneous immersion angle of each tooth depends on the spindle rotation speed and the angular immersion of the first tooth at $t = 0$, which is denoted ϕ_0:

$$\phi_j = \Omega t - \frac{2\pi(j-1)}{N} + \phi_0; \quad j = 1, ..., N \tag{4.3}$$

According to the discussion in previous chapter, the initial immersion angle, ϕ_0, is an unknown parameter and its estimation based on the measured forces will be discussed later in this chapter. Fiber cutting angle is also another parameter which is the summation of fiber orientation angle, θ, and tool rotation angle, ϕ_j, expressed in the following form:

$$\beta = \theta + \phi_j; \tag{4.4}$$

The overall machining forces applied on each tooth is decomposed into the radial component, f_r, and tangential component, f_t, as shown in Figure 4.1(b). In linear mechanistic models of machining forces, each of these components are assumed to be linear functions of the instantaneous chip thickness. However, in machining of CFRPs material, these components are harmonic function of the chip thickness and fiber cutting angle. By substitution of Equation (4.2) in Equation (4.1), we have:

$$\begin{aligned} f_t &= \Big[K_{tc0} + K_{tc1}\sin(2\beta) + K_{tc2}\cos(2\beta)\Big]h(\phi_j)a + \Big[K_{te0} + K_{te1}\sin(2\beta) + K_{te2}\cos(2\beta)\Big]a \\ f_r &= \Big[K_{rc0} + K_{rc1}\sin(2\beta) + K_{rc2}\cos(2\beta)\Big]h(\phi_j)a + \Big[K_{re0} + K_{re1}\sin(2\beta) + K_{re2}\cos(2\beta)\Big]a \end{aligned} \tag{4.5}$$

where a is the axial depth of cut and $h(\phi_j)$ is uncut chip thickness.

Mechanics of chip formation depends on the fibre cutting angle, β, which changes at various immersion angles, as described in Chapter 2.

The variation of chip thickness has been shown as dashed line in Figure 4.1(b) when the eccentricity of the tool rotation centre and its geometric centre is negligible and feed speed is much lower than cutting speed. From a practical point of view,

tool runout and the actual trochoidal trajectory of the cutting tooth alter the chip thickness the chip thickness and neglecting their effect can cause bias error in modelling. Therefore, in order to avoid this unnecessary error, instead of $h(\phi_j) = c.\sin\phi_j$ we consider the trochoidal trajectory and radial runout, [89], as discussed in previous chapter as well.

$$h(\phi_j) = q_1.\sin\phi_j + q_2.\sin\phi_j\cos\phi_j + q_3.\cos^2\phi_j + q_4 \tag{4.6}$$

where $q_i, i = 1..4$ are constants depending on feedrate per tooth, c [mm/tooth], and radial (R_0) and angular (γ) offset of tool rotation centre, O_R, from its geometric centre, O, as shown in Figure 4.1b:

$$\begin{aligned} q_1 &= c(1 + (-1)^j \tfrac{4R_0}{\pi D}\sin\gamma); \qquad q_2 = \tfrac{-2}{\pi D}c^2 \\ q_3 &= \tfrac{1}{D}c^2; \qquad q_4 = -2(-1)^j R_0\cos\gamma \end{aligned} \tag{4.7}$$

The overall measured forces in the coordinate reference system of the CNC machine, F_{X0} and F_{Y0}, could be projected to the feed and normal tool movement directions, F_X and F_Y, by the transformation matrix $T_X^{X_0}$. Then, a second rotation matrix,T_t^X, is applied that maps the forces from the feed and normal directions to the tangential and radial directions on the tool's cutting edge, f_t and f_r, as follows:

$$\begin{aligned} &\begin{Bmatrix} F_{X_0} \\ F_{Y_0} \end{Bmatrix} = T_{X,Y}^{X_0,Y_0}\sum_{j=1}^{N} g(\phi_j) T_{t,r}^{X,Y} \begin{Bmatrix} f_t \\ f_r \end{Bmatrix}; \\ &T_{t,r}^{X,Y} = \begin{bmatrix} -\cos(\phi_j) & -\sin(\phi_j) \\ \sin(\phi_j) & -\cos(\phi_j) \end{bmatrix}; \\ &T_{X,Y}^{X_0,Y_0} = \begin{bmatrix} \cos(\psi) & -\sin(\psi) \\ \sin(\psi) & \cos(\psi) \end{bmatrix}; \end{aligned} \tag{4.8}$$

The engagement of each flute with the cut is determined by the Heaviside function, $g(\phi_j)$, which is nonzero only if the corresponding immersion angle is between the start and exit angles, ϕ_{st} and ϕ_{ex}, shown in Figure 4.1:

$$g(\phi_j) = H(\phi_j - \phi_{st}) - H(\phi_j - \phi_{ex}); \quad j = 1..N \tag{4.9}$$

where $H(\phi_j)$ is unit step function. The start and exit angles are determined by the

radial depth of cut a, tool diameter, D, and the milling mode:

$$\begin{cases} \phi_{st} = 0 \quad \text{and} \quad \phi_{ex} = \cos^{-1}\left(1 - \frac{2b}{D}\right) & \text{upmilling} \\ \phi_{st} = \pi - \cos^{-1}\left(1 - \frac{2b}{D}\right) \quad \text{and} \quad \phi_{ex} = \pi & \text{downmilling} \end{cases} \tag{4.10}$$

4.4 Identification of SFC

In chapter 3, three methods were introduced to identify SFC in milling of homogeneous metallic materials, i.e. Aluminium, and then the derivation of model equations was presented. These methods included Recursive Least Squares (RLS), Kalman filter (KF), and Extended Kalman filter (EKF) methods. In this chapter, we are going to develop the aforementioned methods for the milling of CFRP which has non-homogeneous nature. The basic equations from previous chapter will be rewritten and updated here for readers convenience.

4.4.1 RLS method

This method is based on weighted least squares in which previous values taken in account for determining the future value. Each weight is exponentially assigned to each previous value of the actual system. The weights are updated recursively based on memory. The instantaneous feed and normal forces are used in Recursive Least Squares (RLS) algorithm to estimate the SFC. Considering the effect of tool runout in the chip thickness model described in Equation (4.6), and substituting it in the equation of overall feed and normal forces, Equation (4.5) will result in the following form to express the instantaneous forces as linear functions of SFC in discrete-time domain with constant sampling time of Δt:

$$\{F_k\} = [A_k(\phi_0)]\{K\} \tag{4.11}$$

where $\{F_k\} = \{F(k\Delta t)\}$ and $[A_k(\phi_0)] = [A(k\Delta t, \phi_0)]$ is a 2×12 matrix. The SFC unknown parameters are:

$$\{K\} = \begin{bmatrix} K_{tc0} & K_{tc1} & K_{tc2} & K_{rc0} & K_{rc1} & K_{rc2} & K_{te0} & K_{te1} & K_{te2} & K_{re0} & K_{re1} & K_{re2} \end{bmatrix}^T$$

$$[A(\phi_0, t)] = \begin{bmatrix} A_{11} & A_{12} & \cdots & A_{1-12} \\ A_{21} & A_{22} & \cdots & A_{2-12} \end{bmatrix};$$

$$A_{11} = A_{24} = -a \sum_{j=1}^{N} g(\phi_j) h(\phi_j) \cos\phi_j; \quad A_{12} = A_{25} = -a \sum_{j=1}^{N} g(\phi_j) h(\phi_j) \cos\phi_j \sin 2\beta;$$

$$A_{13} = A_{26} = -a \sum_{j=1}^{N} g(\phi_j) h(\phi_j) \cos\phi_j \cos 2\beta; \quad A_{14} = -A_{21} = -a \sum_{j=1}^{N} g(\phi_j) h(\phi_j) \sin\phi_j;$$

$$A_{15} = -A_{22} = -a \sum_{j=1}^{N} g(\phi_j) h(\phi_j) \sin\phi_j \sin 2\beta; \quad A_{16} = -A_{23} = -a \sum_{j=1}^{N} g(\phi_j) h(\phi_j) \sin\phi_j \cos 2\beta;$$

$$A_{17} = A_{2(10)} = -a \sum_{j=1}^{N} g(\phi_j) \cos\phi_j; \quad A_{18} = A_{2(11)} = -a \sum_{j=1}^{N} g(\phi_j) \cos\phi_j \sin 2\beta;$$

$$A_{19} = A_{2(12)} = -a \sum_{j=1}^{N} g(\phi_j) \cos\phi_j \cos 2\beta; \quad A_{1(10)} = -A_{27} = -a \sum_{j=1}^{N} g(\phi_j) \sin\phi_j;$$

$$A_{1(11)} = -A_{28} = -a \sum_{j=1}^{N} g(\phi_j) \sin\phi_j \sin 2\beta; \quad A_{1(12)} = -A_{29} = -a \sum_{j=1}^{N} g(\phi_j) \sin\phi_j \cos 2\beta; \tag{4.12}$$

Similar to what was explained in Section 3.3.2, a two-step solution is used to estimate the vector of SFC, $\{K\}$, from measured forces, $\left\{\tilde{F}_k\right\}$, in the presented RLS algorithm.

The first step is to determine the unknown parameter ϕ_0 by repeating Equation (4.11) over the first few tool revolutions, and then, the least squares estimation of $\{K\}$ is obtained from the system of linear equations. The optimum value of the ϕ_0 which leads to the smallest approximation residue(error) is selected in the range of 0-2π, and will be used in the second step of RLS algorithm.

The second step of RLS algorithm includes recursively updating the estimation of SFC by using the measured cutting forces at each discrete time step. Very similar to chapter 3, the unknown $\{K\}$ in Equation (4.11) will be determined by implementing a multi-output RLS algorithm in Matlab. The new cutting model and higher number of unknown parameters is the difference between the RLS algorithm in this chapter and previous one.

In the following equations, $\left\{\hat{K}_k\right\}$ denotes the estimation of SFC at the k^{th} time step, $[P_k]$ is the covariance matrix of estimation error which is updated at each time step, $[\lambda]$ is forgetting factor, and e_k is objective error function which is minimized at every updating step:

$$\left\{\hat{K}_k\right\} = \left\{\hat{K}_{(k-1)}\right\} + [P_k]\,[A_k]^T[\lambda]\{e_k\} \tag{4.13}$$

$$\{e_k\} = \left\{\tilde{F}_k\right\} - [A_k]\left\{\hat{K}_{k-1}\right\} \tag{4.14}$$

$$[P_k] = [P_{k-1}] + [P_{k-1}]\,[A_k]^T\left[[\lambda]^{-1} + [A_k]\,[P_{k-1}]\,[A_k]^T\right]^{-1}[A_k]\,[P_{k-1}] \tag{4.15}$$

As it was also mentioned before, the $\tilde{.}$ symbol is used to distinguish the measured forces, $\left\{\tilde{F}_k\right\}$, from their counterpart in the force model, $\{F_k\}$. In this chapter, forgetting factor and the initial values of the estimation and the corresponding error covariance are set to $\left\{\hat{K}_0\right\} = \begin{bmatrix} 0 & 0 & \cdots & 0 \end{bmatrix}^T_{1\times 12}$, $[\lambda] = 0.98[I]_{2\times 2}$, and $[P_0] = 10^5[I]_{12\times 12}$.

4.4.2 KF method

Kalman filter works on prediction-correction model used for linear and time-variant or time-invariant systems. Prediction model involves the actual system and the process noise .The update model involves updating the predicated or the estimated value with the observation noise. Kalman gain is calculated based on RLS algorithm in order to reach the optimal value within less amount of time.

Considering the high sampling rate of measured forces at each time step, SFC can be assumed constant stochastic processes. We can also consider the contribution of tool runout to the overall machining forces which is harmonic at the tool-passing frequency. The variation of milling forces due to runout effect can be modelled as harmonic processes at the tool-passing frequency with stochastic amplitudes. The dynamics of the variation of SFC and runout forces can therefore be described using the following discrete-time domain state space model:

$$\begin{aligned} \{q_{k+1}\} &= [\Psi_k]\,\{q_k\} + \{w_k\} \\ \{F_k\} &= [H_k]\,\{q_k\} + \{v_k\} \end{aligned} \tag{4.16}$$

where $\{q_k\}$ is the vector of state variables, $[\Psi_k]$ is state transition matrix, and $[H_k]$ is observation matrix. Process noise, $\{w_k\}$, and measurement noise, $\{v_k\}$, are assumed to be uncorrelated white noise with Gaussian distribution and known covariance matrices, $[Q]$ and $[R]$, respectively. The state vector includes SFC and runout forces:

$$\{q_k\}_{16\times 1} = \begin{bmatrix} K_{tc0}, & K_{tc1}, & K_{tc2}, & K_{rc0}, & K_{rc1}, & K_{rc2}, & K_{te0}, & K_{te1}, & ... \\ ... & K_{te2}, & K_{re0}, & K_{re1}, & K_{re2}, & F_{Xr}, & \dot{F}_{Xr}, & F_{Yr}, & \dot{F}_{Yr} \end{bmatrix}^T \tag{4.17}$$

The state transition matrix defines the progression of the constant SFC, harmonic runout forces, F_{Xr} and F_{Yr}, and their time-derivatives, $\dot{F}_{Xr}$ and $\dot{F}_{Yr}$, in each time step as follows:

$$[\Psi_k] = \begin{bmatrix} [I]_{12\times 12} & [0]_{12\times 2} & [0]_{12\times 2} \\ [0]_{2\times 12} & \begin{bmatrix} \cos\Omega\Delta t & \sin\Omega\Delta t \\ -\sin\Omega\Delta t & \cos\Omega\Delta t \end{bmatrix} & [0]_{2\times 2} \\ [0]_{2\times 12} & [0]_{2\times 2} & \begin{bmatrix} \cos\Omega\Delta t & \sin\Omega\Delta t \\ -\sin\Omega\Delta t & \cos\Omega\Delta t \end{bmatrix} \end{bmatrix}_{16\times 16} \tag{4.18}$$

Output vector comprises the forces in the feed and normal direction and thus the output matrix, $[H_k]$, is defined by combining runout forces with the forces in Equation (4.8), leading to the following equation:

$$[H]_{2\times 16} = \begin{bmatrix} & 1 & 0 & 0 & 0 \\ [A_k] & & & & \\ & 0 & 0 & 1 & 0 \end{bmatrix} \tag{4.19}$$

Note that because runout forces are considered as additional state variables, prior knowledge of runout parameters (R_0 and λ) is no longer necessary and their values in computing the observation matrix in Equation (4.19) are set to zero.

The KF algorithm is used as a state observer to estimate the states, $\{q_k\}$, based on the observations, i.e. measured forces, $\{F_k\}$. Details of Kalman filter design can be found in various references; for example, see [91]. A brief description of the method is also provided here. The algorithm consists of initialization, prediction, and correction steps.

Step(0) - Initialization

To initialize the algorithm, the expected value of the state vector at k=0 and the associated error covariance matrix are defined:

$$\begin{aligned} \{\hat{q}_0\}^+ &= E(\{q_0\}) \\ [P_0]^+ &= E\left[\left(\{q_0\} - \{\hat{q}_0\}^+\right)\left(\{q_0\} - \{\hat{q}_0\}^+\right)^T\right] \end{aligned} \tag{4.20}$$

where $[P_k]$ is the state estimation covariance matrix, $E\{\}$ stands for the Expected value, and the superscript "+" shows a posteriori estimation. The selected initial estimate of the state vector does not affect the identified SFC, and a relatively large values are selected for $[P_0]$ to increase the convergence rate of the algorithm.

Step(1) - Prediction

The state and covariance matrix at time step k are predicted as a new priori estimation by using the system model.

$$\begin{aligned} \{\hat{q}_{k+1}\}^- &= [\Psi_k]\{\hat{q}_k\}^+ \\ [P_{k+1}]^- &= [\Psi_k][P_k][\Psi_k]^T + [Q] \end{aligned} \tag{4.21}$$

Step(2) - Correction

In this step, the error between the measured forces and the forces predicted based on the priori state estimates is multiplied by the Kalman Gain, $[G_k]$, and the result is added to the priori estimation of the state vector to update it to its posteriori estimation. The priori estimation of the correlation matrix of the states is also updated to its posteriori estimation as follows:

$$\begin{aligned} \{\hat{q}_k\}^+ &= \{\hat{q}_k\}^- + [G_k]\left(\left\{\tilde{F}_k\right\} - [H_k]\{\hat{q}_k\}^-\right) \\ [G_k] &= [P_k]^-[H_k]^T\Big([H_k][P_k]^-[H_k]^T + [R]\Big)^{-1} \\ [P_k]^+ &= ([I] - [G_k][H_k])[P_k]^- \end{aligned} \tag{4.22}$$

4.4.3 EKF method

In both RLS and KF methods, the initial immersion angle of the first flute, ϕ_0, was obtained separately using the batch LSE method in Section 4.4.1. If this parameter is treated as another unknown state variable with constant stochastic dynamics, the state space model in Equation (4.16) will no longer be linear, but it can be described using the following nonlinear state space model:

$$\begin{aligned} \{q_{k+1}\} &= [\Psi_k]\{q_k\} + \{w_k\} \\ \{F_k\} &= h(\{q_k\}, k) + \{v_k\} \end{aligned} \tag{4.23}$$

where the state vector includes the initial immersion angle as the additional variable:

$$\{q_k\}_{17\times1} = \begin{bmatrix} K_{tc0}, & K_{tc1}, & K_{tc2}, & K_{rc0}, & K_{rc1}, & K_{rc2}, & K_{te0}, & K_{te1}, & ... & \\ ... & K_{te2}, & K_{re0}, & K_{re1}, & K_{re2}, & F_{Xr}, & \dot{F}_{Xr}, & F_{Yr}, & \dot{F}_{Yr}, & \phi_0 \end{bmatrix}^T \tag{4.24}$$

The state transition matrix will also be extended to a 17×17 matrix with zeros in all of the additional 17^{th} row and column, and 1 on the 17^{th} diagonal element. Comparing the linear model in Equation (4.16) and the nonlinear model in Equation (4.23), the linear output matrix, $[H_k]$ is converted to the time-varying nonlinear function $h\left(\{q_k\}, k\right)$. Extended Kalman filter (EKF) allows the estimation of state variables in non-linear systems with additive noise [91]. Assuming small sampling time Δt, the nonlinear output function ($h\left(\{q_k\}, k\right)$) can be linearized around its value at the priori estimation of the state vector in current time step, $\{\hat{q}_k\}^-$, leading to the following linearized output equation in the state space model:

$$\{F_k\} = h(\{\hat{q}_k\}^-, k) + [J_k]\left(\{q_k\} - \{\hat{q}_k\}^-\right) + \{v_k\}; \quad [J_k] = \left[\frac{\partial h}{\partial q}\right]_{q=\{\hat{q}_k\}^-} \tag{4.25}$$

Components of the Jacobian matrix,$[J_k]$, in Equation (4.25) are obtained by substituting F_X and F_Y from Equation (4.8) in the following equation:

$$[J_k] = \begin{bmatrix} \frac{\partial F_X}{\partial K_{tc0}} & \frac{\partial F_X}{\partial K_{tc1}} & \frac{\partial F_X}{\partial K_{tc2}} & \frac{\partial F_X}{\partial K_{rc0}} & ... & 1 & 0 & 0 & 0 & \frac{\partial F_X}{\partial \phi_0} \\ \frac{\partial F_Y}{\partial K_{tc0}} & \frac{\partial F_Y}{\partial K_{tc1}} & \frac{\partial F_Y}{\partial K_{tc2}} & \frac{\partial F_Y}{\partial K_{rc0}} & ... & 0 & 0 & 1 & 0 & \frac{\partial F_Y}{\partial \phi_0} \end{bmatrix}_{\{\hat{q_k}\}^-} \tag{4.26}$$

The three stages, initialization, prediction, and correction in Kalman filter algorithm are also used to update the estimate of the state variables from the linearized state space model in Eqs.4.23 and 4.25 as well. While the initialization and prediction stages are similar to Equation (4.20) and 4.21, the correction stage in Extended Kalman filter changes to the following:

$$\begin{aligned} &\{\hat{q}_k\}^+ = \{\hat{q}_k\}^- + [G_k]\left(\left\{\tilde{F}_k\right\} - h(\{\hat{q}_k\}^-, k)\right) \\ &[G_k] = [P_k]^-[J_k]^T\Big([J_k]\,[P_k]^-[J_k]^T + [R]\Big)^{-1} \\ &[P_k]^+ = (I - [G_k]\,[J_k])\,[P_k]^- \end{aligned} \tag{4.27}$$

4.4.4 Kalman filter stability

As a time-domain filter, Kalman filter is able to accommodate time-variable parameter. However there are some situations which the filter will not approach a steady-state condition which results in unstability in the identification results. In this section, the stability of the digital filter is analyzed using z-transform method and the formulation is provided assuming that the Kalman filter under consideration a constant-gain condition. The main estimate update equation which discussed in previous section, (4.22), could be rewritten as a first-order vector difference equation in which we replace $\{\hat{q}_k\}^-$ with $[\Psi_{k-1}]\{\hat{q}_{k-1}\}^+$:

$$\{\hat{q}_k\}^+ = \Big([\Psi_{k-1}] - [G_k]\,[H_k]\,[\Psi_{k-1}]\Big)\{\hat{q}_{k-1}\}^+ + [G_k]\left\{\tilde{F}_k\right\} \tag{4.28}$$

By taking the z-transform on both of the above equation, we can write it in the z-domain as following:

$$\{\hat{q}_k(z)\}^+ = \Big([\Psi_{k-1}] - [G_k]\,[H_k]\,[\Psi_{k-1}]\Big)z^{-1}\{\hat{q}_k(z)\}^+ + [G_k]\left\{\tilde{F}_k(z)\right\} \tag{4.29}$$

where z denotes the usual z-transform variable. $\hat{q}_k(z)$ and $\tilde{F}_k(z)$ also refer to to z-transformed vector of state variables and measurement, respectively. Rearranging both sides of the 4.29 will result in:

$$\Big[z\,[I] - ([\Psi_{k-1}] - [G_k]\,[H_k]\,[\Psi_{k-1}])\Big]\hat{q}_k(z)^+ = z\,[G_k]\left\{\tilde{F}_k(z)\right\} \tag{4.30}$$

According to linear system theory, the term in the bracket on the left side of 4.30 describes the natural modes of the system, and its determinant provides the characteristic polynomial for the system. the root of the following equation gives information about the stability of the Kalman filter.

$$Characteristic \quad polynomial = \Big|z\,[I] - ([\Psi_{k-1}] - [G_k]\,[H_k]\,[\Psi_{k-1}])\Big| \tag{4.31}$$

Since the roots of the characteristic equation are placed inside the unit circle in z-plane, the filter is stable. If any root lies outside the unit circle, the filter will be unstable and control algorithm will detect this unstable behaviour. These roots can be determined by finding calculating the eigenvalues of the term $([\Psi_{k-1}] - [G_k]\,[H_k]\,[\Psi_{k-1}])$.

4.5 Numerical Simulation

A set of numerical simulations are presented in this section to study the consistency and convergence of RLS and KF, and EKF methods discussed in previous section. Cutting forces in feed and normal directions, F_x and F_y, are simulated at 0.12 ms intervals by using the following Force coefficients extracted from offline average-force method. These functions were identified experimentally by the offline regression method in Chapter 2, [100]:

$$\begin{aligned}\hat{K}_{tc} &= 641 - 235sin2\beta - 296cos2\beta \\ \hat{K}_{rc} &= 476 - 275sin2\beta - 131cos2\beta \\ \hat{K}_{te} &= 4.7 + 6.4sin2\beta - 9.6cos2\beta \\ \hat{K}_{re} &= 9.6 + 7.5sin2\beta - 8.7cos2\beta\end{aligned} \tag{4.32}$$

Figure 4.2a shows the whole process of SFC estimation as a reverse method based on the applied cutting conditions in the figure. Table 4.1 shows the parameters which will

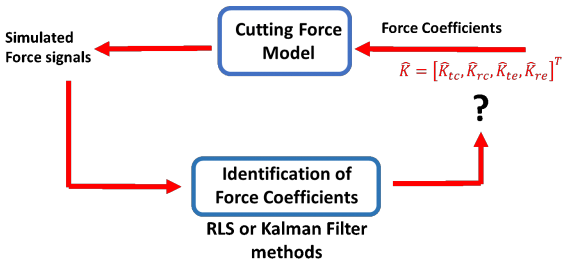

(a)

- Number of flutes: 2
- Spindle speed: 5000 rpm
- Feedrate: 0.1 mm/tooth
- Axial depth of cut: 0.8mm
- ϕ_0=60 deg
- θ=30 deg
- $\psi = 0$ deg
- Full Immersion.

(b)

Figure 4.2: (a)Schematics of the identification process; (b)cutting conditions and parameters

be estimated for each identification method. The initialization parameters applied for RLS, and KF algorithms can be also seen in the following table. The measurement noise covariance, $[R]$, is measured from the baseline (i.e. air cutting) of the measured forces. Determination of the process noise covariance $[Q]$ in KF method is challenging; The correct $[Q]$ is defined by manually trying various values for $[Q]$ and finding the optimum diagonal element of the process noise matrix for which all of the SFC almost converge to constant values in this case study.

Two sets of simulations were performed. In the first set, the tool runout and measurement noise are assumed to be zero. In the second set, the radial and angular

Table 4.1: The initialization parameters and variables applied for RLS, KF, EKF algorithms. $[R], [Q]$, and $[P_0]$ are diagonal matrices, and $Q_{(i,i)}$ and $P_{0(i,i)}$ denote the i^{th} diagonal elements of $[Q]$ and $[P_0]$ matrices, respectively.

RLS	KF	EKF
$[\lambda] = 0.98[I]_{2\times2}$	$[R] = 2 \times 10^{-2}[I]_{2\times2}$	$[R] = 2 \times 10^{-2}[I]_{2\times2}$
$[P_0] = 10^2[I]_{12\times12}$	$[Q] = 10^{-7}[I]_{16\times16}$	$Q_{(i,i)} = \begin{cases} 10^{-8};\ i = 1, ..., 16 \\ 10^{-10};\ i = 17 \end{cases}$
$\{\hat{K}_0\} = \{0\}_{12\times1}$	$[P_0]^+ = 10^7[I]_{16\times16}$	$P_{0(i,i)} = \begin{cases} 10^7;\ i = 1, ..., 16 \\ 10^3;\ i = 17 \end{cases}$
	$\{q_0\}^+ = \{0\}_{16\times1}$	$\{q_0\}^+ = \{0\}_{17\times1}$
Initial values for estimated parameters: $K_{tc0} = 600; K_{tc1} = -200; K_{tc0} = -300; K_{rc0} = 450; K_{rc1} = -250; K_{rc2} = -100;$ $K_{te0} = K_{te1} = K_{te2} = K_{re0} = K_{re1} = K_{re2} = 0;$ $\tilde{F}_{Xr} = \dot{\tilde{F}}_{Xr} = \tilde{F}_{Yr} = \dot{\tilde{F}}_{Yr} = 0; \phi_0 = 62^o;$		

offset parameters of runout are assumed $R_0 = 5\mu m$ and $\gamma = 0°$, and measurement noise is added to the simulated forces. Signal to noise ratio (SNR) in the second set is 17.8 dB and 18.6 dB for the force signals F_x and F_y, respectively. The cutting forces from the two sets of simulations are shown in Figure 4.3. The initial immersion angle in both simulations are assumed $\phi_0 = 60°$. In order to estimate the initial immersion

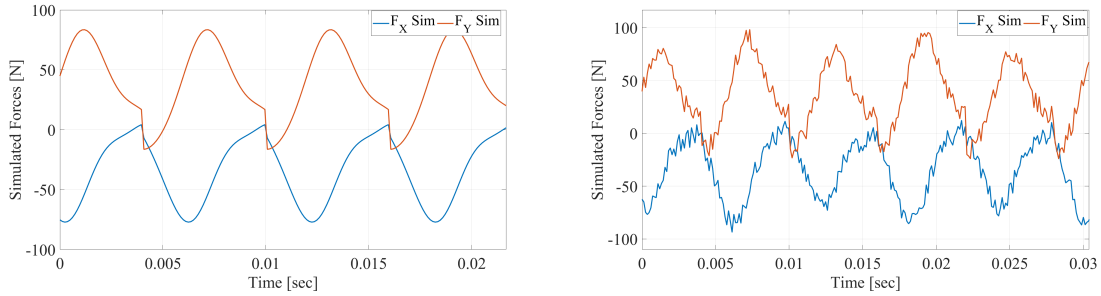

(a) (b)

Figure 4.3: (a)Simulated Forces (No runout No noise) based on cutting conditions on 4.1; (b)Simulated Forces (considering $R_0 = 5\mu m$ and tool runout $\gamma = 0°$, measurement noise of 17.8 dB SNR in F_x and 18.6 dB SNR in F_y)

angle of the tool, a Least Squares Estimation method is applied on the simulated forces. In Figure 4.4, the results for ϕ_0 show accurate estimation of 60°for the first set, and 61.1°for the second set in presence of noise and tool runout. These values are used as optimum estimation of ϕ_0 in the RLS and KF methods.

In Figure 4.5, convergence of SFC is shown when the cutting forces resulting from

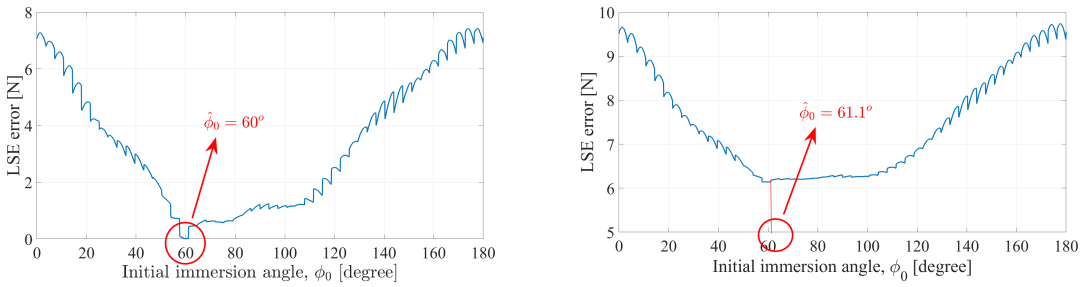

(a) (b)

Figure 4.4: Identification of unknown initial immersion angle, ϕ_0, based on error estimation (residue) of batch Least Square Estimation for two sets of (a)No runout No noise, (b)considering the effect of tool runout and noise

the first set of simulations (i.e. no runout and noise) are used in the RLS, KF, and EKF algorithms. The initialization parameters applied in each of the three methods are presented in Table 4.1. In Figure 4.5, RLS and KF algorithms converge to the true values used in simulations. The effect of linearization errors in EKF is negligible, and it converges to a true estimation value without considerable estimation bias. As shown in this figure, the EKF algorithm, due to linearization errors, converges to a biased estimation, but the estimation bias is negligible (2%). In the KF algorithm, the runout forces also converge to the true value (zero runout). In the EKF, the initial immersion angle ϕ_0 is considered as an additional state variable, which converges to its true value, 60°.

Figure 4.6 also shows the convergence of the RLS, KF, and EKF algorithms when forces simulated in the second set (with noise and runout) are used. As illustrated in the figure, RLS and KF converge to the true values with a negligible bias error. This error is more tangible in K_{tc} and K_{te} convergence diagram shown in part (a,c) of the figure. The deterioration of the performance of the RLS and KF algorithms is intensified with the error in estimating the initial immersion angle, ϕ_0, in the first step of estimation process. The estimated ϕ_0 used in RLS and KF is 61.1^o, different from true value 60^o. As a result of this uncertainty in model parameter, a bias error is anticipated to emerge in the identification results. In order to omit this bias error and to remove the effect of the initial value of the estimated variables on the performance of RLS and KF, we need to run the KF and RLS algorithms including actual value of $\phi_0 = 60°$.

As shown in Figure 4.6, the SFCs, ϕ_0, and running forces are stable and converge

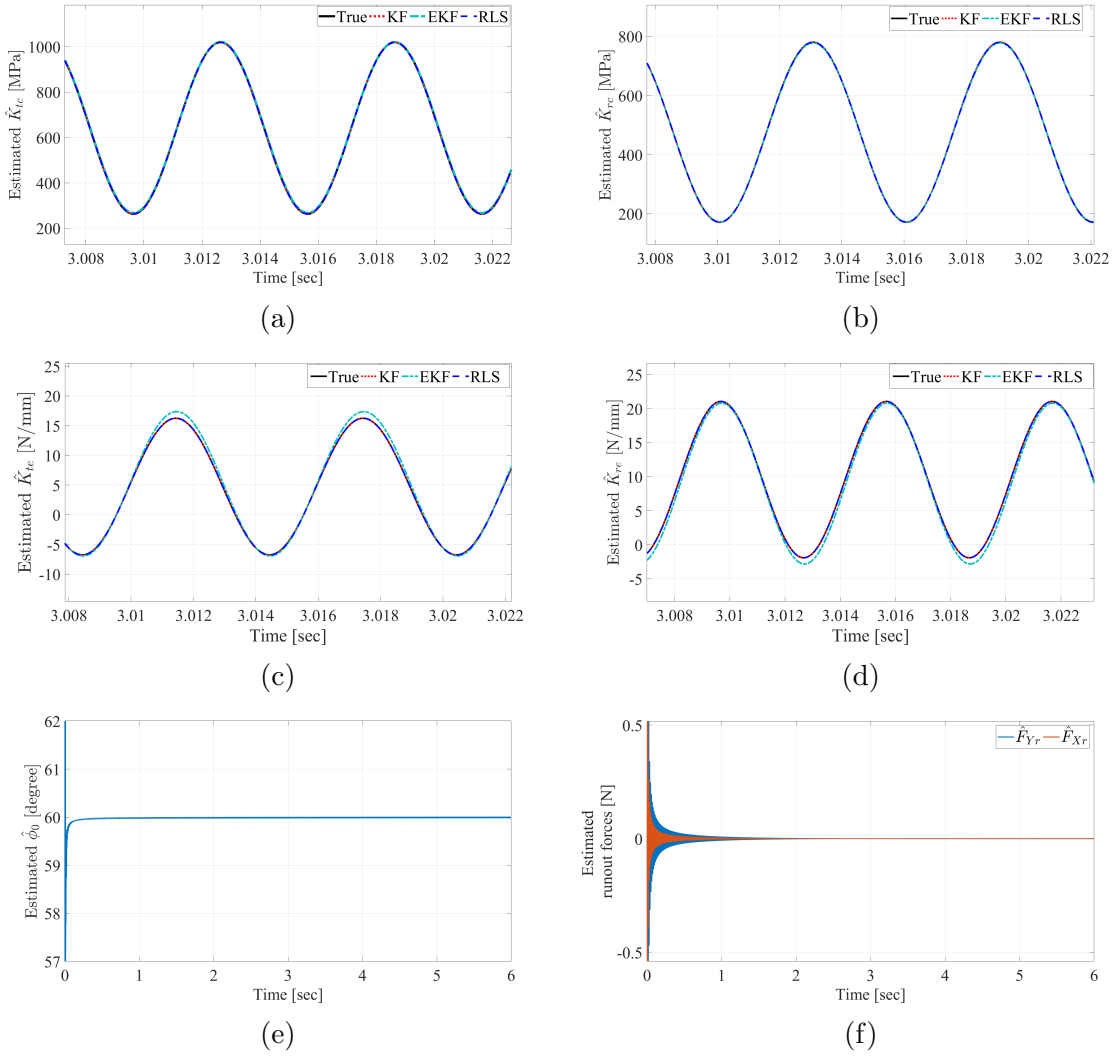

Figure 4.5: Numerical simulation results without considering runout and measurement noise. (a)–(d) Convergence of SFC estimated by RLS, KF, and EKF; (e) Initial immersion angle estimated by EKF. (f)runout forces estimated by EKF during milling process. Forces simulated using force coefficients:
$K_{tc} = 641 - 235\sin 2\beta - 296\cos 2\beta$
$K_{rc} = 476 - 275\sin 2\beta - 131\cos 2\beta$
$K_{te} = 4.7 + 6.4\sin 2\beta - 9.6\cos 2\beta$
$K_{re} = 9.6 + 7.5\sin 2\beta - 8.7\cos 2\beta$
$c = 0.06mm/tooth$, $\Omega = 5000rev/min$, axial depth of cut $a = 0.8mm$, $\Delta t = 0.12ms$, and full immersion engagement.

to the true values of themselves as well.

A comparison of the estimated specific force coefficients for three methods RLS, SKF, and EKF has been depicted in Figure 4.7. The numerical simulation results are

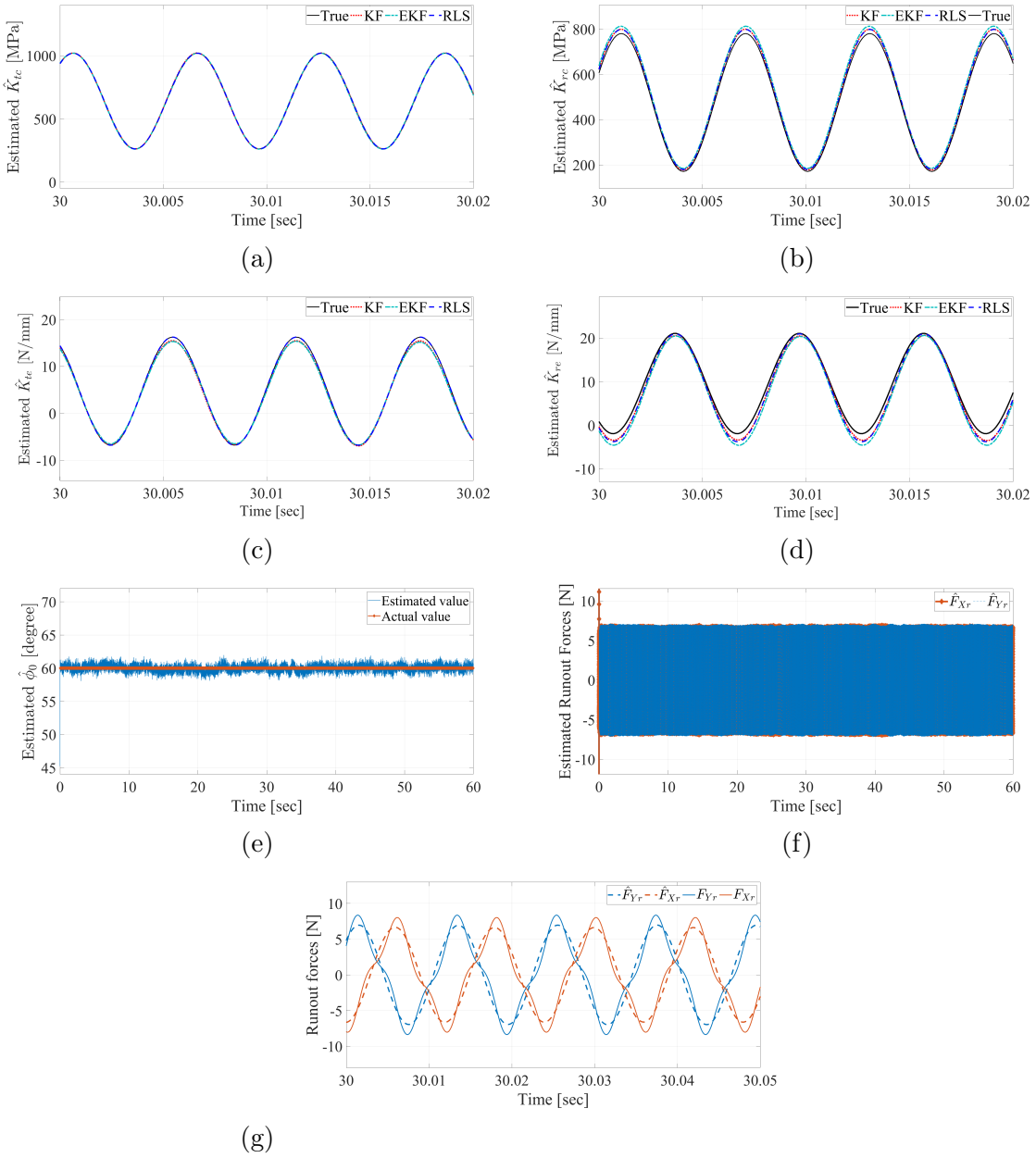

Figure 4.6: Numerical simulation results considering measurement noise and tool runout. (a-d) Convergence of SFC estimated by RLS, KF, and EKF; (e)Initial immersion angle estimated by EKF. (f)runout forces estimated by EKF during the milling process. (g)Comparison of actual vs. estimated running forces. Forces simulated using force coefficients in previous figure. $c = 0.06mm/tooth$, $\Omega = 5000rev/min$, axial depth of cut $a = 0.8mm$, $\Delta t = 0.12ms$, and full immersion engagement. Runout parameters are assumed $R_0 = 10\mu$m, $\gamma = 0°$, and signal to noise ratio (SNR) is 15 dB and 18 dB for the force signals F_X and F_Y

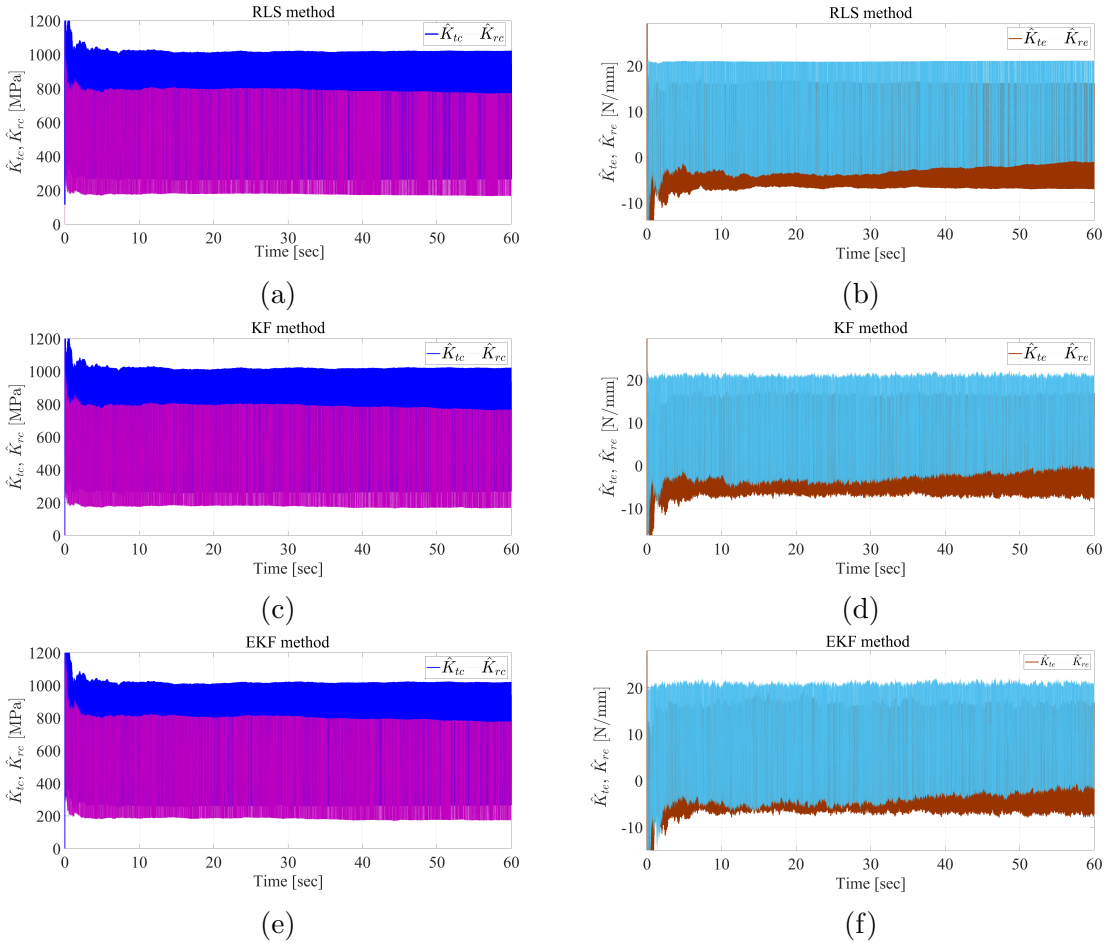

Figure 4.7: Identification of SFC from the forces numerically simulated at $c = 0.1mm/tooth$

used as proof of concept for validation of mentioned methods in milling of CFRP. It also shows that equations in algorithms are correct and working well.

4.5.1 Effect of the initial value of the estimated variables

the initial starting point of the recursive process in Extended Kalman filter plays a big role in convergence of the estimated parameters to their actual values. The initial value of the estimated variables are presumably the best estimations prior to receiving any measurement. Therefore, in presence of a large error in guessing the initial values, the first order approximation used in the linearization will be poor which leads to divergence occurrence problem. Even with perfect arithmetic and zero uncertainty in the model, this poor approximation could cause a slower transition

phase in the convergence process.

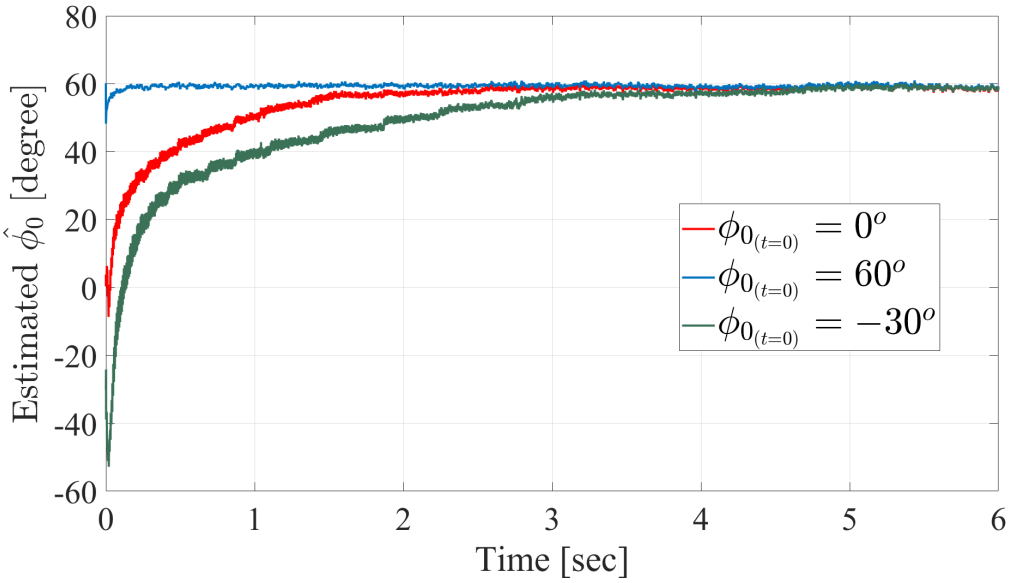

Figure 4.8: The effect of different initial value of ϕ_0 on the performance of EKF identification method

As you can see in Figure 4.8, three different random initial values have been selected for the parameter ϕ_0, and the response of the identification EKF algorithm has been plotted for these different initial values. The more the initial guess is close to actual value of ϕ_0, the sooner the estimated parameter converges to it, and the transition phase is shorter. By choosing $\phi_0 = 60$°as the initial value, EKF identification method has its fastest convergence.

4.6 Experimental Study

The importance of experimental study is to show the accuracy and viability of proposed numerical analysis in an actual process. Mechanistic force models establish the relationship between cutting force and machining parameters by using data fitting methods [17]. Establishment of force models in conventional methods requires lots of experiments which is time-consuming and not efficient. In this work, actual measured cutting forces are used to identify the SFC in milling of CFRP by using online methods such as Recursive Least Squares (RLS) and Kalman filter (KF).

The Extended Kalman filter can diverge if the reference about which the linearization take place is poor [106]. In the mechanistic force model presented in Section 4.4.3, the estimated parameters of Equation (4.24) are the reference variables about which the model is linearized. One of these variables is ϕ_0 which the linearization is poor about it. So, poor linearization of ϕ_0 causes a large error in initial states $\hat{K}_0^-$ and covariance matrix P_0^-. A very large P_0^- combined with low-noise measurements at the first step will cause the P matrix to "jump" from a very large value to a small value in one step. In principle, this is permissible. However, this can lead to numerical problems. A non-positive-definite P matrix at any point in the recursive process usually leads to divergence.

Also, because the error in initial value of $\hat{\phi}_0^-$ is large, the first-order approximation used in the linearization will be poor, and divergence occurs, even with perfect arithmetic. Due to these reasons, EKF has not been used in the experimental analysis in this section.

Mechanical models apply metal cutting theory to relate cutting force to milling process parameters, such as tool geometry, feedrate, etc. Mechanical models for milling of fiber-reinforced PMCs are developed on the basis of metal cutting theories. The limitation is that the detailed cutting mechanism of fiber-reinforced PMCs machining is neglected, which results in inaccurate prediction of cutting forces in some of the fiber orientations. However, it has been shown that using a simplified mechanistic cutting force model in the identification algorithm could also deliver acceptable results which can be used in online application.

In this section, measured cutting forces are used instead of the numerical simulated forces to identify the SFC in milling of CFRP. The results will be shown in 6 different fiber orientations by using both RLS and KF approaches.

4.6.1 Variation of CFRP fiber orientation

According to Hintze et al. [29], two factors mainly influence the occurrence of uncut fibers and delamination in contour milled CFRP parts. These parameters are fiber cutting angle and tool wear. Due to anisotropic properties of CFRPs, they discussed that delamination and machined surface quality changes with different fiber orientations and tool conditions.

Figure 4.9 depicts images of the milled slot in material with different fiber orientations but the same tool geometry. As shown in their article [107], there are two

regions denoted by critical and non-critical areas and marked by red and green colors, respectively. For directions $\theta = 0°$, $30°$, $60°$, delamination happens exclusively in front

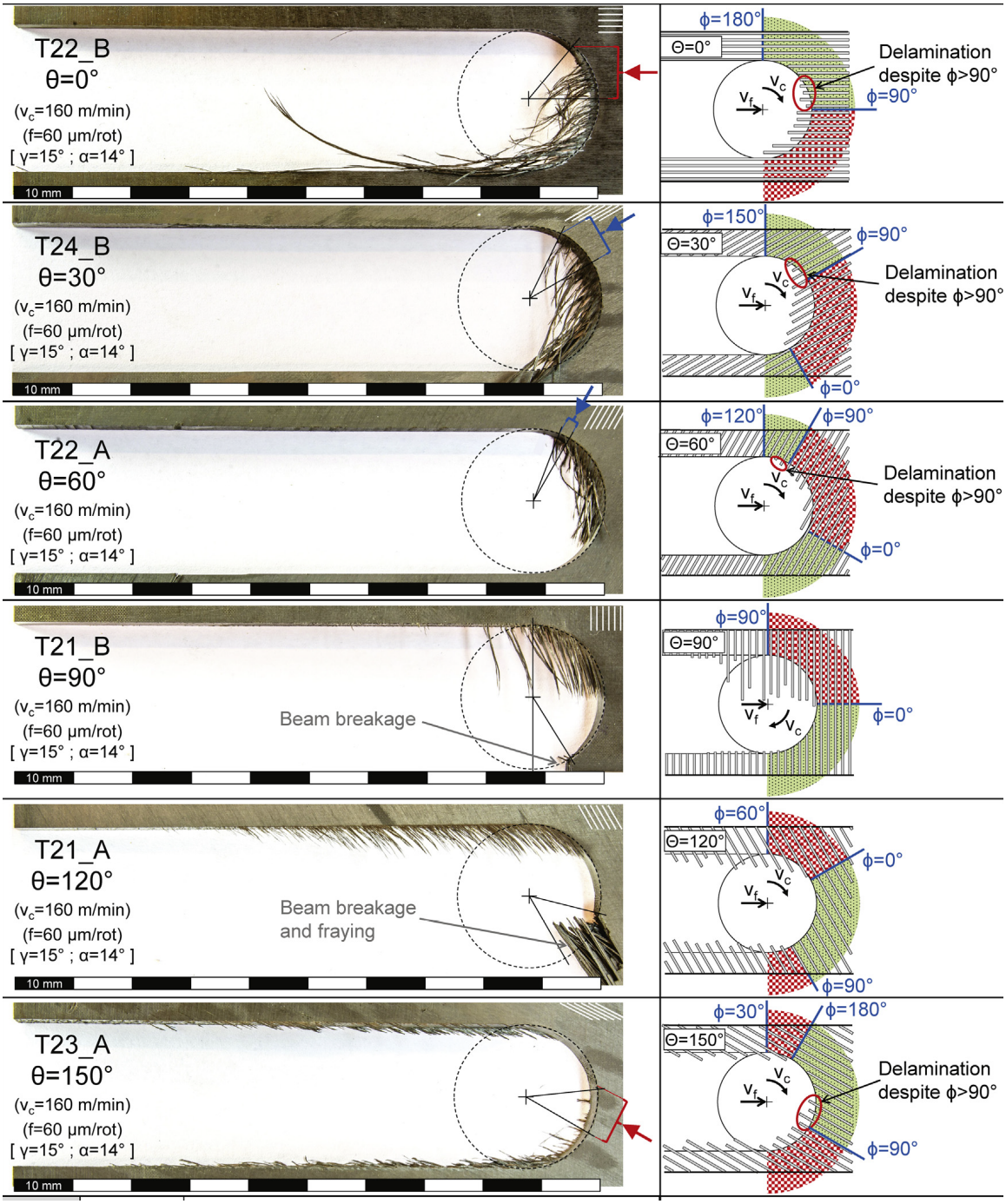

Figure 4.9: Quality in milling of CFRP for different fiber orientations $\theta = 0°$, $30°$, $60°$, $90°$, $120°$, $150°$[107].

of the tool in feed direction where the fiber cutting angle is between 90-130 degrees (critical area). The other directions $\theta = 90^\circ$, 120°, 150°show damages on the up- and down-milled edges.

In this work, only the effect of fiber cutting angle has been considered in identification of SFC due to its higher importance. In order to measure the tangential and radial forces, slot milling tests have been conducted in six different fiber orientations ($\theta = 0^\circ$, 30°, 60°, 90°, 120°, 150°) for Uni-Directional CFRPs. The CFRP composite used in the milling tests were fabricated from resin polymer and carbon fibers of 60% volume. Two different types of Uni-Directional laminates consisting 20 plies with the thickness of 0.8 mm at each layer and fiber orientations of 0°and 90°are selected in the experiments.

The machining conditions for each test were as follows: Spindle speed was 3000 round/min, axial depth of cut was 0.8 mm, and radial depth of cut was 9.525 mm. The milling process was performed by using a 2-flute Tungsten Carbide end mill with 3/8" diameter and 3° normal rake. Cutting forces were measured by a Kistler 9255 table dynamometer, Cutpro application was used to store and process the measured force signals. More information on milling conditions has been provided in Chapter 2, [100].

4.6.2 Chip thickness and tool rotation angle

From the measured forces F_x and F_y, we can obtain the forces in tangential and radial directions, f_t and f_r, as it was shown in Equation (4.8) in previous section. This projection transforms the measured forces from global coordinate system attached to the CNC machine table to the coordinate system attached to the tool. Force f_t is in the cutting speed direction while force f_r is in the radial direction perpendicular to f_t.

For smoothing noisy data, a moving-average filter is usually used as a common method. We implement a moving-average low pass filter which slides a window of length $windowSize = 15$ along the input force vector, computing averages of the data contained in each window. A zero-phase version of the digital filter is obtained here using the Matlab function $filtfilt$ in which the filter takes a few time samples to adjust to the signal and smooth the force data with a slight phase delay. By then filtering backward in time, we can cancel out the phase delay. In Figure 4.10, the cutting forces f_t andf_r are plotted as a function of the engagement angle, ϕ_j, for

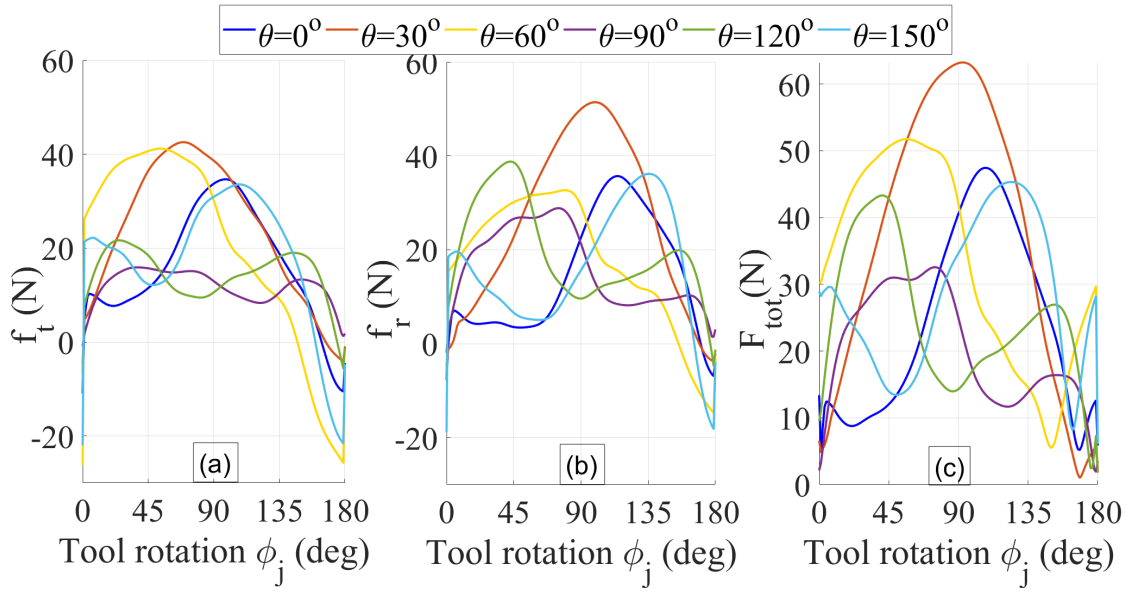

Figure 4.10: Measured Forces vs. Tool rotation angle, in milling UD CFRP for one flute engagement

six different fiber orientations in a full engagement of tool-workpiece during a single half-rotation of tool. Figure 4.10(c) is the lateral forces which is plotted according to $F_{lat} = \sqrt{{f_t}^2 + {f_r}^2}$. As shown in Figure 4.10, maximum forces f_t and f_r do not necessarily occur at $\phi_j = 90°$due to anisotropic property of composite materials. The extrema magnitude depends on the fiber cutting angle β and actual depth of cut. The mean value of the measured cutting forces at each half-rotation is plotted in the figure. This mean value has been calculated by taking the average of cutting forces over the entire period of data measurements.

While plotting the measured cutting forces for each one of these six different fiber orientations, $\theta = 0°$,...,$150°$, the initial value of the parameter ϕ_0 should be first identified in the same way explained in Section 4.4.1, and then, we can plot the measured forces versus rotation angle ϕ_j. Therefore, the accuracy of the plotted forces in Figure 4.10 strongly depends on the correct estimation of unknown initial immersion angle ϕ_0. In Figure 4.11, cutting forces are plotted over the fiber cutting angle β. Maximum cutting force f_t happens at $\beta = 90^o$. It is also shown that maximum radial force f_r usually occurs around $\beta = 135^o$. These results are consistent with the results in the previous studies done by Wang et al. [17], and Zaghbani et al. [108].

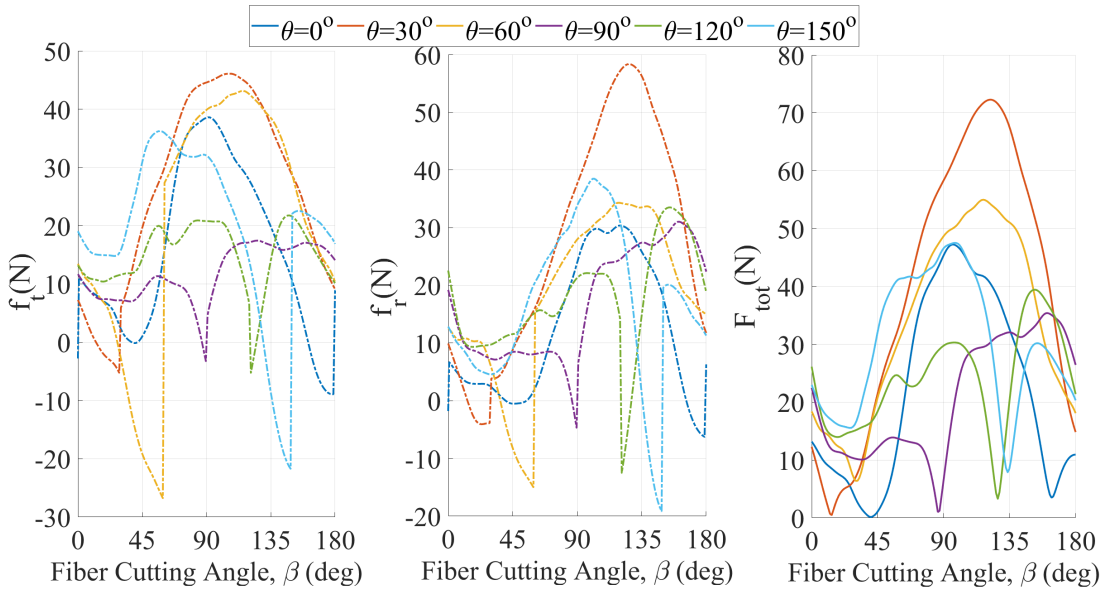

Figure 4.11: Measured Forces vs. Fiber cutting angle, in milling UD CFRP for one flute engagement

The effect of cutting mechanism can be illustrated in Figs. 4.10 and 4.11, where the magnitude of the peaks of f_t in fiber orientations $\theta = 30°$and $60°$has the highest value due to cutting mechanism related to shearing or debonding at fiber/resin interface and bending and subsequent breaking of carbon fibers. At $\theta = 0°$, shear fracture of fiber perpendicular to fiber direction happens in the maximum chip thickness area. At $\theta = 90°$which has the minimum amount of cutting forces, fiber/resin interface separation occurs which is dominated by in-plane shear stress in the area around $\phi = 90°$.

4.6.3 Parameters estimation methods

In the mechanistic force model, cutting forces are proportional to chip thickness and axial depth of cut. This relationship is defined by specific force coefficients (SFCs), which are considered as unknown variables in experimental analysis, $K_{tc}, K_{rc}, K_{te}, K_{re}$. Two identification methods of Standard Kalman filter and Recursive Least Squares are used to estimate SFCs recursively for the experimental studies.

In addition to force coefficients, runout forces, F_{Xr}, F_{Yr} can be also modeled as unknown parameters in kalman filter algorithm to increase the accuracy of estimation

results as well as identifying the runout effect during the milling process without having prior knowledge about tool eccentricity.

In order to reduce the complexity of model, the number of unknown parameters are decreased by considering the Edge force coefficients $K_{te} = 4.7N/mm$ and $K_{re} = 9.6N/mm$ as known parameters calculated from the average-force method in previous study. So, these known edge force coefficients will be directly applied to the estimated forces in RLS algorithm as constant values. Therefore, the following variables are used in the estimation process in kalman filter. In RLS method, the first six parameters are considered as the unknown variables:

$$Variables : [\hat{K}_{tc0}, \hat{K}_{tc1}, \hat{K}_{tc2}, \hat{K}_{rc0}, \hat{K}_{rc1}, \hat{K}_{rc2}, \tilde{F}_{Xr}, \dot{\tilde{F}}_{Xr}, \tilde{F}_{Yr}, \dot{\tilde{F}}_{Yr}]; \tag{4.33}$$

4.6.4 Standard Kalman filter results

Unknown parameters in Equation (4.33) are used as state variables the state space model in Kalman filter algorithm. Chip thickness and depth of cut are defined as input to state model while the cutting forces are output. The goal is to estimate state variables, including cutting force coefficients and runout forces by using a Kalman filter state observer. Estimation algorithm is executed for six different fiber orientations θ=0°, 30°, 60°, 90°, 120°, and 150°; and the results are depicted in Figures 4.12-4.17, respectively.

Table 4.2 shows experimental results for variation of estimated cutting force coefficients and cutting forces in milling of CFRPs for different fiber orientations. The magnitude of the minimum and maximum values for the cutting coefficients and cutting forces has been reported in this table. The values for the cutting coefficients are estimated from the Kalman filter algorithm while the cutting forces are measured and read from the dynamometer. This table shows the effect of different cutting mechanisms in various fiber orientations on the specific force coefficients.

The maximum value for cutting coefficients occurs when θ=120°in which K_{tc} and K_{rc} reach to 850 [MPa] and 1250 [MPa], respectively. According to R. Voss [107], as shown in Figure 4.9 for fiber orientation θ=120°, beam breakage and fraying happens around the down-milled edge of the tool-workpiece engagement where fiber cutting angle, β, is closed to 90°. So, this direction cannot be analyzed in details due to fraying effects at the down-milled edge and deficient stability of the unidirectional material which results in higher energy consumption for the cutting process.

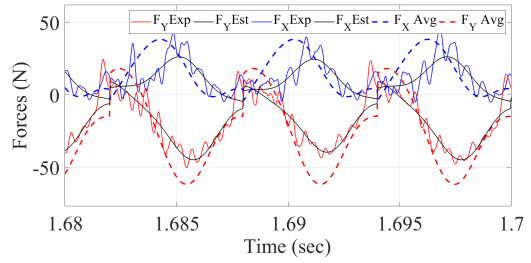

(a) Measured, estimated and average cutting forces

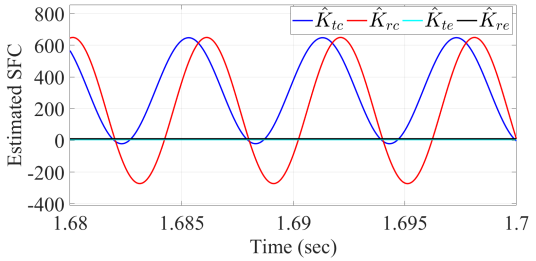

(b) Estimated Cutting Force Coefficients

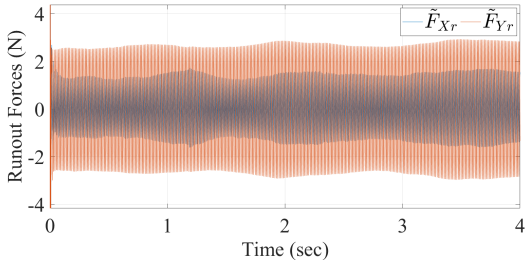

(c) Estimated runout forces in directions X,Y

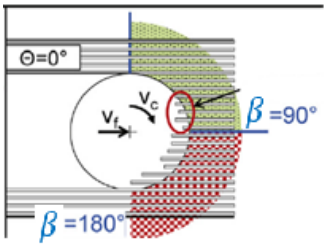

(d) Schematics of tool-workpiece engagement [107].

Figure 4.12: Kalman filter results for $\theta = 0$

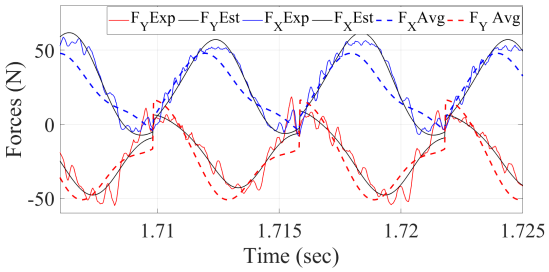

(a) Measured, estimated and average cutting forces

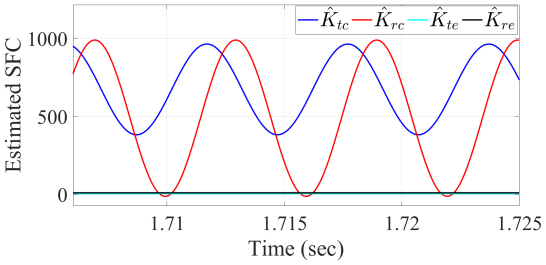

(b) Estimated Cutting Force Coefficients

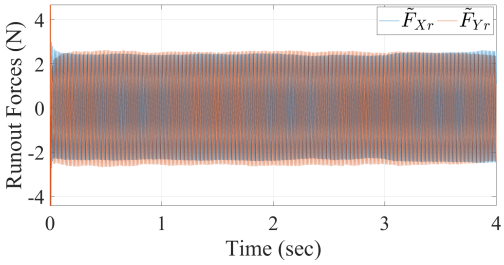

(c) Estimated runout forces in directions X,Y

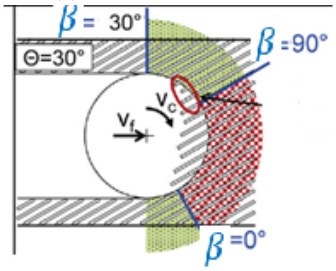

(d) Schematics of tool-workpiece engagement [107].

Figure 4.13: Kalman filter results for $\theta = 30^o$

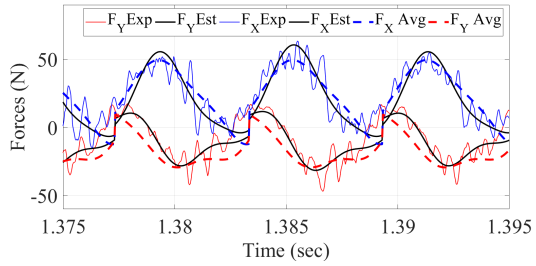

(a) Measured, estimated and average cutting forces

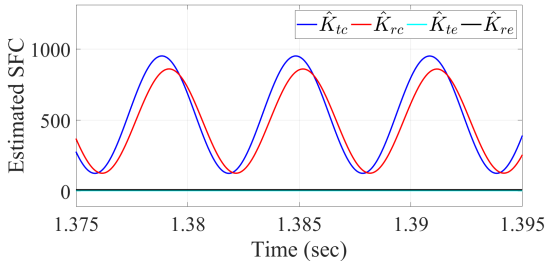

(b) Estimated Cutting Force Coefficients

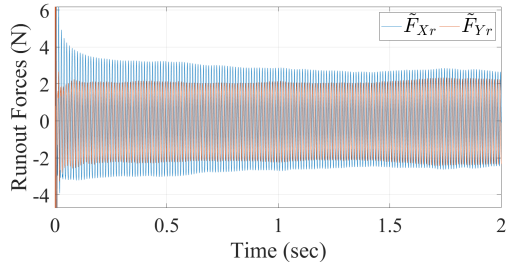

(c) Estimated runout forces in directions X,Y

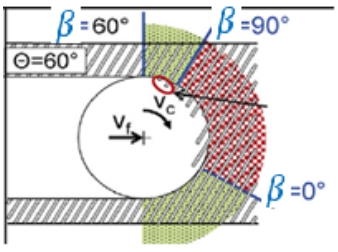

(d) Schematics of tool-workpiece engagement [107].

Figure 4.14: Kalman filter results for $\theta = 60$

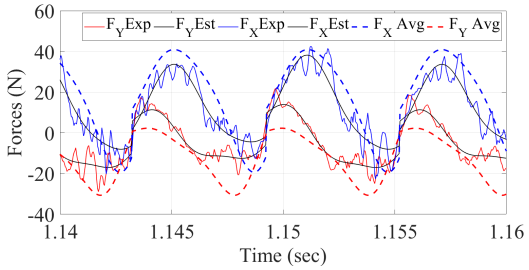

(a) Measured, estimated and average cutting forces

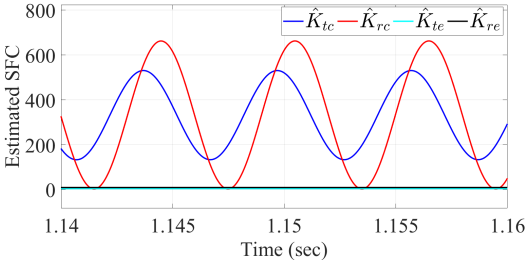

(b) Estimated Cutting Force Coefficients

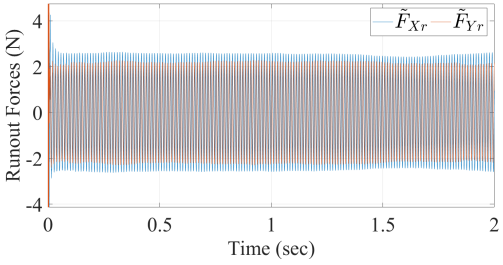

(c) Estimated runout forces in directions X,Y

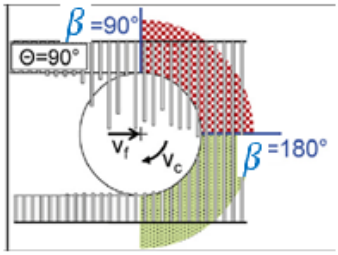

(d) Schematics of tool-workpiece engagement [107].

Figure 4.15: Kalman filter results for $\theta = 90^o$

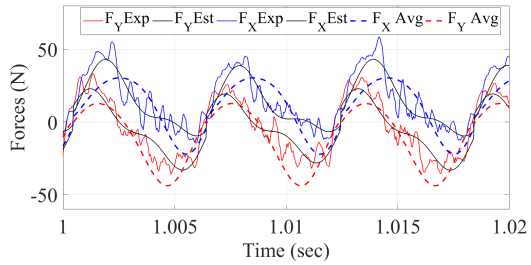

(a) Measured, estimated and average cutting forces

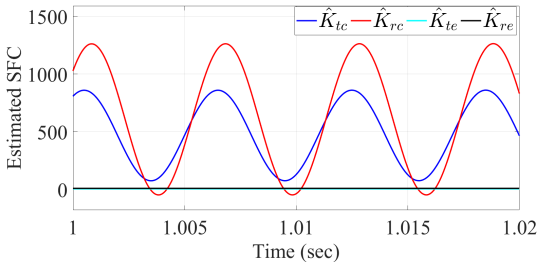

(b) Estimated Cutting Force Coefficients

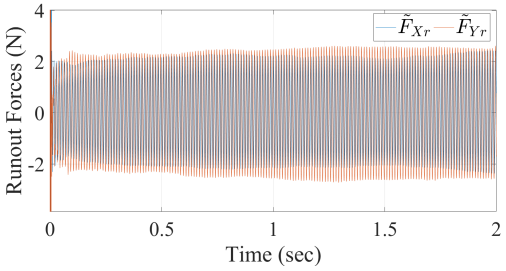

(c) Estimated runout forces in directions X,Y

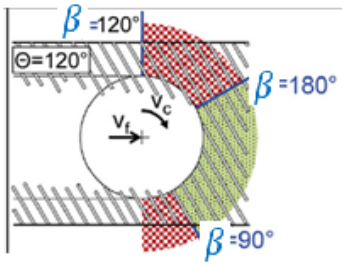

(d) Schematics of tool-workpiece engagement [107].

Figure 4.16: Kalman filter results for $\theta = 120^o$

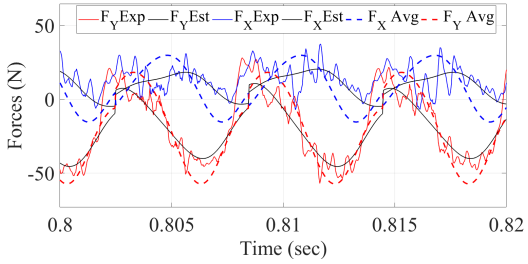

(a) Measured, estimated and average cutting forces

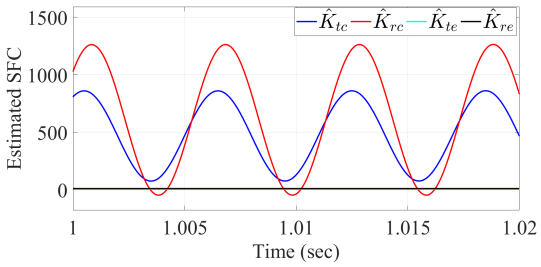

(b) Estimated Cutting Force Coefficients

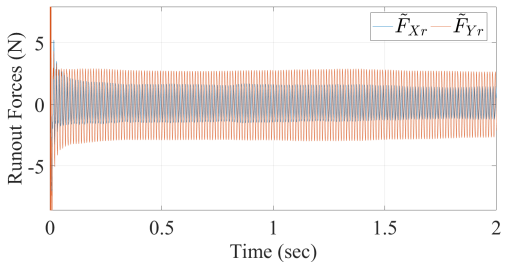

(c) Estimated runout forces in directions X,Y

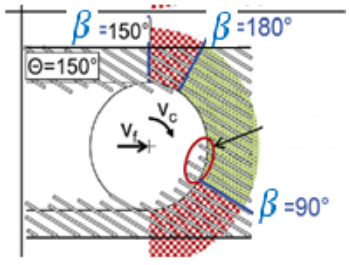

(d) Schematics of tool-workpiece engagement [107].

Figure 4.17: Kalman filter results for $\theta = 150^o$

Table 4.2: Experimental results for variation of cutting force coefficients and cutting forces in milling of CFRP for different fiber orientations

Fiber Orientation		K_t(MPa)	K_r(MPa)	F_X(N)	F_Y(N)
0^o	max	645	639	44	21
	min	-10	-255	-5	-47
30^o	max	971	989	59	19
	min	395	-4	-6	-53
60^o	max	955	855	63	18
	min	142	140	-13	-41
90^o	max	525	662	40	20
	min	133	0	-20	-26
120^o	max	850	1250	59	33
	min	94	-35	-15	-36
150^o	max	655	711	37	27
	min	200	-62	-5	-56

The force coefficients are supposed to have positive values. However, there are some negative values in three cases θ=120°, 150°, and 0°for radial cutting coefficient K_{rc}. At all three fiber orientations, critical zone occurs at the up and down-milled edges where the fibers tend to bend and evade the cutting edge instead of being cut-off in the up and down-milled edges.

It should be noticed that since the mathematical model of cutting process is highly sensitive to the value of some parameters such as ϕ_0, a small deviation of this initial parameter from its actual values will result in big error in estimation of other state space variables.

The best values for matrices [P], [Q], and [R] in the Kalman filter algorithm have been chosen manually. Kalman filter is a model-based observation method. If the mathematical model of system doesn't represent the actual behavior of system, there would be significant biased error in estimation results. In other words, if the mechanistic model used in identification process does not fully represent the actual milling operation, we could not expect an accurate estimation of model parameters.

4.6.5 RLS results

The estimated values for the specific cutting force coefficients $\hat{K}_{tc}$ and $\hat{K}_{rc}$ are plotted in Figure 4.18. The RLS method is used in identification of these parameters for six different fiber orientations are presented in Figure 4.18. The results show a good

consistency between the estimated values in RLS and KF approaches. One case study with fiber orientation θ=30°is chosen to show the L-curve and the convergence of predicted cutting forces in Figure 4.19.

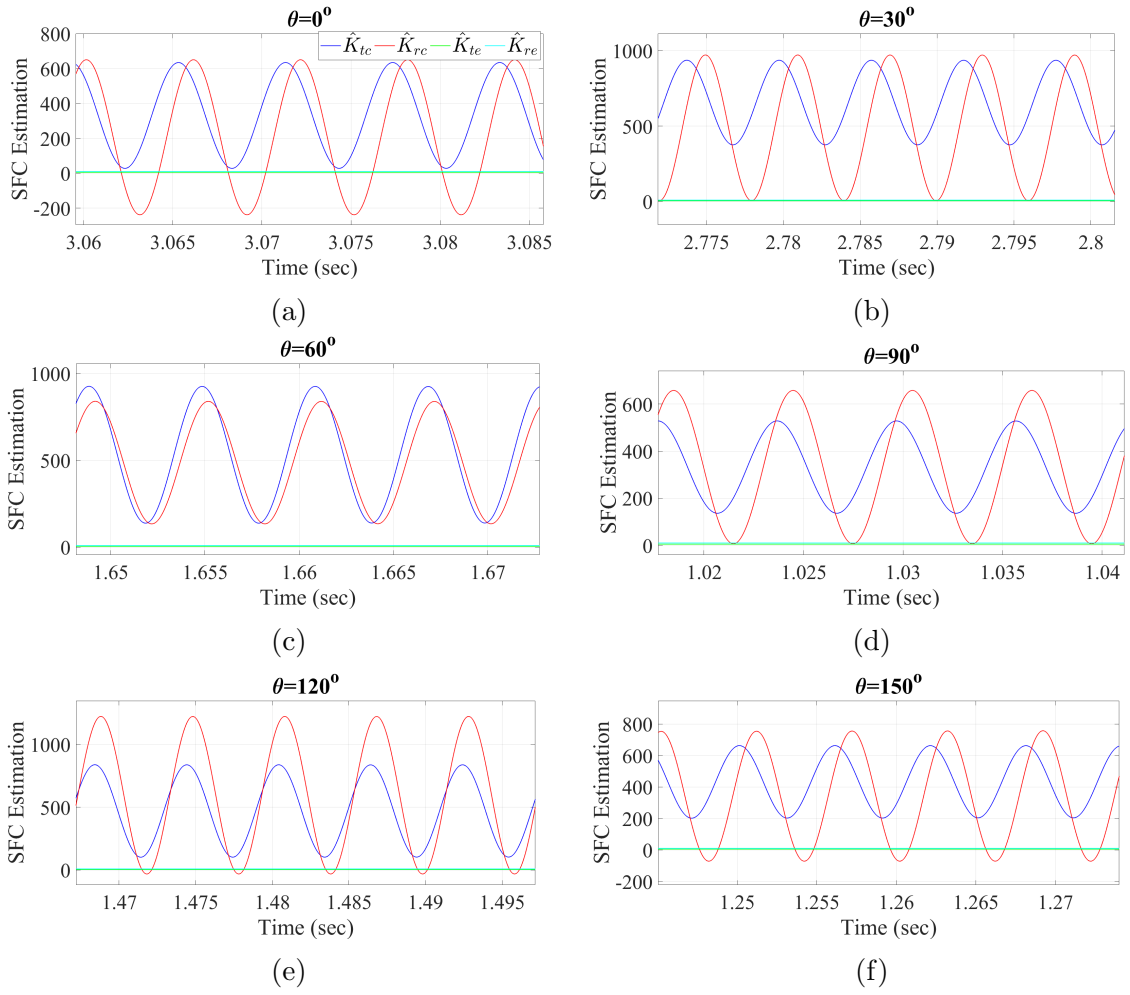

Figure 4.18: Experimental results for estimation of specific cutting force coefficients in six different fiber orientations using RLS method

4.7 Model Prediction for Multi-Directional CFRP Laminates

Multi-directional CFRP consists of a number of unidirectional layers, and the corresponding total cutting forces are calculated by summing the force related to each unidirectional fiber layer.

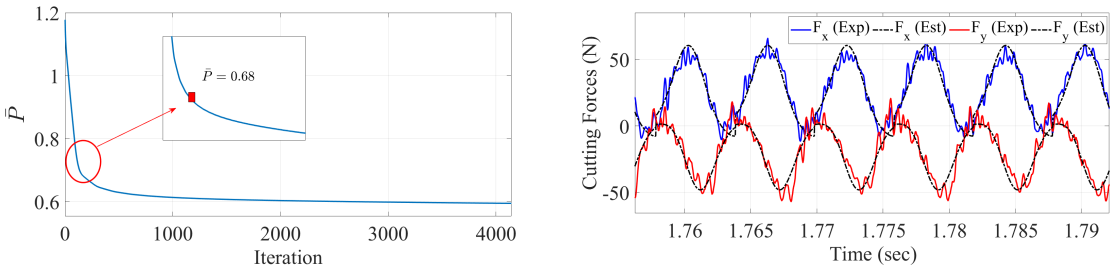

Figure 4.19: (a) Variation of the average of the diagonal elements of error covariance matrix by time steps. Threshold chosen 0.686 for algorithm termination limit.
(b) Comparison between measured and estimated cutting forces during milling of CFRP; feedrate=0.06 mm/teeth, depth of cut=0.8 mm, Spindle speed Ω=5000 RPM, fiber orientation θ=30°, tool feed direction ψ=330°, and full-immersion contact between tool/workpiece.

For the milling of unidirectional composites, estimation of force model parameters was done based on the instantaneous prediction of specific cutting force coefficients (SFC) in previous section. However, the goal in this section is developing mechanical model from UD-CFRP to MD-CFRP, and predicting cutting forces in milling multidirectional composite laminates. A layup sequence of laminates with fiber orientations [150°/60°/150°] was selected randomly in the experimental test, including 3 layers with thickness of 0.8 mm for each layer.

In this section, the mechanistic force model is presented to calculate the overall milling forces for multidirectional CFRP laminates based on superposition principle. Then, the predicted and experimental results of specific force coefficients estimation is compared as well as the cutting force in the figures.

The chip thickness model presented in Equation (4.6) is used here again for the MD-CFRP. It considers the trochoidal trajectory and tool runout parameters. The instantaneous immersion angle of the j^{th} flute, ϕ_j, is assumed to be the same for all of the layers at each time step. In reality, ϕ_j is affected by the helix angle on the cutting tool. Therefore, depending on the depth of cut, we have a different value of ϕ_j for each layer of the composites. However in the current study, because of having only 3 layers of thickness 0.8 mm, we neglect the effect of helix angle as an assumption to simplify the model.

Another assumption to simplify the force model and reduce the complexity of the state space model is neglecting the interlaminar effects between the composites layers.

However the interlaminar effects have been already included in the SFC estimation results.

The tangential and radial cutting forces in multidirectional laminates are considered as summation of cutting forces on each layer. The layer number is denoted by superscript *(i)* in Equation (4.34), where $K_{tc}^{(i)}, K_{rc}^{(i)}, K_{te}^{(i)}$, and $K_{re}^{(i)}$ are the specific force coefficients of the $(i)^{th}$ layer in tangential and radial directions. $a^{(i)}$ is axial depth of cut for the layer *(i)* which could be also referred to the thickness of each layer. Most of the composites parts have layers with the same thickness. Chip thickness is also denoted by $h_{(\phi_j)}$ in the following equation:

$$\begin{aligned} f_{tj} &= \sum_{i=1}^{l} f_{tj}^{(i)} = \sum_{i=1}^{l} (K_{tc}^{(i)}.h_{(\phi_j)}.a^{(i)} + K_{te}^{(i)}.a^{(i)}) \\ f_{rj} &= \sum_{i=1}^{l} f_{rj}^{(i)} = \sum_{i=1}^{l} (K_{rc}^{(i)}.h_{(\phi_j)}.a^{(i)} + K_{re}^{(i)}.a^{(i)}) \end{aligned} \tag{4.34}$$

Specific Force Coefficients are treated as unknown parameters of the force model, So the Kalman filter algorithm will results in estimation of these parameters for the multidirectional composites.

To reduce the complexity of cutting force model, edge force coefficients $K_{te}^{(i)}$ and $K_{re}^{(i)}$ are assumed to be constant numbers which have been already determined from the average force method. This assumption was similarly considered in some other works previously published by R. Voss et al. [107], J Xiao et al. [109], F. Wang et al. [110], Q. An et al. [98].

$$\begin{aligned} K_{tc}^{(i)} &= K_{tc0}^{(i)} + K_{tc1}^{(i)} \sin(2\beta) + K_{tc2}^{(i)} \cos(2\beta) \\ K_{rc}^{(i)} &= K_{rc0}^{(i)} + K_{rc1}^{(i)} \sin(2\beta) + K_{rc2}^{(i)} \cos(2\beta) \\ K_{te}^{(i)} &= K_{te0}^{(i)} \\ K_{re}^{(i)} &= K_{re0}^{(i)} \end{aligned} \tag{4.35}$$

By using Equation (4.4) ($\beta = \phi_j + \theta$), and then, substituting Equation (4.35) in the main force model (Equation (4.34)) and considering the tool rotation angle, ϕ_j for each flute j in the heaviside function $g_{(\phi_j)}$, refer to Equation (4.9), we have the

following form of equation:

$$
\begin{aligned}
f_t &= \sum_{j=1}^{N} g_{(\phi_j)} \sum_{i=1}^{l} \Big[\Big(K_{tc0}^{(i)} + K_{tc1}^{(i)} \sin 2(\phi_j + \theta^{(i)}) + K_{tc2}^{(i)} \cos 2(\phi_j + \theta^{(i)}) \Big) . h_{(\phi_j)} . a^{(i)} + K_{te}^{(i)} . a^{(i)} \Big] \\
f_r &= \sum_{j=1}^{N} g_{(\phi_j)} \sum_{i=1}^{l} \Big[\Big(K_{rc0}^{(i)} + K_{rc1}^{(i)} \sin 2(\phi_j + \theta^{(i)}) + K_{rc2}^{(i)} \cos 2(\phi_j + \theta^{(i)}) \Big) . h_{(\phi_j)} . a^{(i)} + K_{re}^{(i)} . a^{(i)} \Big]
\end{aligned}
\tag{4.36}
$$

Using trigonometric identities formulas, $\big(\sin(a+b) = \sin a . \cos b + \sin b . \cos a \big)$ and $\big(\cos(a+b) = \cos a . \cos b - \sin a . \sin b \big)$, we can break the terms *sin* and *cos* down into separate components. Therefore, Equation (4.36) can be rewritten in the following form:

$$
\begin{aligned}
f_t = \sum_{j=1}^{N} g_{(\phi_j)} \sum_{i=1}^{l} \Big[\Big(& K_{tc0}^{(i)} + K_{tc1}^{(i)} \big(\sin 2\phi_j . \cos 2\theta^{(i)} + \sin 2\theta^{(i)} . \cos 2\phi_j \big) + \\
& + K_{tc2}^{(i)} \big(\cos 2\phi_j . \cos 2\theta^{(i)} - \sin 2\theta^{(i)} . \sin 2\phi_j \big) \Big) . h_{(\phi_j)} . a^{(i)} + K_{te}^{(i)} . a^{(i)} \Big] \\
f_r = \sum_{j=1}^{N} g_{(\phi_j)} \sum_{i=1}^{l} \Big[\Big(& K_{rc0}^{(i)} + K_{rc1}^{(i)} \big(\sin 2\phi_j . \cos 2\theta^{(i)} + \sin 2\theta^{(i)} . \cos 2\phi_j \big) + \\
& + K_{rc2}^{(i)} \big(\cos 2\phi_j . \cos 2\theta^{(i)} - \sin 2\theta^{(i)} . \sin 2\phi_j \big) \Big) . h_{(\phi_j)} . a^{(i)} + K_{re}^{(i)} . a^{(i)} \Big]
\end{aligned}
\tag{4.37}
$$

One more simplification step and rearranging the terms in Equation (4.37) will result in cutting forces as a function of equivalent specific force coefficients shown in Equation (4.38):

$$
\begin{aligned}
f_t &= \sum_{j=1}^{N} g_{(\phi_j)} . a^{(eq)} \Big[\big(K_{tc0}^{(eq)} + K_{tc1}^{(eq)} \sin 2\phi_j + K_{tc2}^{(eq)} \cos 2\phi_j \big) . h_{(\phi_j)} + K_{te}^{(eq)} \Big] \\
f_r &= \sum_{j=1}^{N} g_{(\phi_j)} . a^{(eq)} \Big[\big(K_{rc0}^{(eq)} + K_{rc1}^{(eq)} \sin 2\phi_j + K_{rc2}^{(eq)} \cos 2\phi_j \big) . h_{(\phi_j)} + K_{re}^{(eq)} \Big]
\end{aligned}
\tag{4.38}
$$

where the equivalent coefficients of the mechanistic force model could be extracted explicitly as functions of fiber orientation angle of each layer, $\theta^{(i)}$, and the characteristic properties of layers. Equation (4.39) shows these model parameters, and how properties of each layer *(i)* and plies layup influence the overall SFC in milling of MD-CFRP composites.

$$
\begin{aligned}
a^{(eq)} &= \sum_{i=1}^{l}\left[a^{(i)}\right]; \qquad K_{tc0}^{(eq)} = \sum_{i=1}^{l}\left(K_{tc0}^{(i)}\right); \qquad K_{rc0}^{(eq)} = \sum_{i=1}^{l}\left(K_{rc0}^{(i)}\right) \\
K_{tc1}^{(eq)} &= \sum_{i=1}^{l}\left(K_{tc1}^{(i)}\cos\left(2\theta^{(i)}\right) - K_{tc2}^{(i)}\sin\left(2\theta^{(i)}\right)\right) \\
K_{tc2}^{(eq)} &= \sum_{i=1}^{l}\left(K_{tc1}^{(i)}\sin\left(2\theta^{(i)}\right) + K_{tc2}^{(i)}\cos\left(2\theta^{(i)}\right)\right) \\
K_{rc1}^{(eq)} &= \sum_{i=1}^{l}\left(K_{rc1}^{(i)}\cos\left(2\theta^{(i)}\right) - K_{rc2}^{(i)}\sin\left(2\theta^{(i)}\right)\right) \\
K_{rc2}^{(eq)} &= \sum_{i=1}^{l}\left(K_{rc1}^{(i)}\sin\left(2\theta^{(i)}\right) + K_{rc2}^{(i)}\cos\left(2\theta^{(i)}\right)\right)
\end{aligned}
\tag{4.39}
$$

In order to determine the force model parameters in milling of MD-CFRPs, it is necessary to know the value of the equivalent force coefficients $K_{tc0}^{(eq)}$, $K_{tc1}^{(eq)}$, $K_{tc2}^{(eq)}$, $K_{rc0}^{(eq)}$, $K_{rc1}^{(eq)}$, $K_{rc2}^{(eq)}$, $K_{te}^{(eq)}$, and $K_{re}^{(eq)}$. These coefficients could be estimated numerically or experimentally by using the Kalman filter observer algorithm. However, each one of these equivalent coefficients has been shown as a trigonometric combination of unidirectional layers force coefficients and their corresponding fiber orientations angle $\theta^{(i)}$, as shown in Equation (4.39).

We can rewrite the cutting force model by mapping the cutting forces from the tangential and radial directions to the feed and normal directions using transformation matrix presented in the following equation:

$$
\left\{ \begin{array}{c} F_X \\ F_Y \end{array} \right\} = \sum_{j=1}^{N} g(\phi_j) T_t^X \left\{ \begin{array}{c} f_t \\ f_r \end{array} \right\}; \qquad T_t^X = \left[\begin{array}{cc} \cos(\phi_j) & \sin(\phi_j) \\ -\sin(\phi_j) & \cos(\phi_j) \end{array} \right] \tag{4.40}
$$

Now, by substituting the equivalent coefficients, Equation (4.39), into Equation (4.34), we can rearrange the feed and normal forces, F_X and F_Y, in a linear matrix form in MD laminate composites. Runout forces are also considered as unknown

parameters in the modeling:

$$\left\{ \begin{array}{c} F_X \\ F_Y \end{array} \right\} = \sum_{j=1}^{N} g(\phi_j).a. \left[\begin{array}{cc} h_{(\phi_j)} \cos\phi_j & -h_{(\phi_j)} \sin\phi_j \\ h_{(\phi_j)} \sin 2\phi_j \cos\phi_j & -h_{(\phi_j)} \sin 2\phi_j \sin\phi_j \\ h_{(\phi_j)} \cos 2\phi_j \cos\phi_j & -h_{(\phi_j)} \cos 2\phi_j \sin\phi_j \\ h_{(\phi_j)} \sin\phi_j & h_{(\phi_j)} \cos\phi_j \\ h_{(\phi_j)} \sin 2\phi_j \sin\phi_j & h_{(\phi_j)} \sin 2\phi_j \cos\phi_j \\ h_{(\phi_j)} \cos 2\phi_j \sin\phi_j & h_{(\phi_j)} \cos 2\phi_j \cos\phi_j \\ \cos\phi_j & -\sin\phi_j \\ \sin\phi_j & \cos\phi_j \\ 1 & 0 \\ 0 & 0 \\ 0 & 1 \\ 0 & 0 \end{array} \right]^T \left[\begin{array}{c} K_{tc0}^{(eq)} \\ K_{tc1}^{(eq)} \\ K_{tc2}^{(eq)} \\ K_{rc0}^{(eq)} \\ K_{rc1}^{(eq)} \\ K_{rc2}^{(eq)} \\ K_{te}^{(eq)} \\ K_{re}^{(eq)} \\ F_{Xr} \\ \dot{F}_{Xr} \\ F_{Yr} \\ \dot{F}_{Yr} \end{array} \right] \tag{4.41}$$

4.7.1 Simulation results for MD-CFRP

In this section, firstly we show numerical simulation results for a layup sequence of three laminates with different fiber orientation formations [0°/0°/0°], [90°/90°/90°], and [150°/60°/150°], which were selected arbitrarily to show the cutting forces in feed and normal directions, X and Y.

The cutting force coefficient (SFC) are as same as Equation (4.32) except the edge force coefficients which are considered as constant values. The other cutting conditions are $c = 0.06mm/tooth$, $\Omega = 5000rev/min$, axial depth of cut for each layer $a = 0.8mm$, $\Delta t = 0.039ms$, and full immersion engagement. Figure 4.20 shows the cutting forces for these three different formation of laminates generated by using the Equation (4.41). Although layup [0°/0°/0°] and [90°/90°/90°] could be considered as unidirectional laminates with depth of $3 \times a$, the resulting cutting forces are not the same due to effect of fiber cutting angle β for each formation.

In order to investigate the performance of Kalman filter on the estimation of SFC in milling MD-CFRP, the layup [150°/60°/150°] is chosen for the numerical analysis. Runout effect and noise on cutting forces have been also considered in the model. The initial tool rotation angle is selected $\phi_0 = 0°$. Figures 4.21(a-b) shows the equivalent SFC, presented in Equation (4.41). part (c) and (d) also show the estimated runout forces and estimated cutting forces, respectively.

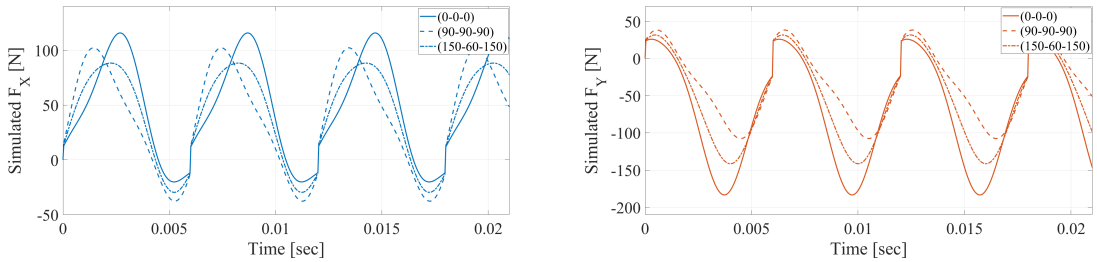

(a) (b)

Figure 4.20: Numerical simulation of cutting forces in milling multi-directional(MD) laminates for three different formation of fiber orientation angle θ including [0°/0°/0°], [90°/90°/90°], and [150°/60°/150°] (a)F_X; (b)F_Y;

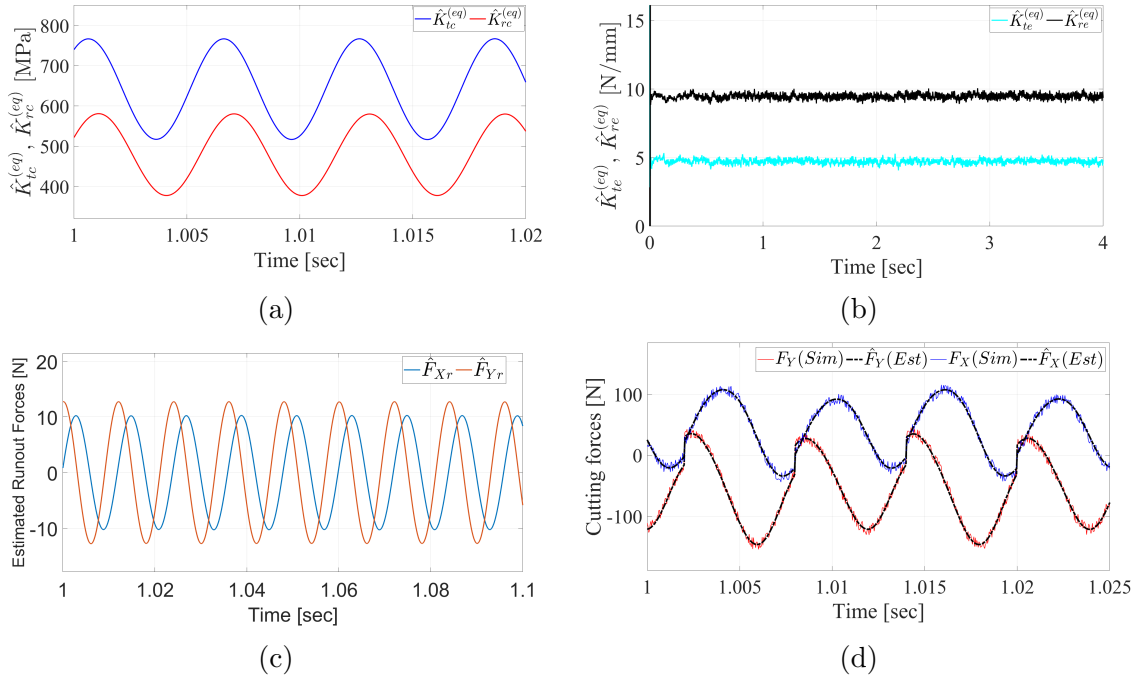

(a) (b) (c) (d)

Figure 4.21: Numerical simulation results for milling Multi-directional laminates [150°/60°/150°] using Kalman filter method. (a) Cutting force coefficients estimation; (b) Edge force coefficients estimation; (c) Runout forces estimation; (d) Simulated and estimated cutting forces F_X, F_Y.

Equation 4.39 is an important equation which gives us the ability to identify the specific force coefficients $K_{tc0}^{(i)}$, $K_{tc1}^{(i)}$, $K_{tc2}^{(i)}$, $K_{rc0}^{(i)}$, $K_{rc1}^{(i)}$, $K_{rc2}^{(i)}$, $K_{te}^{(i)}$, and $K_{re}^{(i)}$ from the estimated equivalent force coefficients $K_{tc0}^{(eq)}$, $K_{tc1}^{(eq)}, \cdots$. In most of the applications, the properties of fibers and matrix such as strength and density of fibers, matrix material, shearing stresses in layers are the same, so we can assume that $K_{tc0}^{(1)} =$

$K_{tc0}^{(2)} = \cdots = K_{tc0}^{(i)}$. Therefore, the Equation (4.39) will change into a system with the same number of equations and unknowns which has a single unique solution for SFC. The numerical simulation results also shows that the equations presented in this section are applicable for any arbitrary layup of composites.

4.7.2 Experimental study on milling MD-CFRP

The presented Kalman filter method in section 4.4.2 is applied here to estimate the SFCs and runout forces contribution to the experimental measured forces. The initial immersion angle is estimated $\phi_0 = 40°$from the prior analysis discussed on previous section 4.4.1. It is identified based on the minimization of the error using least squares estimation(LSE) method discussed previously. In Figure 4.22a, the minimum and

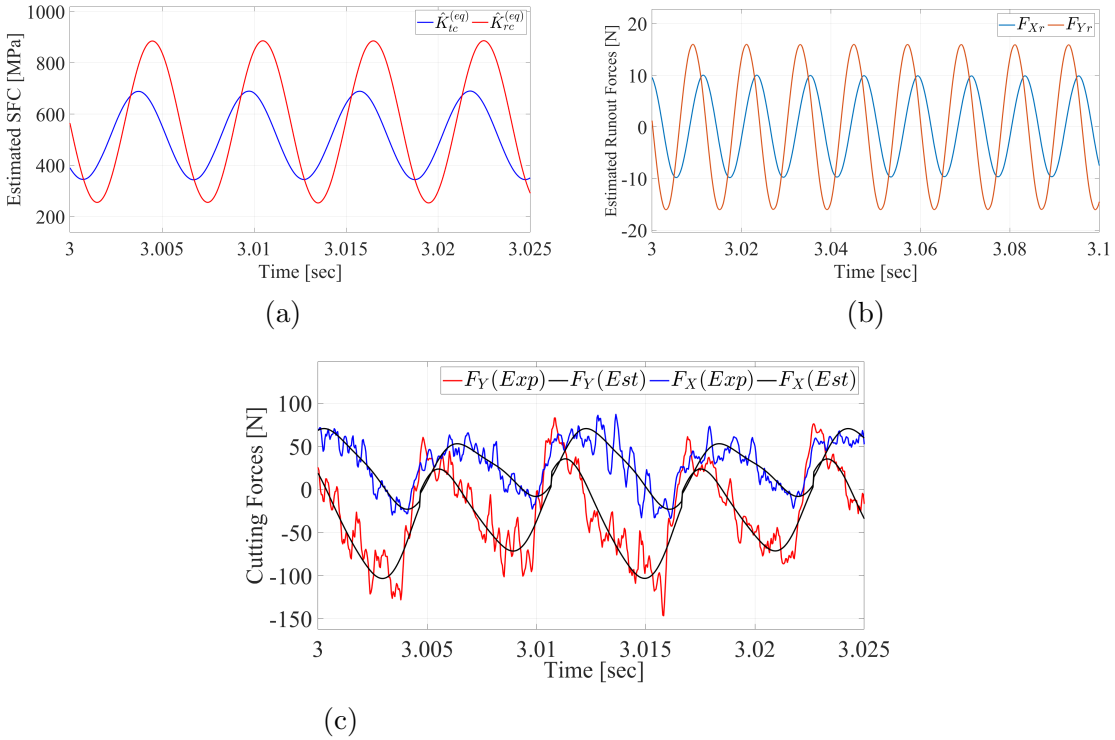

Figure 4.22: Experimental Analysis results results for milling Multi-directional laminates [150°/60°/150°] using Kalman filter method. (a) Cutting force coefficients estimation; (b) Runout forces estimation; (c) Comparison of measured cutting forces and the forces estimated using Kalman filter method.

maximum values for the equivalent coefficient $\hat{K}_{tc}^{(eq)}$ converge to 669 and 351 [MPa], respectively. These values are 815 and 273 [MPa] for $\hat{K}_{rc}^{(eq)}$. Figure 4.22b depicts the

estimated runout forces. The forces estimated by the KF algorithm are compared against the measured ones in Figure 4.22c.

The estimated cutting forces appear to be reasonably accurate. The relative errors between the predicted and experimental value at the feedrate $c = 0.05mm/tooth/rev$ are less than 10% which is within a reasonable range for experiments. Three layers are being cut with the total 2.4 mm depth of cut and with spindle rotational speed of $\Omega = 5000$ [RPM].

4.8 Comparison of Online Identification Methods

In Chapter 4, all of the three methods EKF, KF, and RLS were shown to be capable of identifying the SFC in full-immersion operations in numerical simulations. The predicted cutting forces follows the measured ones with an acceptable deviation from the actual values. However, due to the uncertainty in the used mechanistic force model and unmodelled parameters, the EKF does not converge for the estimation of the state variables in the experimental studies.

The runout parameters need to be measured accurately and modelled properly in the RLS algorithm in order to increase the convergence accuracy of identified specific force coefficients, while in KF and EKF methods these runout forces can be considered as additional state variables and being identified in the algorithm. The advantage of KF and EKF methods over RLS is in their capability to identify the SFC without a prior knowledge of the runout parameters. When an accurate measurement of the runout parameters is available, the application of RLS is more advantageous, because information about the process and measurement noise is not required. One important advantage of the EKF over RLS and KF methods is that the initial immersion angle of the tool was considered as an additional state variable. Therefore, it does not require the determination of initial immersion angle in the first stage of identification.

According to part (a) in Figures 4.12 to 4.17, the overall performance of the presented online methods in prediction of the cutting forces in better than the average-force method presented in Chapter 2. This higher accuracy is because the SFC resulting from the average method are identified for a range of feedrate values, whereas in the online presented methods, they are adaptively calibrated for the specific feedrate that is being used in the operation. The identified SFC from both RLS and KF methods are similar to each other with slight differences due to different number of state variables used in each method.

The convergence rate of the mentioned methods are also different. Because EKF linearizes the nonlinear system at each time-step of the algorithm, it converges slower than KF while the RLS algorithm converges the fastest as it involves a fewer number of variables.

The computational complexity of the KF increases when the number of estimated state variables or dimensionality of the measurement vector increases. Because EKF linearizes the nonlinear system at each time-step of the algorithm, it converges slower than KF. The RLS algorithm converges the fastest as it involves a fewer number of variables. The number of state variables are reduced in the CFRP milling force model by considering the edge force coefficients as constant numbers instead of periodic functions with multiple coefficients. This decision reduces the complexity of the model as well as the computational loads. The computation time of algorithms can also be reduced using parallel computing. The matrix operations can be effectively parallelized in the linear algebra library that handles the matrix operations. Thus, we do not consider parallelization in this project.

4.9 Conclusions

Two recursive identification methods, including Kalman filter (KF) and Recursive Least Squares (RLS), were applied to estimate the parameters of the mechanistic force model in the milling of Unidirectional CFRP composites. The RLS method is more straightforward to implement, but it requires prior knowledge of tool runout parameters.

The KF method does not need knowledge of runout parameters, but designing the filter requires tuning measurement and process noise covariance coefficients. The performances of the presented methods were validated by numerical simulations and experimental studies. Both methods were shown to be accurate in predicting the machining forces and converging to similar force models for the applications of process monitoring, control, and optimization.

Chapter 5

Application of Online Identification Methods in Future Works

In this chapter of the thesis, the applications of the model identification methods, presented in Chapters 3 and 4 are studied. It is shown that how implementation of these methods could enhance the composite material machining process.

5.1 Virtual Model Assisted Adaptive Control in Milling Process

Force and Specific Cutting Energy (SCE) control are known as an indirect means of controlling delamination. The extent of delamination is correlated with the level of cutting forces. Also, SCE is a measure of machinability of the material and therefore could be correlated with delamination. The correlation between forces and SCE and the resulting delamination has been already investigated experimentally in the literature. For example, the influence of fiber orientation, tool geometry, and process parameters has been studied on material surface quality during CFRP milling, presented by R. Voss et al. [107]. However, there is a gap in the knowledge regarding online control of delamination during the CFRP milling process.

In this section, two algorithm are proposed in Figure 5.1 and Figure 5.2, which illustrate the general flowchart of the proposed force and SCE control algorithms. In both algorithms, feedrate is used as the control variable.

As shown in Figure 5.1 and Figure 5.2, both of the control systems consist of three main components: 1) milling process model shown in red block, 2) virtual

model shown in blue block, and 3) adaptive control algorithm shown as black block. The adaptive control algorithm (black block) is readily available in metal cutting literature [111, 42], but there are fundamental differences between milling process model (red block) and virtual model of CFRP and metal cutting (blue block). The presented results in previous chapters can be directly used in development of these two components in this research.

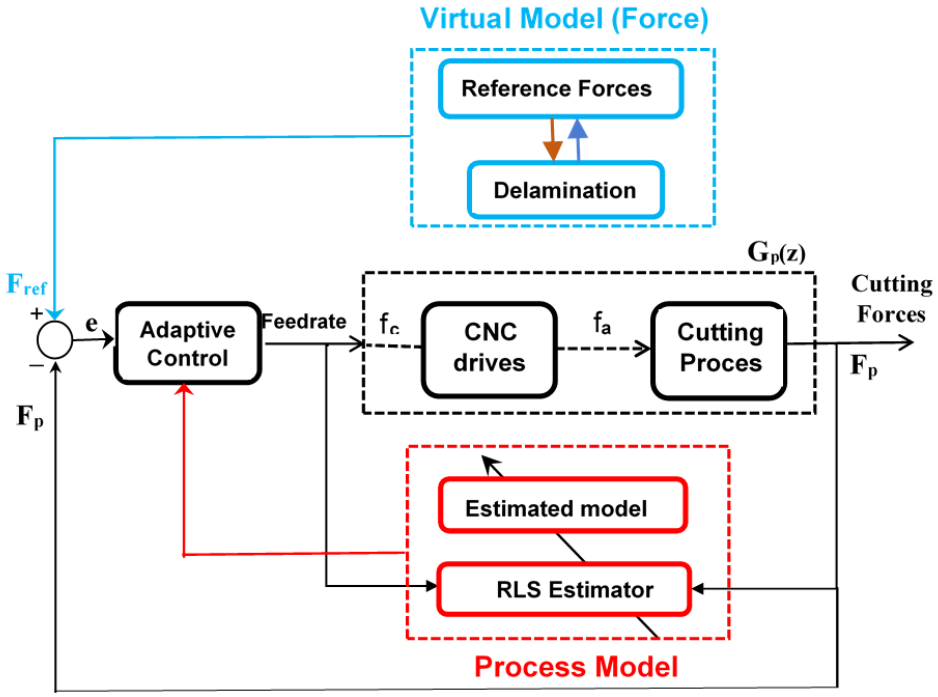

Figure 5.1: schematic block diagram of the adaptive force control system integrated by virtual system

The blue block in Figure 5.1 and Figure 5.2 is Virtual Machining System (VMS). This system has different functionalities in force control (Figure 5.1), and energy control (Figure 5.2).

In Force control, the VMS provides the reference force at every cutter location along the toolpath. The maximum cutting force that will guarantee acceptable level of delamination might be different at various cutter locations based on fibre orientation and cutter/workpiece engagement conditions. The reference force at each cutter location will be determined by using offline simulations of the process in the VMS; The mechanistic model with parameters that depend on fibre cutting angle in **Chapter 2** can be used in VMS. The model parameters (i.e. specific force coefficients) are identified based on the offline regression of the milling forces. The computed reference

force values are provided to the control system during the machining operation.

In SCE control, the VMS has an additional functionality. The reference SCE at each cutter location will be determined using offline simulations of the process in the VMS as well, and in addition to that, the VMS will estimate the SCE during the process by combining the online force measurements and the cutter/workpiece engagement geometry that is computed using offline simulations in **Chapter 2**. The estimated SCE during the process can be calculated by using recursive identification methods (i.e. recursive least square (RLS) and Kalman filter (KF)), presented in **Chapters 3 and 4**.

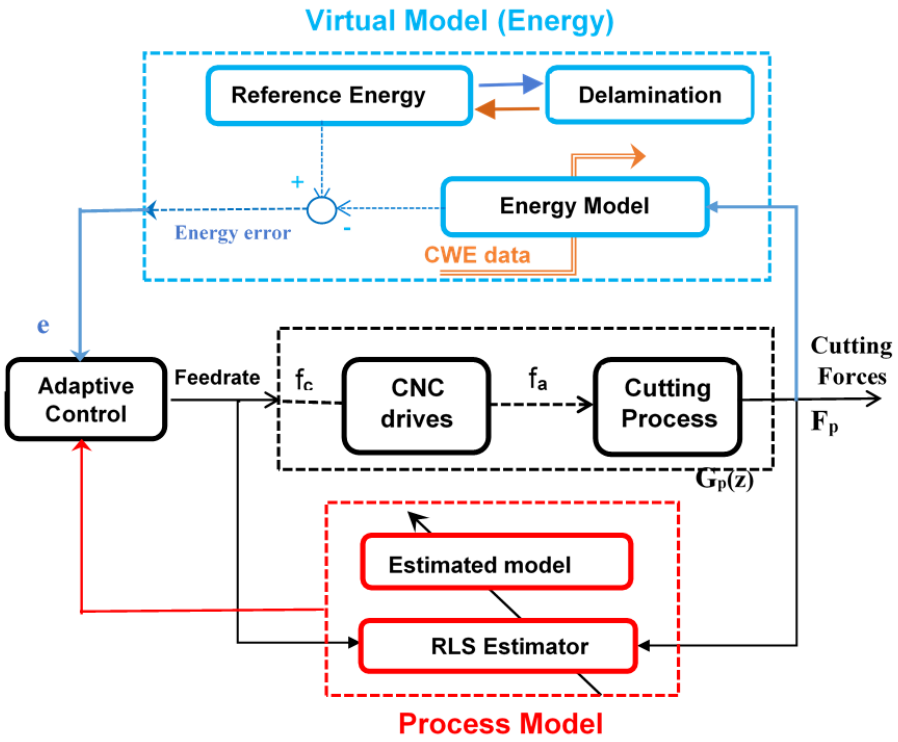

Figure 5.2: schematic block diagram of the adaptive energy control integrated by virtual system

The red block in Figure 5.1 and Figure 5.2 show the milling process model which correlates the commanded feedrate to the resulting forces. The composition of this block is identical in both force and SCE control algorithms. The transfer function in this block combines the dynamics of the feed drive and the milling process. While modeling the feed drive dynamics is readily available from metal machining literature, the dynamics of CFRP milling process is fundamentally different than milling metallic materials. The mechanics of chip formation in CFRP milling depends on fibre cutting

angle and the length of the fibre that is being cut, and these parameters change periodically as the tool rotates.

Since the estimated model parameters identified by offline approaches lose accuracy when tool wear increases or cutting conditions change during the process, online identification methods are being used in the process model (red block) to adaptively recalibrate the model parameters during the process. The estimated model has been proposed and discussed in **Chapter 3** for the metallic materials, and **Chapter 4** for the CFRP composites.

The Adaptive control system, shown in black block, will be designed to keep the peak forces and energy at a desired level by manipulating the feedrate in order to avoid delamination and get a better surface finish and machinability. During the end milling operation, cutting forces and SCE vary due to the variation in fibre cutting angle and cutting parameters.

In Figure 5.1, after measurement of the cutting forces and comparing with the reference forces, the resulting error is adjusted by the adaptively controlling the feedrate command to CNC machine. In Figure 5.2, if the level of computed energy exceeds the reference energy level in virtual model, the adaptive controller can identify these changes and send the corrective feedrate signal to CNC machine to keep the cutting forces in a desired level.

A Recursive Least Squares (RLS) method can be used to estimate the parameters of the adaptive controller based on the minimization of error between the command feed and the feed estimated from RLS algorithm. The fundamentals of RLS has been explained in **Chapter 3**.

5.2 Tool Condition Monitoring

Another application of the online identification methods, presented in **Chapter 3 and 4**, is tool condition monitoring. Online monitoring of machining forces is an effective method for tool condition monitoring; however, in addition to tool wear and breakage, machining forces are also affected by changes in cutter-workpiece engagement and machining parameters. Therefore, tool condition monitoring using the force signal requires a complex use of Virtual Machining Systems or signal processing methods to remove the effect of cutter-workpiece engagement and machining parameters.

Referring to Chapter 4, Specific Force Coefficients, on the other hand, are mainly affected by the mechanics of chip formation only. As a result, SFC provide more

sensitive measures for tool condition monitoring. For instance, Lin and Yang [85], and later, Choudhury and Rath [86] used the relationship between flank wear and the average SFC to estimate the extent of tool wear in milling processes. In their work, SFC were estimated by offline processing of the average cutting forces.

Therefore, the recursive methods RLS and KF presented in Chapter 4 as online schemes to monitor SFC led to the successful monitoring of tool wear during the process since other studies verify that SCF are strongly affected by tool wear. As a result, in addition to their application in mechanistic force models, SFC can be used for tool condition monitoring as well.

Chapter 6

Conclusion and Contribution

This thesis describes (1) the development of mechanistic force model for modeling and identification of cutting forces in milling of Carbon Fibre Reinforced Polymers, (2) online approaches for Identification of force models parameters in machining of isotropic metallic materials, (3) Using recursive least squares and kalman filter methods in parameter identification of force models during milling CFRP composites, and (4) innovative applications of the online methods in virtual machining system assisted adaptive control of CFRP milling process, each of which is described in Chapter 2 to 5 in details. In the following section, a summary of key findings and future works for each component are presented.

6.1 Modeling and Identification of Cutting Forces in Milling of CFRPs

6.1.1 Summary of findings

- A mechanistic CFRP milling force model that considers the variation of the chip formation mechanics in various fibre cutting angles was presented.
- A new method was presented to identify the periodic cutting force coefficients based on the average milling forces measured during milling UD composite layers.
- Numerical modeling and simulation of machining of multi-directional CFRPs.

- Unavoidable characteristics of CFRP milling processes such as excessive tool wear, fibre pull-out, and fibre peeling affect the accuracy of the presented model.

6.1.2 Recommendations for future works

- Analyzing the effect of other cutting process parameters such as tool wearing factor, tool rotation speed, or axial depth of cut in the mechanics of chip formation will results in more accurate force model.
- Studying the mechanics of delamination during CFRP milling processes and developing analytical models that relate milling forces to the resulting delamination.
- Studying the linkage between the variation of the cutting force coefficients and the physics of chip formation at different fibre cutting angles may provide a better understanding of the mechanics of the process.

6.2 Online Identification of Mechanistic Milling Force Models in Milling Metallic Materials

6.2.1 Summary of findings

- Three online identification methods were presented to monitor the evolution of Specific Force Coefficients (SFC) of linear milling force models for Aluminum cutting
- Recursive Least Squares(RLS), Kalman Filter(KF), and Extended Kalman Filter (EKF) methods were shown to be capable of identifying SFC recursively at every discrete time step during the milling process.
- Considering the effect of tool runout parameters in the estimation of SFC.

6.2.2 Recommendations for future works

- Extending the identification methods and simulation of cutting forces to other machining processes such as drilling, turning, etc.

- Developing the online methods for more complicated toolpath trajectories rather than only slot millings.
- Real-time implementation of the proposed methods for a more effective process monitoring during milling operations in order to use for in-situ calibration of Virtual Machining Systems when they are used as the digital twin of the machining process.

6.3 Recursive Identification of Cutting Force Model Parameters in Milling of CFRPs

6.3.1 Summary of findings

- Two recursive identification methods, including Kalman Filter (KF) and Recursive Least Squares (RLS), were applied to estimate the parameters of the mechanistic force model in the milling of CFRP composites.
- Both Uni-directional (UD) and Multi-directional composite layups were analysed in numerical simulation and experimental studies.
- RLS method is more straightforward to implement, but it requires prior knowledge of tool runout parameters.
- KF method does not need knowledge of runout parameters, but designing the filter requires tuning measurement and process noise covariance coefficients.
- The mechanistic milling force model of UD laminates was developed for using in MD laminates consisting multiple layers of plies.
- Both RLS and KF methods were shown to be accurate in predicting the machining forces and converging to similar force models for the applications of process monitoring, control, and optimization.

6.3.2 Recommendations for future works

- Applying adaptive control of cutting forces on the CNC machine to prevent machining induced damages. due to the application of tools with unconventional geometries, materials with arbitrary layups, and accelerated tool wear in CFRP

milling, implementing adaptive control of force and energy could be an effective method to prevent delamaination.

6.4 Contributions

1. Numerical simulations are presented to prove the accuracy and validation of the RLS, and Kalman filter approaches in milling of CFRP composites.

2. In order to consider the effect of tool runout and measurement noises on the results, two different sets of numerical simulations are determined, one without considering tool runout and noises, and the other analysis considering the effect of runout and noises. The results for numerical simulation show consistency between true values and estimated values of SFC using RLS and KF online identification methods.

3. Experimental analysis is conducted for online estimation of SFCs based on actual cutting forces measured by dynamometer on the CNC table machine.

4. Range and accuracy of experimental results using online RLS and Kalman filter methods are acceptable and in some cases more reasonable than offline identification approaches such as average force method.

5. Using Kalman filter also gives the opportunity of identifying runout forces during the milling process which adds to advantages of proposed online methods.

6. The mechanistic force model was also developed for the multi-layer composites and the experimental analysis was implemented for the identification of the SFCs, and the cutting forces during milling of multi-directional laminate composites which shows a successful extension of the mechanistic force model from the uni-directional to multi-directional composites while there is good agreement between the experimental and simulation results.

Bibliography

[1] Jamal Y Sheikh-Ahmad. *Machining of polymer composites*, volume 387355391. Springer, 2009.

[2] Alan Arnold Griffith. The phenomena of rupture and flow in solids. *Philosophical Transactions of the Royal Society of London. Series A, Containing Papers of a Mathematical or Physical Character*, 221:163–198, 1921.

[3] DeFu Liu, YongJun Tang, and WL Cong. A review of mechanical drilling for composite laminates. *Composite structures*, 94(4):1265–1279, 2012.

[4] Suresh G Advani and E Murat Sozer. *Process modeling in composites manufacturing*. CRC press, 2002.

[5] Tomas Astrom. *Manufacturing of polymer composites*. Routledge, 2018.

[6] Demeng Che, Ishan Saxena, Peidong Han, Ping Guo, and Kornel F Ehmann. Machining of carbon fiber reinforced plastics/polymers: a literature review. *Journal of Manufacturing Science and Engineering*, 136(3), 2014.

[7] Roberto Teti. Machining of composite materials. *CIRP Annals*, 51(2):611–634, 2002.

[8] Shan Luo, Reza Bayesteh, Zuomin Dong, and Martin BG Jun. 3-axis milling algorithm development for carbon fiber reinforced polymer (CFRP) composites. *Journal of the Korean Society for Precision Engineering*, 33(6):447–452, 2016.

[9] Devi Kalla, Jamal Sheikh-Ahmad, and Janet Twomey. Prediction of cutting forces in helical end milling fiber reinforced polymers. *International Journal of Machine Tools and Manufacture*, 50(10):882–891, 2010.

[10] Yiğit Karpat, Onur Bahtiyar, and Burak Değer. Milling force modelling of multidirectional carbon fiber reinforced polymer laminates. *Procedia Cirp*, 1:460–465, 2012.

[11] Berend Denkena, David Boehnke, and Jan H. Dege. Helical milling of cfrp–titanium layer compounds. *CIRP Journal of manufacturing Science and Technology*, 1(2):64–69, 2008.

[12] Nor Khairusshima Mk, Che Hassan Ch, Nurul Amin Akm, and Nurul Amin AKM. Tool wear and surface roughness on milling carbon fiber-reinforced plastic using chilled air. *Journal of Asian Scientific Research*, 2(11):593–598, 2012.

[13] Antonio Argüelles, J. Viña, Alfonso Fernandez Canteli, and Jorge Bonhomme. Influence of resin type on the delamination behavior of carbon fiber reinforced composites under mode-ii loading. *International Journal of Damage Mechanics*, 20(7):963–978, 2011.

[14] Kevin Colligan and Mamidala Ramulu. Delamination in surface plies of graphite/epoxy caused by the edge trimming process. *Processing and Manufacturing of composite materials*, 112:113–125, 1991.

[15] SKSR Basavarajappa, G Chandramohan, KV Narasimha Rao, R Radhakrishanan, and V Krishnaraj. Turning of particulate metal matrix composites—review and discussion. *Proceedings of the institution of mechanical engineers, Part B: Journal of engineering manufacture*, 220(7):1189–1204, 2006.

[16] DH Wang, Mamidala Ramulu, and Dwayne D. Arola. Orthogonal cutting mechanisms of graphite/epoxy composite. part ii: multi-directional laminate. *International Journal of Machine Tools and Manufacture*, 35(12):1639–1648, 1995.

[17] DH Wang, Mamidala Ramulu, and Dwayne D. Arola. Orthogonal cutting mechanisms of graphite/epoxy composite. part i: unidirectional laminate. *International Journal of Machine Tools and Manufacture*, 35(12):1623–1638, 1995.

[18] Meltem Altin Karataş and Hasan Gökkaya. A review on machinability of carbon fiber reinforced polymer (cfrp) and glass fiber reinforced polymer (gfrp) composite materials. *Defence Technology*, 14(4):318–326, 2018.

[19] G Santhanakrishnan, Ramalingam Krishnamurthy, and Santa Kumar Malhotra. Machinability characteristics of fibre reinforced plastics composites. *Journal of Mechanical Working Technology*, 17:195–204, 1988.

[20] Mihai-Bogdan Lazar and Paul Xirouchakis. Experimental analysis of drilling fiber reinforced composites. *International Journal of Machine Tools and Manufacture*, 51(12):937–946, 2011.

[21] Gordon C. Everstine and TG Rogers. A theory of machining of fiber-reinforced materials. *Journal of Composite Materials*, 5(1):94–106, 1971.

[22] V Chandrasekharan, Shiv Gopal Kapoor, and Richard E. DeVor. A mechanistic approach to predicting the cutting forces in drilling: with application to fiber-reinforced composite materials. 1995.

[23] Aksel Koplev, Aage Lystrup, and T. Vorm. The cutting process, chips, and cutting forces in machining cfrp. *Composites*, 14(4):371–376, 1983.

[24] Hong Hocheng, HY Puw, and Y Huang. Preliminary study on milling of unidirectional carbon fibre-reinforced plastics. *Composites Manufacturing*, 4(2):103–108, 1993.

[25] Ashkan Sahraie Jahromi and Behnam Bahr. An analytical method for predicting cutting forces in orthogonal machining of unidirectional composites. *Composites Science and Technology*, 70(16):2290–2297, 2010.

[26] D. Nayak, Naresh Bhatnagar, and Puneet Mahajan. Machining studies of UD-FRP composites part 2: finite element analysis. *Machining Science and Technology*, 9(4):503–528, 2005.

[27] Peter A Cundall and Otto DL Strack. A discrete numerical model for granular assemblies. *geotechnique*, 29(1):47–65, 1979.

[28] Hany El Kadi. Modeling the mechanical behavior of fiber-reinforced polymeric composite materials using artificial neural networks—a review. *Composite structures*, 73(1):1–23, 2006.

[29] Wolfgang Hintze, Dirk Hartmann, and Christoph Schütte. Occurrence and propagation of delamination during the machining of carbon fibre reinforced

plastics (cfrps)–an experimental study. *Composites Science and Technology*, 71(15):1719–1726, 2011.

[30] Alaa E. Bayoumi, Gundog Yücesan, and Donny V. Hutton. On the closed form mechanistic modeling of milling: Specific cutting energy, torque, and power. *Journal of materials engineering and performance*, 3(1):151–158, 1994.

[31] Volker Schulze, Christoph Becke, and Rüdiger Pabst. Specific machining forces and resultant force vectors for machining of reinforced plastics. *CIRP Annals*, 60:69–72, 2011.

[32] Guoyong Zhao, Ziye Liu, Yan He, Huajun Cao, and Yuebin Guo. Energy consumption in machining: Classification, prediction, and reduction strategy. *Energy*, 133:142–157, 2017.

[33] Vincent Aizebeoje Balogun and Paul Tarisai Mativenga. Impact of un-deformed chip thickness on specific energy in mechanical machining processes. *Journal of Cleaner Production*, 69:260–268, 2014.

[34] Yanli He, Huanan Qing, Shengguang Zhang, Dazhen Wang, and Shengwei Zhu. The cutting force and defect analysis in milling of carbon fiber-reinforced polymer (cfrp) composite. *The International Journal of Advanced Manufacturing Technology*, 93, 11 2017.

[35] AI Azmi, AZ Syahmi, M Naquib, TC Lih, AF Mansor, and ANM Khalil. Effects of machining conditions on the specific cutting energy of carbon fibre reinforced polymer composites. In *Journal of Physics: Conference Series*, volume 908, page 012053. IOP Publishing, 2017.

[36] Qinglong An, Weiwei Ming, Xiaojiang Cai, and Ming Chen. Study on the cutting mechanics characteristics of high-strength ud-cfrp laminates based on orthogonal cutting method. *Composite Structures*, 131:374–383, 2015.

[37] CH Lauro, Lincoln Cardoso Brandão, Denison Baldo, RA Reis, and JP Davim. Monitoring and processing signal applied in machining processes–a review. *Measurement*, 58:73–86, 2014.

[38] Oleg Ryabov, Kazuo Mori, Nagayoshi Kasashima, and Kunio Uehara. An in-process direct monitoring method for milling tool failures using a laser sensor. *CIRP Annals*, 45(1):97–100, 1996.

[39] Michele Lanzetta. A new flexible high-resolution vision sensor for tool condition monitoring. *Journal of Materials Processing Technology*, 119(1):73–82, 2001.

[40] Steven Y. Liang, Rogelio L. Hecker, and Robert G. Landers. Machining Process Monitoring and Control: The State-of-the-Art . *Journal of Manufacturing Science and Engineering*, 126(2):297–310, 07 2004.

[41] P Stavropoulos, D Chantzis, C Doukas, Alexios Papacharalampopoulos, and George Chryssolouris. Monitoring and control of manufacturing processes: A review. *Procedia CIRP*, 8:421–425, 2013.

[42] Paolo Bosetti and Francesco Biral. Application of optimal control theory to milling process. In *IECON 2014-40th Annual Conference of the IEEE Industrial Electronics Society*, pages 4896–4901. IEEE, 2014.

[43] Yusuf Altinas. Manufacturing automation: Metal cutting mechanics, machine tool vibration, and cnc design (2012).

[44] Scott Smith and Jiri L. Tlusty. An overview of modeling and simulation of the milling process. *Journal of engineering for industry*, 113(2):169–175, 1991.

[45] Erhan Budak, Yusuf Altintas, and EJA Armarego. Prediction of milling force coefficients from orthogonal cutting data. *Journal of Manufacturing Science and Engineering*, 118(2):216–224, 1996.

[46] Serafettin Engin and Yusuf Altintas. Mechanics and dynamics of general milling cutters.: Part I: helical end mills. *International journal of machine tools and manufacture*, 41(15):2195–2212, 2001.

[47] EJA Armarego and RC Whitfield. Computer based modelling of popular machining operations for force and power prediction. *Cirp Annals*, 34(1):65–69, 1985.

[48] Hao-Jen Fu, Richard E. DeVor, and Shiv Gopal Kapoor. A mechanistic model for the prediction of the force system in face milling operations. 1984.

[49] Oscar Gonzalo, Jokin Beristain, Haritz Jauregi, and Carmen Sanz. A method for the identification of the specific force coefficients for mechanistic milling simulation. *International Journal of Machine Tools and Manufacture*, 50(9):765–774, 2010.

[50] Niccolò Grossi, Lorenzo Sallese, Antonio Scippa, and Gianni Campatelli. Speed-varying cutting force coefficient identification in milling. *Precision Engineering*, 42:321–334, 2015.

[51] Edouard Rivière-Lorphèvre and Enrico Filippi. Mechanistic cutting force model parameters evaluation in milling taking cutter radial runout into account. *The International Journal of Advanced Manufacturing Technology*, 45(1-2):8, 2009.

[52] Mark A Rubeo and Tony L Schmitz. Milling force modeling: a comparison of two approaches. *Procedia Manufacturing*, 5:90–105, 2016.

[53] Jamal Sheikh-Ahmad, Janet Twomey, Devi Kalla, and Prashant Lodhia. Multiple regression and committee neural network force prediction models in milling frp. *Machining Science and Technology*, 11(3):391–412, 2007.

[54] Fei Su, Juntang Yuan, Fujian Sun, Zhenhua Wang, and Zhaohui Deng. Modeling and simulation of milling forces in milling plain woven carbon fiber-reinforced plastics. *The International Journal of Advanced Manufacturing Technology*, 95(9):4141–4152, 2018.

[55] M Eugene Merchant. Mechanics of the metal cutting process. I. orthogonal cutting and a type 2 chip. *Journal of applied physics*, 16(5):267–275, 1945.

[56] Wang Haiyan and Qin Xuda. A mechanistic model for cutting force in helical milling of carbon fiber-reinforced polymers. *The International Journal of Advanced Manufacturing Technology*, 82(9):1485–1494, 2016.

[57] Yiğit Karpat, Onur Bahtiyar, and Burak Değer. Mechanistic force modeling for milling of unidirectional carbon fiber reinforced polymer laminates. *International Journal of Machine Tools and Manufacture*, 56:79–93, 2012.

[58] Cutpro. Manufacturing automation inc. www.malinc.com.

[59] Tilo Strutz. *Data fitting and uncertainty: A practical introduction to weighted least squares and beyond*. Vieweg and Teubner, 2010.

[60] Kornel Ehmann, Shiv Gopal Kapoor, Richard E. DeVor, and Ismail Lazoglu. Machining process modeling: a review. *Journal of manufacturing science and engineering*, 119(4B):655–663, 1997.

[61] C.A. Van Luttervelt, Thomas H.C. Childs, I.S. Jawahir, Fritz Klocke, Patrick K. Venuvinod, Yusuf Altintas, EJA Armarego, David Alan Dornfeld, Igor Grabec, Jurgen Leopold, Bo Lindström, Don A. Lucca, Toshiyuki Obìkawa, Shirakashi, and Hisayoshi Sato. Present situation and future trends in modelling of machining operations progress report of the cirp working group 'modelling of machining operations'. *CIRP Annals*, 47(2):587–626, 1998.

[62] Yusuf Altintas, Petra Kersting, D Biermann, Erhan Budak, Berend Denkena, and Ismail Lazoglu. Virtual process systems for part machining operations. *CIRP Annals*, 63(2):585–605, 2014.

[63] Simon S. Park and Yusuf Altintas. Dynamic compensation of spindle integrated force sensors with kalman filter. *Journal of Dynamic Systems, Measurement, and Control*, 126(3):443–452, 2004.

[64] Paolo Albertelli, Massimo Goletti, Mattia Torta, Mehdi Salehi, and Michele Monno. Model-based broadband estimation of cutting forces and tool vibration in milling through in-process indirect multiple-sensors measurements. *The International Journal of Advanced Manufacturing Technology*, 82(5):779–796, 2016.

[65] Andreas Albrecht, Simon S. Park, Yusuf Altintas, and Günter Pritschow. High frequency bandwidth cutting force measurement in milling using capacitance displacement sensors. *International Journal of Machine Tools and Manufacture*, 45(9):993–1008, 2005.

[66] Deniz Aslan and Yusuf Altintas. Prediction of cutting forces in five-axis milling using feed drive current measurements. *IEEE/ASME Transactions on Mechatronics*, 23(2):833–844, 2018.

[67] M Eugene Merchant. Basic mechanics of the metal-cutting process. *ASME J. of Applied Mechanics*, 11:A168, 1944.

[68] Eun-Hee Lee. The theory of plasticity applied to a problem of machining. *ASME J. Appl. Mech.*, 18:405, 1951.

[69] W.B. Palmer and P.L.B. Oxley. Mechanics of orthogonal machining. *Proceedings of the Institution of Mechanical Engineers*, 173(1):623–654, 1959.

[70] Rodney J. Hill. The mechanics of machining: a new approach. *Journal of the Mechanics and Physics of Solids*, 3(1):47–53, 1954.

[71] Pedro Jose Arrazola, Tugrul Özel, Domenico Umbrello, Matthew A. Davies, and Ibrahim S. Jawahir. Recent advances in modelling of metal machining processes. *CIRP Annals*, 62(2):695–718, 2013.

[72] Jaroslav Mackerle. Finite-element analysis and simulation of machining: a bibliography (1976–1996). *Journal of materials processing technology*, 86(1-3):17–44, 1999.

[73] EJA Armarego and Robert Hallowes Brown. The machining of metals. *Prentice-Hall Inc, Englewood Cliffs, N. J., 1969, 437 P*, 1969.

[74] Thankappan Radhakrishnan and Uday Nandan. Milling force prediction using regression and neural networks. *Journal of Intelligent Manufacturing*, 16(1):93–102, 2005.

[75] Tamas Szecsi. Cutting force modeling using artificial neural networks. *Journal of Materials Processing Technology*, 92:344–349, 1999.

[76] ME Martellotti. An analysis of the milling process. *Trans ASME*, 63:677, 1941.

[77] F Koenigsberger and AJP Sabberwal. An investigation into the cutting force pulsations during milling operations. *International Journal of Machine Tool Design and Research*, 1(1-2):15–33, 1961.

[78] William A. Kline and Richard E. DeVor. The effect of runout on cutting geometry and forces in end milling. *International Journal of Machine Tool Design and Research*, 23(2-3):123–140, 1983.

[79] AJP Sabberwal and F Koenigsberger. Chip section and cutting force during the milling operation. *Annals of the CIRP*, 10(3):197–203, 1961.

[80] Yusuf Altintas. *Manufacturing automation: metal cutting mechanics, machine tool vibrations, and CNC design*. Cambridge university press, 2012.

[81] Mark A Rubeo and Tony L Schmitz. Mechanistic force model coefficients: A comparison of linear regression and nonlinear optimization. *Precision Engineering*, 45:311–321, 2016.

[82] Edouard Rivière-Lorphèvre, Christophe Letot, François Ducobu, Pierre Dehombreux, and Enrico Filippi. Dynamic simulation of milling operations with small diameter milling cutters: effect of material heterogeneity on the cutting force model. *Meccanica*, 52(1-2):35–44, 2017.

[83] Eric Dimla Sr and Paul M. Lister. On-line metal cutting tool condition monitoring.: I: force and vibration analyses. *International Journal of Machine Tools and Manufacture*, 40(5):739–768, 2000.

[84] Yusuf Altintas and Deniz Aslan. Integration of virtual and on-line machining process control and monitoring. *CIRP Annals*, 66(1):349–352, 2017.

[85] Shihchieh Lin and Richard J.T. Lin. Tool wear monitoring in face milling using force signals. *Wear*, 198(1-2):136–142, 1996.

[86] Sounak Kumar Choudhury and Subhashree Rath. In-process tool wear estimation in milling using cutting force model. *Journal of Materials Processing Technology*, 99(1-3):113–119, 2000.

[87] Mehdi Nouri, Barry K Fussell, Beth L Ziniti, and Ernst Linder. Real-time tool wear monitoring in milling using a cutting condition independent method. *International Journal of Machine Tools and Manufacture*, 89:1–13, 2015.

[88] Rolf Isermann. Process fault detection based on modeling and estimation methods—a survey. *automatica*, 20(4):387–404, 1984.

[89] Lee M Kumanchik and Tony L Schmitz. Improved analytical chip thickness model for milling. *Precision Engineering*, 31(3):317–324, 2007.

[90] Takashi Matsumura and Shoichi Tamura. Cutting force model in milling with cutter runout. *Procedia CIRP*, 58:566–571, 2017.

[91] Robert Grover Brown. *Introduction to random signals and Kalman filtering*. John Wiley, 1992.

[92] Milton Clayton Shaw and JO Cookson. *Metal cutting principles*, volume 2. Oxford university press New York, 2005.

[93] Eric A Wan and Rudolph Van Der Merwe. The unscented kalman filter for nonlinear estimation. In *Proceedings of the IEEE 2000 Adaptive Systems for Signal Processing, Communications, and Control Symposium (Cat. No. 00EX373)*, pages 153–158. Ieee, 2000.

[94] A. Jullien-Corrigan and K. Ahmadi. Measurement of high-frequency milling forces using piezoelectric dynamometers with dynamic compensation. *Precision Engineering*, 66:1–9, 2020.

[95] Tao Chen, Jiupeng Xiang, Fei Gao, Xianli Liu, and Guangjun Liu. Study on cutting performance of diamond-coated rhombic milling cutter in machining carbon fiber composites. *The International Journal of Advanced Manufacturing Technology*, 103(9):4731–4737, 2019.

[96] Devi Kalla, Jamal Sheikh-Ahmad, and Janet Twomey. Prediction of cutting forces in helical end milling fiber reinforced polymers. *International Journal of Machine Tools and Manufacture*, 50(10):882–891, 2010.

[97] Wang Haiyan, Qin Xuda, Li Hao, and Chengzu Ren. Analysis of cutting forces in helical milling of carbon fiber-reinforced plastics. *Proceedings of the Institution of Mechanical Engineers, Part B: Journal of Engineering Manufacture*, 227:62–74, 01 2012.

[98] Qinglong An, Weiwei Ming, Xiaojiang Cai, and Ming Chen. Study on the cutting mechanics characteristics of high-strength ud-cfrp laminates based on orthogonal cutting method. *Composite Structures*, 131:374–383, 2015.

[99] Youliang Su, Zhenyuan Jia, Bin Niu, and Guangjian Bi. Size effect of depth of cut on chip formation mechanism in machining of cfrp. *Composite Structures*, 164:316–327, 2017.

[100] Raimund Mullin, Mehran Farhadmanesh, Ahmadian, and Keivan Ahmadi. Modeling and identification of cutting forces in milling of carbon fibre reinforced polymers. *Journal of Materials Processing Technology*, 280:116595, 2020.

[101] Yusuf Altintas and Abraham A. Ber. Manufacturing automation: metal cutting mechanics, machine tool vibrations, and cnc design. *Appl. Mech. Rev.*, 54(5):B84–B84, 2001.

[102] Mingyi Guo, Xifeng Fang, Zhongtai Hu, and Qun Li. Design and research of digital twin machine tool simulation and monitoring system. 2022.

[103] G. Byrne and Garret E. O'Donnell. An integrated force sensor solution for process monitoring of drilling operations. *CIRP Annals*, 56(1):89–92, 2007.

[104] Min Wan, Shao-En Li, Heng Yuan, and Wei-Hong Zhang. Cutting force modelling in machining of fiber-reinforced polymer matrix composites (pmcs): A review. *Composites Part A: Applied Science and Manufacturing*, 117:34–55, 2019.

[105] Mehran Farhadmanesh and Keivan Ahmadi. Online identification of mechanistic milling force models. *Mechanical Systems and Signal Processing*, 149:107318, 2021.

[106] Robert Grover Brown. *Introduction to random signal analysis and Kalman filtering*, volume 8. Wiley New York, 1983.

[107] Robert Voss, Lukas Seeholzer, Friedrich Kuster, and Konrad Wegener. Influence of fibre orientation, tool geometry and process parameters on surface quality in milling of cfrp. *CIRP Journal of Manufacturing Science and Technology*, 18:75–91, 2017.

[108] Imed Zaghbani, Jean-François Chatelain, Victor Songmene, Sebastien Berube, and Abdelatif Atarsia. A comprehensive analysis of cutting forces during routing of multilayer carbon fiber-reinforced polymer laminates. *Journal of composite materials*, 46(16):1955–1971, 2012.

[109] Jianzhang Xiao, Chongyang Gao, and Yinglin Ke. An analytical approach to cutting force prediction in milling of carbon fiber reinforced polymer laminates. *Machining Science and Technology*, 22(6):1012–1028, 2018.

[110] Fu-Ji Wang, Jian-Bo Yan, Meng Zhao, Dong Wang, Xiao-Nan Wang, and Jia-Xuan Hao. Surface damage reduction of dry milling carbon fiber reinforced plastic/polymer using left–right edge milling tool. *Journal of Reinforced Plastics and Composites*, 39(11-12):409–421, 2020.

[111] Yusuf Altintaş. Direct adaptive control of end milling process. *International Journal of Machine Tools and Manufacture*, 34(4):461–472, 1994.

Appendix A

Entries of Matrix B

The non-zero entries of the matrix $\mathbf{a}(\theta, \psi)$ given in Equation (2.13) are provided in Table A.1 for downmilling, half-immersion, $\phi_s = 90^o, \phi_e = 180^o$, with a two fluted tool ($N = 2$) and assuming $\psi = 0$.

Table A.1: A Matrix Entries for downmilling

$$a_{1,1} = \frac{a}{2\pi}$$
$$a_{1,3} = -\frac{a}{4}$$
$$a_{1,5} = \frac{1/8\,a\pi - 1/4\,a\pi\,(\cos(\theta))^2}{\pi}$$
$$a_{1,6} = \frac{1}{4} a \sin(\theta) \cos(\theta)$$
$$a_{1,9} = \frac{-a/2 + a(\cos(\theta))^2 + 1/4\,a\pi\,\sin(\theta)\cos(\theta)}{\pi}$$
$$a_{1,10} = \frac{-1/8\,a\pi + 1/4\,a\pi\,(\cos(\theta))^2 - a\sin(\theta)\cos(\theta)}{\pi}$$
$$a_{2,2} = a/\pi$$
$$a_{2,4} = -a/\pi$$
$$a_{2,7} = \frac{2/3\,a - 4/3\,a(\cos(\theta))^2 + 2/3\,a\sin(\theta)\cos(\theta)}{\pi}$$
$$a_{2,8} = \frac{-a/3 + 2/3\,a(\cos(\theta))^2 + 4/3\,a\sin(\theta)\cos(\theta)}{\pi}$$
$$a_{2,11} = \frac{-2/3\,a + 4/3\,a(\cos(\theta))^2 + 2/3\,a\sin(\theta)\cos(\theta)}{\pi}$$
$$a_{2,12} = \frac{-a/3 + 2/3\,a(\cos(\theta))^2 - 4/3\,a\sin(\theta)\cos(\theta)}{\pi}$$
$$a_{3,1} = a/4$$
$$a_{3,3} = \frac{a}{2\pi}$$
$$a_{3,5} = \frac{a/2 - a(\cos(\theta))^2 - 1/4\,a\pi\,\sin(\theta)\cos(\theta)}{\pi}$$
$$a_{3,6} = \frac{1/8\,a\pi + a\sin(\theta)\cos(\theta) - 1/4\,a\pi\,(\cos(\theta))^2}{\pi}$$
$$a_{3,9} = \frac{1/8\,a\pi - 1/4\,a\pi\,(\cos(\theta))^2}{\pi}$$
$$a_{3,10} = \frac{1}{4} a \sin(\theta) \cos(\theta)$$
$$a_{4,2} = a/\pi$$
$$a_{4,4} = a/\pi$$
$$a_{4,7} = \frac{2/3\,a - 4/3\,a(\cos(\theta))^2 - 2/3\,a\sin(\theta)\cos(\theta)}{\pi}$$
$$a_{4,8} = \frac{a/3 - 2/3\,a(\cos(\theta))^2 + 4/3\,a\sin(\theta)\cos(\theta)}{\pi}$$
$$a_{4,11} = \frac{2/3\,a - 4/3\,a(\cos(\theta))^2 + 2/3\,a\sin(\theta)\cos(\theta)}{\pi}$$
$$a_{4,12} = \frac{-a/3 + 2/3\,a(\cos(\theta))^2 + 4/3\,a\sin(\theta)\cos(\theta)}{\pi}$$